QATAR UNIVERSITY

COLLEGE OF ENGINEERING

TOWARD THE DEVELOPMENT OF PRINTABLE PEROVSKITE SOLAR CELLS

BY

ARTI MISHRA

A Dissertation Submitted to the

Faculty of the College of Engineering

In Partial Fulfillment of the Requirements for the Degree of

Doctorate of Philosophy in Electrical Engineering

June 2019

COMMITTEE PAGE

The members of the Committee approve the Dissertation of

Arti Mishra defended on 18/04/2019.

Prof. Farid Touati

Dr. Zubair Ahmad

_____

Thesis/Dissertation Supervisors

_____

Name

Committee Member

_____

Name

Committee Member

_____

Name

Committee Member

_____

Add Member

Approved:

_____

Abdel Magid Hamouda, Dean, College of Engineering

ABSTRACT

MISHRA ARTI, Doctorate: June: 2019,

Doctorate of Philosophy in Electrical Engineering

Title: Toward the Development of Printable Perovskite Solar Cells

Supervisors of Dissertation: Prof. Farid Touati and Dr. Zubair Ahmad

.

PSCs have become a significant performer in third generation photovoltaics with power conversion efficiency, greater than 22% for active areas less than 1 cm^2. However, with efficiency improvement, concerns regarding the operational stability and industrial production firstly resolved to grow into commercially viable PSCs. To address above stated issues most stable, yet efficient Monolithic PSCs (mPSCs) are structured. The mPSCs are having compact TiO_2, mesoporous TiO_2, mesoporous ZrO_2, and mesoporous carbon electrode layers in optimal thicknesses on the FTO substrate. Fabrication protocol for all the layers which is easily scalable for large area mPSCs manufacturing is highly required. Furthermore top carbon electrode materials those are stable and behaves as protective casing to make PSCs stable has also been highly desired. Hence, in this project our aim is to optimize top carbon layer and study photophysical processes inside the mPSCs. This research work is mainly divided into three parts.

The first part of the dissertation described carbon film fabrication by screen printing technique and their investigation at different annealing temperature.

Influence of annealing temperatures on the electrical, morphological and structural properties of the carbon film has been discussed. It is shown that a low annealing temperature is good for better adherence of the conductive carbon films, however, temperatures higher than 300°C are required to produce efficient mPSCs. A sintering temperature of 400°C showed the highest device efficiency of 13.2%.

It is important to correlate all the physical properties/processes taking place in the mPSCs to gain a deeper understanding of mPSCs operation: What is the role of the contacts? What limits the efficiency of existing perovskite solar cells? How many charge carriers are there in the cell under operating condition. Hence, in second part, Electrochemical Impedance spectroscopy (EIS) spectrum has been described, which is performed on the mPSCs having highest efficiency during previous experiments. The EIS spectrum of mPSCs quantitatively explains the role of contacts, layers, charge generation, drift and diffusion of charge carriers and recombination. This would further provide insight into the performance-limiting physical processes of mPSCs.

The microstructure or morphology of the perovskite crystals inside mesoporous TiO_2 and mesoporous ZrO_2 have significant effect on the mPSCs performance and stability. Therefore, to achieve higher mPSCs device performance, one-dimensional microrods (4mm-5mm) of PbI_2 and $CH_3NH_3PbI_3$ ($MAPbI_3$) is fabricated in the 3rd part. These microrods consist of unique structural and morphological properties which are grown at room temperature. The XRD and TEM analyses confirm the existence of strong interactions between different stable

groups in the crystals. The morphological studies approve crack free morphology of PbI_2 and $MAPbI_3$ micro-rods. The above results are expected to have a big effect on solar cell and photo-detection industry by fostering improvement of thin-film opto-electronic devices.

Keywords: Monolithic perovskite solar cells, Power conversion efficiency, Carbon film, screen printing, Electrochemical Impedance spectroscopy, One dimensional micro-rods

DEDICATION

I dedicate my thesis work to my family. A special gratitude to my in-laws Chandra Prabha and M P Mishra whose care and encouragement push me forward. My husband Narendra Mishra whose constructive criticisms have been improved my persona. My daughters Shashi and Arshi for being decent and responsible kids.

I would also dedicate this thesis to my parents Shyam Sundar and Raghav Pandey for teaching me importance of hard work and dedication. My elder brother Col Ashok Kumar Pandey and elder sister Alka Pandey for being my first teachers and role models.

ACKNOWLEDGMENTS

I would also like to thank Late Prof. Mohieddine Amor Benammar for his role in my admission and supervision during the first two years of my PhD.

I would like to thank my PhD supervisor, Professor Farid Touati (Department of Electrical Engineering), for selecting me to pursue doctoral studies in his group. He always trusts me and encourage me to undertake my research interest freely, at the same time Prof. Farid has been always available with advice and support I wished.

Next, I would like to thank Dr. Zubair Ahmad (Center for Advanced materials) my co-supervisor and a great mentor for his unconditional support. I learned a lot from countless discussions with Dr. Zubair on scientific topics from the beginning of my research.

I also thank Dr. R.A. Shakoor (Center for Advanced materials) and Prof. Md. K. Nazeeruddin (Ecole Polytechnique fédérale de Lausanne) for their encouragement and helpful reviews.

I would also like to thank Dr. Nasser Abdullah Alnuaimi (Director CAM) and Dr. Peter Kasak (Technical Manager CAM) for all the support he provided while working in CAM.

My special gratitude to the personnel of the Center for Advanced materials Mr. Abdulla Al Ashraf, Mr. Moinuddin Mohammed Yusuf, Mr. Abdul Jaleel Naushad, Mr. Mohammed Ismail Saleh for his technical assistance during day to day lab experiments.

I would also like to thank Central Laboratory Unit staff Dr. Mohammed Yousuf and Mr. Essam Shabaan Mohamed Attia for conducting TEM and FESEM analysis for our samples.

I owe special thanks to my colleagues Mr. Shoaib Alam Mallick, Mr. Indra Gunawan and Ms. Sumayya Muhammad Abdulrahim for creating dynamic and vibrant working environment.

I would also like to thank Dr. Fadi Jaber for his supervision during the first two years of my PhD.

Further I would like to thank Qatar University and Center for Advanced Materials for facilitating me required lab facilities. Qatar University Internal Grant No. QUCG-CAM-2018/19-1 for funding and our collaborator Qatar Aluminium (Qatalum) for providing partial financial support for this dissertation.

TABLE OF CONTENTS

LIST OF FIGURES

LIST OF TABLES

Chapter 1: Importance of Renewable Sources of Energy

If growing economies ignore the problem of global warming, and pollution than also exhausting fossil fuels will not be able to meet global energy requirement alone for more than a century. The Energy Information Administration expects an increase of 48% in current consumption by 2040 [1]. Hence its compulsion for scientific community to find clean, inexhaustible and competitive renewable energy supplies to meet future requirements. Among all available renewable energies (geo, hydro, solar, wind) on the earth, solar radiation is most abundantly available (4.1×10^{20} Joles/hour) hence photovoltaic solar cells are the most feasible source to produce electricity and have potential to encounter the world's continually growing energy demand.

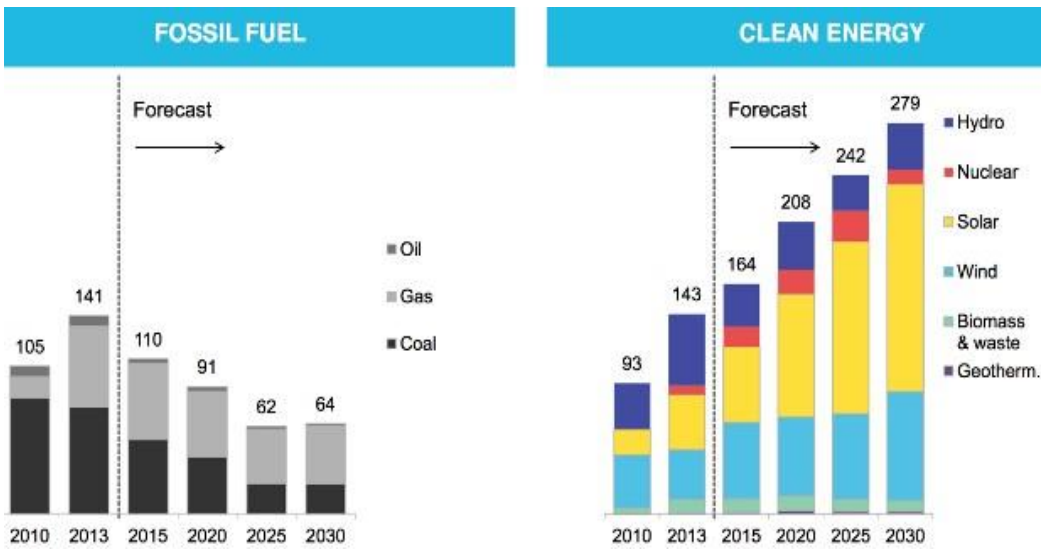

Figure 1.1: Power generation capacity and future forecast from renewable and nonrenewable sources [2]

Photovoltaic Technology:

Photovoltaic research gains tremendous attention because it is cheap, easily available, and abstraction does not stress environments. Hence till date its contribution to power generation is maximum among all available renewable sources of energy (Figure 1.1). Photo voltaic technology commonly separated into three generations for research and development and commercialization. The first generation is mainly Silicon wafer-based. Solar cells and second-generation thin films (CIGS, GaAs and CdTe) based. They both are well developed, mature, and commercially available, but they have not shown any further improvement in terms of efficiency suffer from prohibitive cost, manufacturing complexity and material scarcity. For example, if we supply all 2050 global electricity demand with Silicon technology require two times more silicon, and three times more aluminum that have been extracted since 1900, similarly 34 years of cadmium mining and 1500 years tellurium mining for CdTe solar cell production at current rates. Furthermore, purities of these critical elements are also very important which make element extraction expensive. Hence demand of substantial increase in efficiency with cost reduction for these forerunner technologies is no more achievable. [3]

Third generation contains dye-sensitized solar cells (DSCs), perovskite solar cells (PSCs), thin film solar cells, quantum dots solar cells and cells constructed using nano-materials. However, hypothetically, low-cost, and lab scale high-efficient thirdgeneration solar cells are waiting for commercialization PSCs are most promising among all stated third generation solar cells. [4]

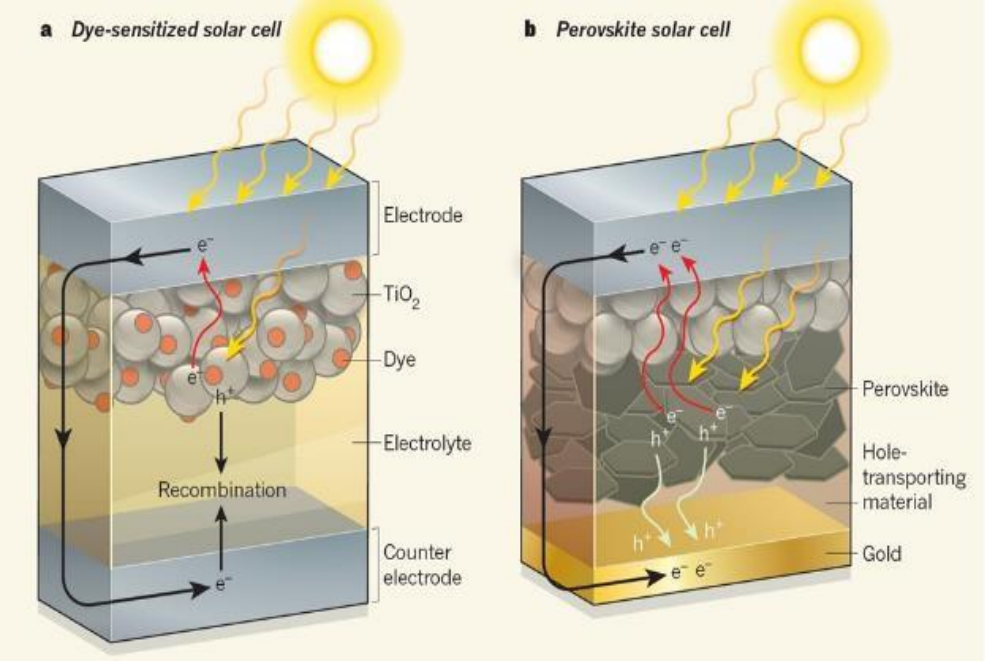

Figure 1.2: (a), A DSC consists ruthenium-based dye molecules that are located on titanium dioxide (TiO_2) nanoparticles. Incident sunlight produces electron (e^-) and hole (h^+) in the dye. The electron further absorbed by the TiO_2 film and is later transported to a metal electrode. (b), In a solidstate Perovskite Solar Cell, hole transport material (HTM) Spiro-OMeTAD is used in place of liquid electrode and semiconductor material called perovskites act as the light absorber. [5]

DSCs architecture reported in 1991 by O'Regan and Grätzel in Nature is the landmark work of a low-cost DSCs. This cell had around 7.5% efficiency. In this cell ruthenium-based dye molecules (Figure 1.2) that are located on titanium dioxide (TiO_2) nanoparticles absorb light. but this device is highly unstable [6]. However, the basic concept of using porous TiO_2 with light absorbing dye has become a forerunner for further improvement. The next step was to improve stability of the device which is not possible to achieve with liquid electrolyte, hence solid-state DSCs is introduced [7]. With the introduction of problems associated with liquid leakage is solved and device stability is increased up to 80 hrs. However, the efficiencies of solid-state DSCs were very poor because the HTM Spiro-OMeTAD do not infuse in the TiO_2 film as

homogeneously as liquid electrolytes. Many other parameters of this solar cell also need to be optimized for efficiency improvement, hence open new era of innovations which include improvement in device architecture as well as the introduction of new materials. In this context Cai. et. Al introduced organic D-π-A dye C220 which is having molar absorption coefficient ε 5.5 × 10^4 M^{-1} cm^{-1} at 555 nm, which is approximately five times higher than that of the usual Z907 ruthenium sensitizer (ε = 1.2 × 10^4 M^{-1} cm^{-1} at 521 nm) hence 6.08% efficiency achieved [8] which is further improved to7.2 % with p-type doping in Spiro-OMeTAD [9]. In addition, with high efficiency this device had shown good long-term stability also and produced 6-7 % efficiency after 2 weeks of their fabrication.

Table 1.1: Landmark work of Dye-sensitized solar cell towards the development of perovskite solar cell

Year	V_{oc} (V)	J_{sc} (mA/cm^2)	FF	PCE (%)	Device Active Area (cm^2)	Innovation	Reference
1991	0.67	2.3	0.684	7	0.5	DSC introduced	[6]
1998	0.342	3.18	0.62	0.74	NA	Solid-state DSC Spiro-OMeTAD Introduced	[7]
2011	0.88	9.735	0.71	6.08	0.3033	D-π-A dye	[8]
2011	0.986	9.5	0.76	7.2	NA	P-type doping with Spiro-OMeTAD	[9]

Due to all above benchmark work of Michael Grätzel and his group the DSCs cell is also called as Grätzel cell. For improving light energy conversion in DSCs many organic sensitizers and inorganic semiconductors had been extensively studied during this time. In 2009 Miyasaka and his group used organic inorganic halide structured perovskite made from $CH_3NH_3PbBr_3$ and $CH_3NH_3PbI_3$. as visible-light sensitizers in DSCs which is later acknowledged as perovskite solar cells (PSCs).[10] However, this cell was not able to produce good PCE but perovskite as light sensitizer gain much attention because of its unique optical and electrical properties hence further explored by many research groups.

Perovskite Solar Cell:

Perovskite Properties:

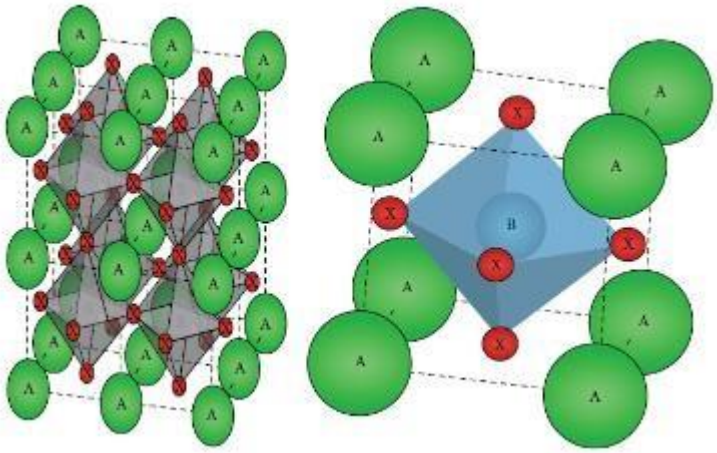

Figure 1.3: Perovskite crystal structure

Perovskite mineral was first discovered by a German mineralogist Gustav Rose in 1839. Initially perovskite is the ceramic oxide mineral $CaTiO_3$ but later include all

the compounds which crystallize in the identical ABX_3 structure (Figure 1.3) designated by Russian mineralogist L. A. Perovski in 1978 where A and B are cations of different sizes and X is an anion that bonds them together. In the ideal cubic perovskite structure, the B cation is at the center of an octahedral cage formed by the anions. (Figure 1). For perovskite solar cell A is organic cations made from methylammonium ($CH_3NH_3^+$), ethylammonium ($CH_3CH_2NH_3$), formamidinium ($NH_2CH{=}NH_2$). Or Cs^+ and Rb^+ inorganic cation. B is made from lead (Pb), tin (Sn) or germanium (Ge), comes from the same group. However, lead is commonly used in solar cell because it produces more stable and efficient cells. Sn tends to oxidize very easily, hence produces easily changeable cells and not possible to implement as a commercial device. Halide anion X is iodine (I), chlorine (Cl) or bromine (Br) element or combination of some of them (mixed halides $CH_3NH_3PbI_{3-x}Cl_x$ and $CH_3NH_3PbI_{3-x}Br_x$) however, fluoride-based perovskites are also not uncommon. [11]

All the perovskites used for solar cell applications are semiconductors. Hence perovskites exhibit comparable advantages of semiconductors. They are very low in cost, hence mass production is economical, recombination losses of the circuit are low. Charge carrier diffusion lengths are very large, and the cation and anion can exchange for tuning bandgap There are many materials which is having ABX_3 structure, hence have applications in many other areas also, Piezoelectric crystals, thermo-electric materials, insulating materials can be produced using these perovskites. Due to above all stated applications and excellent light-absorption properties of perovskites, they are under intense investigation among the photovoltaic researcher. [12]

The size of the A-site cation determines whether the material adopts a three dimensional structure or a two-dimensional structure. Cations including methylammonium, formamidinium, cesium and rubidium are known to form a 3D

structure, while the others arrange in a 2D structure made of flat BX_6 corner sharing structures intercalated with double layers of cations. 2D perovskite structures are significantly more tolerant in terms of the size and type of the organic cations.

Historical Background of Perovskite Solar Cell

In the 2009, Kojima, and Miyasaka used the architecture of DSCs and prepared first perovskite solar cell (PSC) [10] In this revolutionary DSCs, hybrid perovskites much precisely perovskite crystals (due to its crystalline structure) $CH_3NH_3PbBr_3$ and $CH_3NH_3PbI_3$ has been used as an alternative sensitizer to dye TiO_2 particles in the previously used DSCs architecture based on the liquid electrolyte. However, this device did not find much recognition that time due to very low efficiency (which is around 3.8%) and stability. However, Park and his co-workers successfully improved the efficiency of this configuration of perovskite-sensitized solar cells to 6%. [13] In this work quantum-dot-(QD) sensitized solar cell is fabricated using 2-3 nm sized perovskite ($CH_3NH_3PbI_3$) nanocrystal on nanocrystalline TiO_2 surface. In addition, they also done study on the relationship on thickness of TiO_2 film and absorption coefficient of the film and concluded that higher absorption coefficient requires thinner film. For this reason, at given thickness TiO_2 layer, perovskite QD shows much higher photocurrent density than N719 dye. However, the stability of this QD-sensitized solar cell is also very poor under continued 1sun irradiation it is approximately 10 min (about 80% degradation) due to perovskite QD tends to be dissolved into redox electrolyte. Hence Studies to improve long-term stability of PSC are extensively done during this time. These seminal works of the Miyasaka and Park initiated a boom by producing PSCs for improving stability of these cells (as done with DSC) liquid electrolytes transition to solid-state

PSCs has been done. Inorganic–organic hybrid perovskite structures have become innovative substitutions for next-generation solid state dye-sensitized solar cells, because they combine the advantages of both systems.

Around 2012, three equivalent breakthrough reports [14-16] on solid-state PSCs with 10–11% efficiencies prompted the research bang on PSCs. Firstly Kim et.al. introduced solid state hetero junction PSC In this work $CH_3NH_3PbI_3$ deposited on the mesoporous TiO_2 or Al_2O_3 particles with silver as metal electrode, shows panchromatic absorption of visible light, leading to high short circuit current J_{sc} (17 mA/cm^2) and open-circuit voltage V_{oc} (0.888 V) and fill factor of (0.62) and high PCE of 9.7% was achieved. This study also revealed by an impedance spectroscopic study that solid-state devices are depreciated by growing mesoporous TiO_2 film thickness, this is mainly credited to the increase in dark current and electron transport resistance Moreover, this PSCs reveals extremely good stability (more than 500 hours) even without encapsulation [14].

Similar structure solution-processable solar cell at the same time reported by Lee. et.al with J_{sc} = 17.8 mA/ cm^2, V_{oc} =0.98 V, and a fill factor of 0.63, hence attain PCE = 10.9%. This work explains that key limitation in performance of the PSC is a balance between series and shunt resistance. The perovskite absorber is practically conductive, measured to be on the order of 10^{-3} S/cm^3; therefore, short-circuiting of the device occurs if contact exists between the top metal electrode and the perovskite absorber. A thick covering layer of hole transport material readily resolves this issue. but; spiro-OMeTAD is less conductive (~10^{-5} S/cm^1), so a thicker capping layer results in high series resistance. Thus, they presented a compromise. [15]

In the 3rd study layered sandwich-type architecture, highlights that using three dimensional composites of TiO_2 and $CH_3NH_3PbI_3$ and corresponding well-matched polymeric hole conductors is key to produce good PCE. In this work poly-3hexylthiophene (P3HT), poly-[2,1,3-benzothiadiazole-4,7-diyl[4,4-bis(2ethylhexyl)4H-cyclopenta[2,1-b:3,4-b′]dithiophene-2,6-diyl]] (PCPDTBT), and (poly[[9-(1-octylnonyl)-9H-carbazole-,7diyl]2,5hiophenediyl2,1,benzothiadiazole4,7-diyl-2,5-thiophenediyl]) (PCDTBT) and poly-triarylamine (PTAA) are investigated as HTMs or electron-blocking layers. Highest efficiency produced by PTAA with gold counter electrode gives J_{sc} of 16.5 mA/cm^{-2} ,V_{oc} of 0.997 V and fill factor of 0.727, yielding a power conversion efficiency of 12.0% under standard 1 sun.[16]

Subsequently then, hybrid perovskites have attracted enormous worldwide attention from researchers working on different optoelectronic materials and methylammonium lead triiodide ($CH_3NH_3PbI_3$) is extensively used for manufacturing of solar cells. These research work focused on both perovskite material properties and device development principles. With the recent technological development PCE of 22.7 % has been attained at lab scale [17-20]. PSCs are under intensive investigation because of their outstanding power conversion efficiency, cost effective fabrication, and their great potential to compete with the conventional silicon technology [21, 22].

All above groups have demonstrated that the methylammonium lead triiodide ($CH_3NH_3PbI_3$) perovskite can be used not only as the light-absorbing material, but also as the charge-transporting material However, stability and scalability issues are causing to delay the PSCs to bring them into commercial market.

Types of Perovskite solar cell based on device Architecture:

All perovskite solar cells are built using bottom-up procedures on transparent Indium/fluorine conductive oxide coated glass substrate. However, broadly they can be classified into two separate categories planner and mesoporous architecture (Figure 1.4).

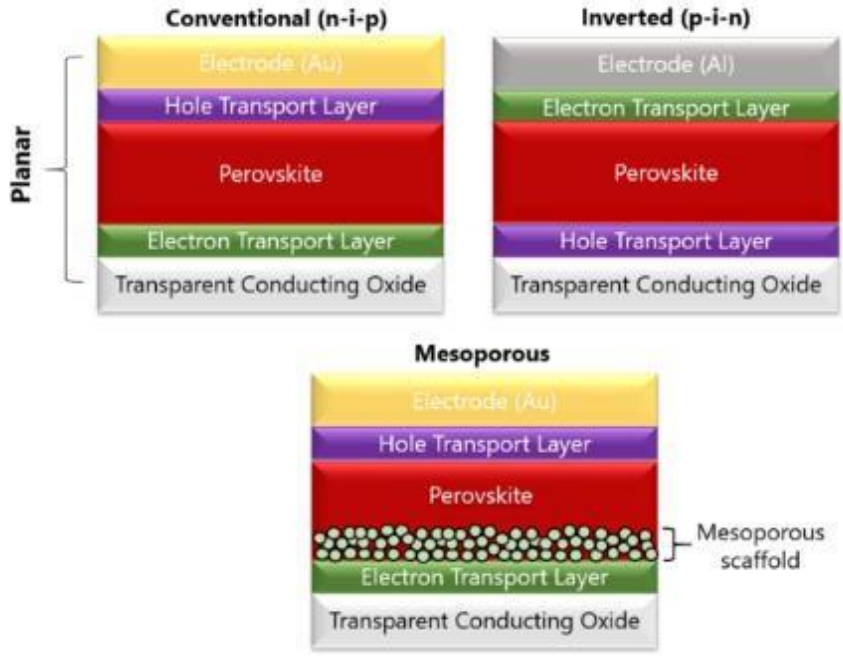

Figure 1.4: Conventional planer (n-i-p and p-i-n) and mesoporous perovskite cell architecture.

Mesoporous structure. The first PSC reported by the Miyasaka and group having a mesoporous scaffold. In this configuration a compact thin (10– 30 nm) layer of n-type TiO_2 film deposited on the FTO or ITO layered glass substrate. The compact TiO_2 layer acts as an electron transport layer and selectively blocks the holes. Annealing around 500^0C after spray pyrolysis or spin coating, process is generally used to fabricate compact layer. Subsequently, a thicker porous layer of TiO_2 (early configurations of PSCs also used Al_2O_3 nanoparticles) is

deposited and sintered at 500^0C and infiltrated by the perovskite solution. The conformation of mesoporous PSCs is like solid-state DSC solar cells by substituting dye molecular with lead halide perovskite. In the mesoporous structure, the perovskite morphology is principally governed by the underlying mesoporous scaffold, making the perovskite deposition facile and reproducible. In the early stage, the mesoporous configuration helped realize high-efficiency. The regular mesoporous layer is usually thicker than 500 nm, which could lead to a high charge-collection efficiency mesoporous layer thicker than 1 mm generally shows lower efficiency due to the limitation in charge-collection. A hole transport layer is then dropped on top of the perovskite layer to provide selectivity for holes. Most hole transport materials (HTM) consist of Spiro-MeOTAD but other HTM such as (PTAA), PCPDTBT, PCDTBT, P3HT has been also generally used. The device is ended by thermally evaporating a 40-200 nm top metal electrode of aluminum, gold or silver. The main disadvantage of the mesoporous configuration for PSCs is it usually requires a high-temperature annealing development, which is problematic for fabricating large area devices on large-sized fluorine-doped tin oxide (FTO) substrates. [15] Thus, developing low-temperature routes for growing a mesoporous scaffold layer represents one active direction of research. With the rapid development of perovskite film deposition, the pure mesoporous device structure has become less critical. Initially Other configurations, such as the bi-layer or planar cell structures, have attracted more attention with higher efficiencies demonstrated. However, one advantage associated with the mesoporous cell structure is the low (negligible) hysteresis in photocurrent density–voltage (J–V) measurements.

Bi-layer or Planner structure. The planar devices are having regular (n-i-p) [23] and inverted (p-i-n) [24] devices, depending on which discriminatory contact is top of the transparent electrode. Snaith et al. achieved 15% efficiency with regular planar heterojunction structure solar cells where the mesoporous TiO_2 layer was replaced with

only a compact TiO_2 layer. In this planar configuration on compact Tio_2 layer, the perovskite absorber is coated through vapor deposition solution-processed, and then hole transport material (HTM) is coated by spin coating and a 60–80 nm layer of Ag as top contact has been deposited by vacuum evaporation. In this configuration light travels through the glass and therefore the HTM and top contact can be completely opaque, although reflection from the top contact can help improve the PCE.

In the inverted architecture, or p-i-n, the HTM (usually the p-type conductive polymer poly(3,4-ethylenedioxythiophene) polystyrene sulfonate, or PEDOT: PSS is coated first, followed by perovskite layer. Hung and et.al. reported an interdiffusion method devices have a structure of ITO/PEDOT:PSS/$MAPbI_3$/PCBM/C_{60}/Al. They successfully fabricated pinhole free perovskite films using a low temperature (less than 100°C) solution process method. Highest efficiency of 15.4%, with a fill factor of more than 80%, and an efficiency of above 14.5% for more than 85% of the devices was achieved for the devices under one sun illumination. The interdiffusion method results in high device yield. [25] Inverted architectures are interesting because of their possible application to non-transparent substrates like metal foils. The low temperature used is compatible with plastic substrates. (which are also flexible). Fabrication of tandems PSCs.

Eventually, the efficiency of PSCs has achieved to 22.1% in early 2016 [19] and reached 23% in 2017[26, 27]. Meanwhile several groups have verified that the methyl ammonium lead triiodide ($CH_3NH_3PbI_3$) perovskite can be used not only as the light-absorbing material, but also as the charge-transporting material. The maximum theoretical PCE of the PSCs is calculated which is around 31.4%, hence there is still enough space for development [28].

Fabrication Technique:

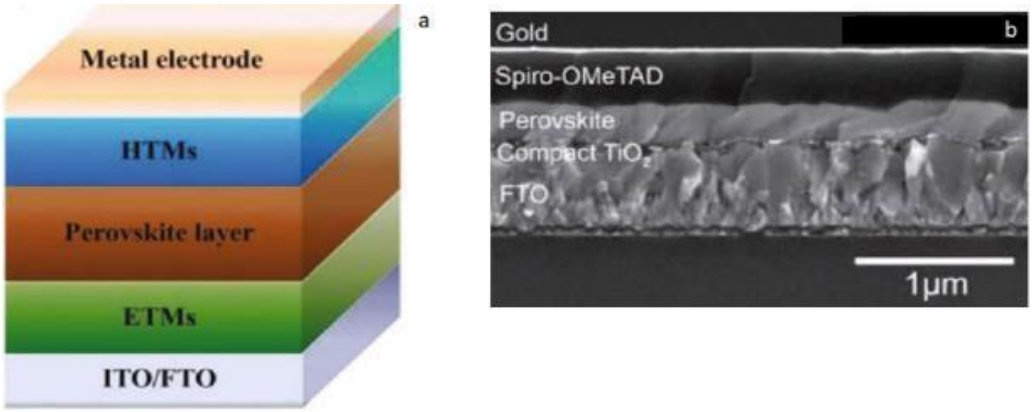

Figure 1.5: (a) Schematic diagram of a general PSC. (b) SEM images of a planar PSC [29]

Photovoltaic characteristics of perovskite solar cell (PSC) build by thin film fabrication technique is immensely depend upon fabrication procedure. The processing physiognomies have a major effect on the film morphology and coverage of the film on the substrate. Due to this different result can be produced with same perovskite materials. Environmental conditions (temperature, humidity) also effect the resultant film quality, hence should be carefully monitored. PSC can be built by different methods. A typical procedure is explained below. [30]

The general configuration of PSCs, shown in Figure 1.5, which usually comprises a tin-doped indium oxide (ITO)/fluorine-doped tin oxide (FTO) substrate, metal electrode, a perovskite photoactive layer, and charge transport layers. The mesoporous TiO2 is used as electron transport material (ETM) and layer built with this is called electron transport layer (ETL). A 2,2′,7,7′-tetrakis-(N,N-dipmethoxyphenylamine)-9,9′-spirobifluorene (spiro-OMeTAD) is a hole transport material (HTM) layer constructed by this is called

hole transport layer (HTL). The $CH_3NH_3PbI_3$ solution is used for perovskite layer preparation. The ETL, HTL and perovskite layers can be prepared by a simple spin-coating technique. Porosity and thickness of all the layers are adjusted by different solvent concentration used during material preparation and various fillers. Spin coating and annealing parameters also directs the quality of different layers. It is also recognized that the cleaning of the ITO/FTO surface is an important factor governing the performance of the devices. [30, 31]

Working Principle:

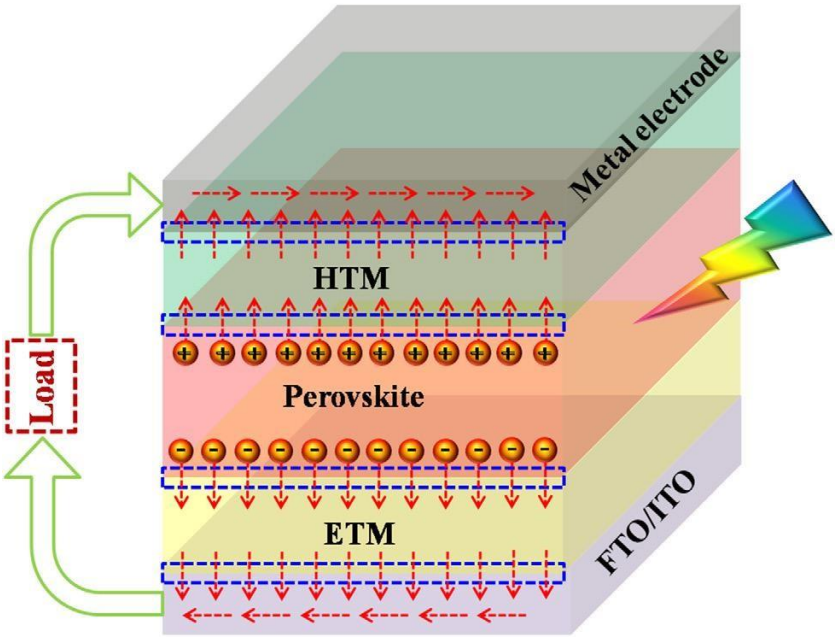

Figure 1.6: Schematic diagram of charge transport across the various interfaces in PSCs with each potentially contributing to losses and thereby reduced performance. [32]

The general working principle of these PSCs can be summarized in Figure 1.6. In PSCs, the absorber perovskite layer is sandwiched in between HTL and ETL. PSCs generate electricity, according to the following mechanism. On sunlight absorption the perovskite layer excites and absorb photons which have energy greater than its band gap and produce electron hole pair. Photo generated electron/hole pairs detached at the interfaces of other layers. Generated Electrons charge carriers in the perovskite layer are injected into the conduction band of the electron selective contact and collected by the anode, while holes are transported to the valence band of the hole selective layer and collected by the metal cathode creating the flow of electric current. Perovskite layer absorbs the incident photon and generate electrons and holes. [33]

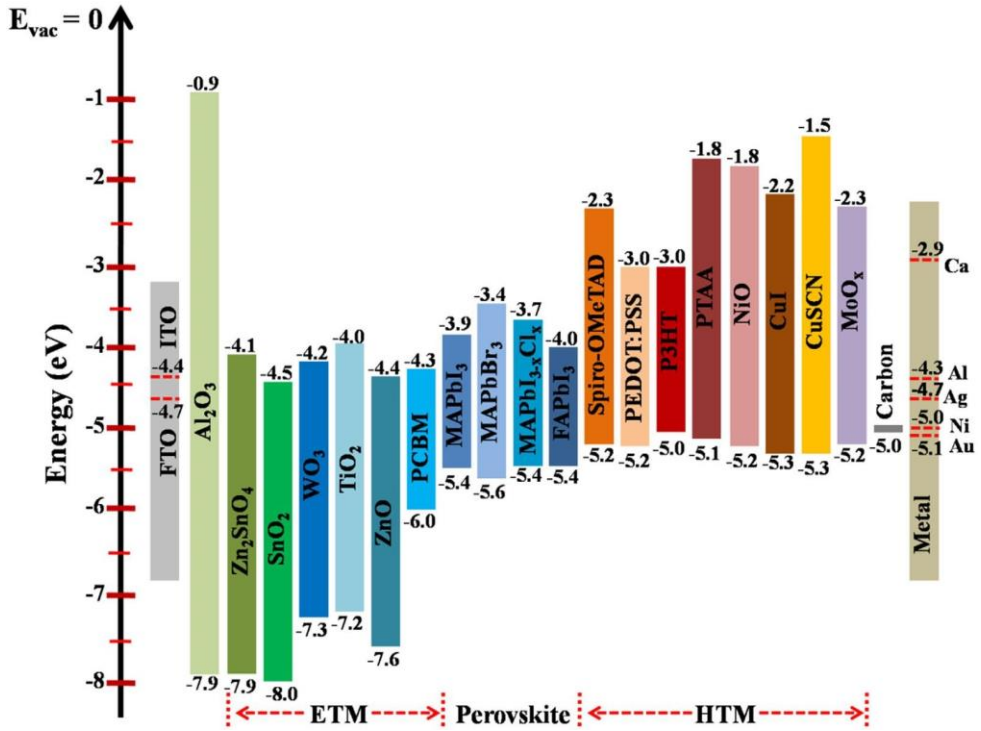

Figure 1.7: Energy level diagram of the materials used in PSCs. [32]

The incident photon to current conversion efficiency is different corresponding to different wavelengths of light. Furthermore, path taken by electrons and holes to produce high PCE requires a well-constructed layered structure to avoid the hole and electron from being slaked before they reach cathode and anode. During the journey the free charge carriers can be seized or recombined by traps and defects in the ETM/HTM layers or perovskite layer due to their internal deficiencies. Hence, interfacial defects of the different layers significantly contribute to charge loss, which further leads to a drop in fill factor, open-circuit voltage (V_{oc}), and short-circuit current (J_{sc}), results poor efficiency. [34] To increase the PCEs of aforementioned devices, it is to optimize charge carrier transport pathway by utilizing new materials with improved fabrication methods which improve interface between layers, controlling the crystallization and morphology formation processes of perovskite films is also important [35]. There are many organometallic halide perovskites have been developed, including $MAPbI_3$, $MAPbBr_3$, $MAPbCl_3$ and $FAPbI_3$ and mixed halides $MAPbI_{3-x}Cl_x$ for PSCs improvement Furthermore PCBM is the most common ETM in inverted planner PSCs, conventional n-i-p used TiO_2, ZnO, WO_3, SnO_2, and $ZnSnO_4$ as ETM. Spiro-OMeTAD, P3HT, PTAA are the mostly used HTM. PEDOT: PSS, is used as HTM in inverted architecture. FTO and ITO substrates are characteristic cathodes with Al, Au or Ag metal electrodes. Sun light is made up of photons (particles of light) that have a range of wavelengths or a range of energies. On the other hand, all materials have different bandgap and according to that they convert solar energy into electrical energy. The energy level diagram of all these different materials is shown in Figure 1.7.

Due to the unique semiconducting and conducting properties of perovskite crystal, such as high optical absorption coefficient, appropriate direct band gap around 1.5eV, ambipolar charge mobility, long carrier lifetime and long carrier diffusion length [36], PSCs have

nowadays obtained a certified efficiency record of 22.7% [19], which is even higher than that of the commercialized polycrystalline silicon.

Tandem solar cells

The single junction thin film commercial silicon solar cells reach nearly 20 % of PCE which is nearly equal to Shockley-Quiesser (S-Q) limit. The S-Q limit is the highest theoretically predicted efficiency of a solar cell for a single p-n junction silicon cell contain band gap of 1.1eV.

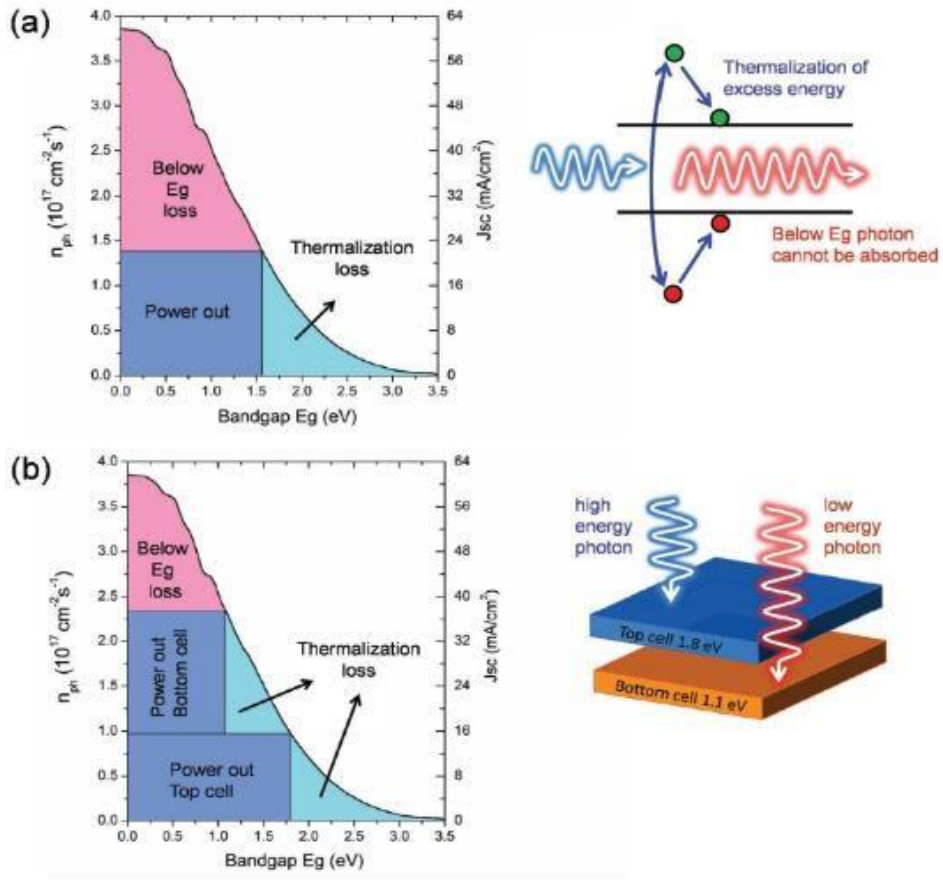

Figure 1.8: Thermalization loss and below-Eg loss of a) a single-junction solar cell with Eg 1.55 eV. b) Dual-junction tandem solar cell with 1.8-eV Eg top-cell and 1.1-eV Eg bottom-cell. [37]

Hence silicon cell converts only that wavelength which is suitable for 1.1eV. The other wavelengths are wasted due to below-bandgap absorption loss and the thermal-relaxation loss of hot charge-carriers (Figure 1.8(a)). It is obvious that we can reach efficiencies more than S-Q limit by combining different band gap materials with silicon cell. Due to this architecture previously, discarded wavelengths are absorbed. Hence joining wide band gap top solar cell with low band gap bottom solar cell in a single cell is the idea of tandem solar cells. Hence the actual absorption window of the tandem solar cells is the wider portion of the solar spectrum. A tandem cell is a unique form of solar cell having more sub-cells, which together convert more of the sunlight spectrum into electricity which results in an increase in overall PCE.

However, it's very fascinating for tandem solar cells to get a high-efficiency wide-bandgap top and bottom cells because the lattice and thermal-expansion coefficient discrepancies between the semiconductor materials. It has been demonstrated that the bottom cell have bandgap around 1.1 eV and the top cell around1.7–1.8 eV (Figure 1.8 (b)) [38]. There are many reasons that make PSCs a promising top cell candidate for tandem cell formation. Initially, PSC attained 22% PCE for a single-junction PSCs. All the perovskites are having charge carrier diffusion lengths more than their optical absorption length Furthermore, perovskite hold huge carrier mobility, stretched carrier recombination lifetime, great defect tolerance and very good high-bandgap absorption hence it is a striking aspirant for tandem top layer application. Secondly, they are very little in price, hence mass construction is inexpensive. Third, tandem solar cells can be fabricated with thin-film technologies, hence several substrates can be used. Fourth, perovskites can be deposited by low-temperature procedures as spin-coating, doctor-blading, slot-die coating, dip coating, screen printing, thermal evaporation, etc., hence reduce the damage to the bottom-cell. Lastly, the bandgap of the perovskite can be tuned in the range 1.17–3.10 eV. [30, 38, 39]

In perovskite/silicon tandem cell, theoretical PCE nearly 40% has been calculated. However, substantial drop in the actual PCE is obtained to be due to the glass reflection and FTO parasitic absorption losses. Actual PCE of dual-junction two-terminal perovskite/silicon tandem solar cell is approximately 30%. [40, 41]. However, due to the very complex fabrication procedure tandem cells are limited to extremely equipped labs.

Limitation of Perovskite Solar Cell

PSC have significant improvement in terms of efficiency from 3.1% in 2009 to more than 22 % in 2018. However, other technology such as CIGS took more than 40 years to attain same PCE [4] Efficiency is important parameters towards commercial application of PSC but there are many other needs to be addressed as well. [32]. In the lab-scale PSCs use metal such as gold (Au), Silver (Ag) Aluminum (Al) as top electrode. These metal electrodes are deposited under high vacuum and high temperature by physical vapor deposition (PVD). The PVD and spin coating processes has been appropriate only for device having dimension of few centimeter (typically between 0.03-0.2 cm^2) hence not feasible for commercially manufactured large solar panels. Moreover, metal electrodes react with perovskite very quickly under oxygen, moisture and heat and participate in the degradation of the device [42, 43]. In addition 2,2′,7,7′-tetrakis-(N, N-di-pmethoxyphenylamine) -9,9′spirobifluorene (Spiro-OMeTAD) has been a commonly used HTM, which has lengthy, expensive synthesis and requires costly sublimation steps for purification and help in degradation of PSCs [44]. Due to this in spite of attaining high efficiency PSCs are very far from commercial manufacturing and issues related to stability and scalability delayed the PSCs commercialization. [45]. Hence fabrication protocol for all the layers which is easily acceptable for large area PSCs manufacturing and top electrode materials those are stable and behaves as a protective casing to make PSCs stable has been

highly desired. [29] which is achieved under controlled environments of lab for small area (less than 1 cm^2) devices but needs to implement for large area perovskite solar cells. Furthermore, these devices should be easily reproducible and must be stable during long term use. Hence, to improve the lifetime of PSCs devices, research effort has been focused on enhancing the device architectures, perovskite material compositions, and manufacturing techniques. [46]

Thesis Outlook

PSCs have become a significant performer in 3rd generation photovoltaics with significant improvement in power conversion efficiency. While with efficiency improvement, there are many concerns regarding the stability and scalability of the PSCs which need to be addressed if they are to be commercialized. To address these issues most stable, yet efficient Monolithic PSCs (mPSCs) are structured. The mPSCs are having compact TiO_2, mesoporous TiO_2, mesoporous ZrO_2, and mesoporous carbon electrode layers in optimal thicknesses on the FTO substrate. Fabrication protocol for all the layers which is easily acceptable for large area mPSCs manufacturing and top carbon electrode materials those are stable and behaves as protective casing to make PSCs stable has been highly desired. Hence, in this project our aim is to optimize top carbon layer and study photophysical processes inside the mPSCs.

This research work is mainly divided into three parts. First part focused on characterization techniques of carbon top electrode for mPSCs. The electrochemical impedance spectroscopy (EIS) measurement for mPSCs has been done in the second part to demonstrated contribution of each layer on the photovoltaic performance of the mPSCs solar cells. The microstructure or morphology of the perovskite crystals inside mesoporous TiO_2, and mesoporous ZrO_2, have significant effect on the mPSCs performance and

stability. Therefore, to achieve high mPSCs device performance, One-dimensional microrods (4mm-5mm) of PbI_2 and $CH_3NH_3PbI_3$ ($MAPbI_3$) is fabricated in the third part of the project.

In Chapter 1, rapid development of PSCs has been briefly presented, with the origin of perovskites as a semiconductor. Moreover, some excellent properties of PSCs which are not observed for traditional solar cells are reviewed in this chapter.

Chapter 2 covers review of state-of-art carbon based mPSCs. Types of carbon have been used in PSCs and recent development in carbon.

Chapter 3 Materials and General Experimental Procedures are explained in chapter 3

Chapter 4 explains carbon film fabrication by screen printing technique and their investigation at different annealing temperatures ranging from 100°C to 400°C. The influence of annealing temperatures on the electrical, morphological and structural properties of the carbon film has been explained. It is shown that a low annealing temperature is good for better adherence of the conductive carbon films, however, temperatures higher than 300°C are required to produce efficient mesoscopic perovskite solar cells. A sintering temperature of 400°C showed the highest device efficiency of 13.2%.

Nevertheless, there is a need to correlate all the physical properties/processes taking place in the mPSCs to gain a deeper understanding of mPSCs operation: What is the role of the contacts? What limits the efficiency of existing perovskite solar cells? How many charge carriers are there in the cell under operating condition? Hence in Chapter 5, EIS spectrum has been described, which is performed on the mPSCs having highest efficiency during previous experiments. The EIS spectrum of mPSCs quantitatively explained the role of contacts, layers, charge generation, drift and diffusion of charge carriers and

recombination. Which further provides insight into performance-limiting physical processes of mPSCs.

For improving mPSCs device, fabrication of one-dimensional microrods (4mm-5mm) of PbI_2 and $CH_3NH_3PbI_3$ ($MAPbI_3$) is explained in Chapter 6. These microrods consist of unique structural and morphological properties and grown at room temperature. The analyses confirm the existence of strong interactions between different stable groups in the crystals. The morphological studies approve crack free morphology of PbI_2 and $MAPbI_3$ micro-rods with porous structure. It is found that the packing of crystals is compact but porous, which represents a novel concept in materials design and synthesis.

In Chapter 7, the main limitations, achievements and conclusions presented in this thesis is summarized. The development of one-dimensional microrods technology towards more stable and low temperature processed mPSCs production is discussed as an outlook.

Chapter 2: Monolithic Review

Introduction

Initially ETL, HTL and perovskite layers have been prepared by spin-coating technique. Porosity and thickness of all the layers are adjusted by different solvent concentration used during the material preparation and adding various fillers. Spin coating and annealing parameters also directs the quality of different layers [30]. It has been foreseeable that the fabrication method and materials have a huge impact on the performance of the PSCs devices, hence Researchers have originate carbon-based materials for top electrode. [47] Carbon materials have many merits including abundant sources, low-cost, high electrical conductivity, water resistance, high chemical stability and flexibility in processing. Carbon work function (5.0 eV) is near to gold (5.1 eV) and have been proved that carbon can work as HTM as well, hence undoubtedly, carbon is an attractive choice to replace metal electrode in PSCs [48]. After this realization PSC scalable fabrication took a very imperative step towards the PSCs large scale stable fabrication [49]. Hongwei Han [50] and group has been made an evaluation in scalable fabrication methods of PSCs and recommended that screen printing and slot-die coating are the maximum promising methods. [50] for roll-to-roll printing. Among the variety of PSCs architectures Monolithic perovskite solar cells (mPSCs) are most promising in association with scalable fabrication because all layers are printed with highly reproducible and morphology controlled methods. This chapter starts with the mPSCs device fabrication and will move towards large scale fabrication. mPSCs long-term stability and efficiency strongly depend upon top carbon layer which has been discussed later. PSCs has reached 22.7 % PCE but mPSCs has been

able to achieve around 14%, hence to improve device further some modification has been suggested at the end.

Mesoporous perovskite solar cell

Carbon-based mesoporous PSCs are primarily segregated into monolithic and planner architecture as demonstrated in Figure 2.1 a and b. However the monolithic architecture is more advantageous than a planner for large area fabrication. [51].

Monolithic perovskite solar cells

Fabrication Technique and Device Structure:

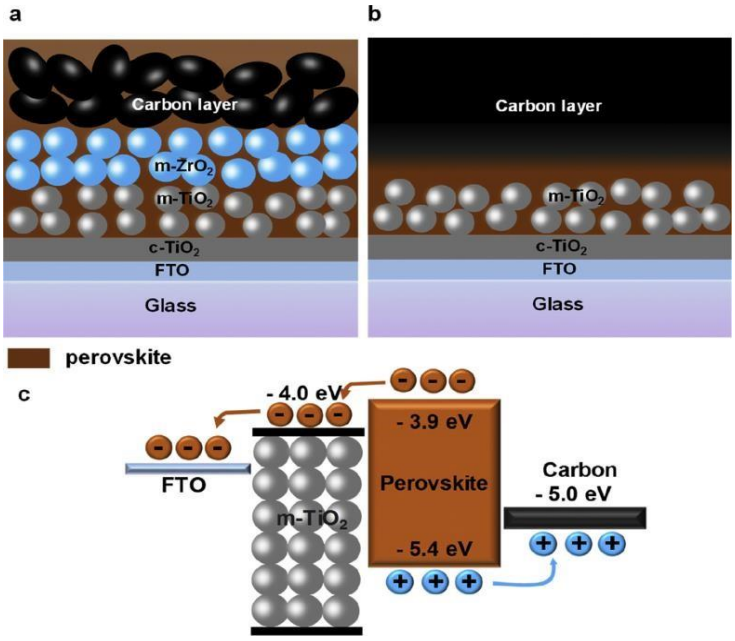

Figure 2.1: Schematic representation of (a) monolithic perovskite solar cell and (b) mesoporous planer perovskite solar e. (c) Energy band diagram of carbon based perovskite solar cell device. [52]

The typical carbon electrode based, hole transport material (HTM) free mPSCs consists three mesoporous layers of Titania ($mTiO_2$) Zirconia ($mZrO_2$) and mesoporous electro carbon (mCarbon). Conductive $mTiO_2$ is acting as ETL, $mZrO_2$ is acting as spacer layer and mCarbon is working as top electrode as well as a HTL. These three layers are fabricated with screen printing technique on the FTO/ITO substrate. A compact TiO_2 is also printed before $mTiO_2$ to provide better electron hole separation. A few metal oxides also have been effectively presented for compact layer fabrication such as SnO_2 and ZnO among which TiO_2 is the most widely used [53, 54]. However Pristine TiO_2 is having many advantages such as low cost, excellent transparency, high chemical stability and suitable conduction band. After printing, all the three layers are annealed around 400°C -500°C sequentially for stabilization High temperature heating allows all the volatile solvent to evaporate fully and built porous scaffolds inside the layer. The Perovskite precursor solution is infiltrated from the top carbon electrode. When all the pores of the three mesoporous layer sip perovskite liquid annealing have been done around 50°C -100°C. By annealing perovskite crystal are built inside the pores of the mesoporous layers. Planner mesoporous PSCs are fabricated by the similar technique as the conventional PSCs using metal electrodes but instead of metal here carbon electrode is used [55]. In this architecture perovskite layer is printed by spin coating or dip coating at mesoporous TiO_2 then the carbon layer is printed on top. Here we concentrate more on the fabrication of mPSCs and various types of carbon used in mPSCs architecture. [52]

Working Principle:

mPSCs generate electricity according to the following mechanism (Figure 2.1 c): On light absorption by sunlight, the perovskite crystal excites and absorb photons and generated electron/hole pairs. The conduction band of perovskite is around 3.9eV (slightly

different for different kind of perovskites) is higher than the conduction band edge of TiO_2 which is -4.0 eV. Photo generated electrons charge carriers in the perovskite are injected into the conduction band of the electron selective $mTiO_2$ layer and collected by the anode. Furthermore, the valence band edge of perovskite (-5.4 eV) is lower than the work function of carbon layer which is -5.0 eV. Holes are transported to the valence band of the perovskite to hole selective carbon layer and further collected by the cathode of the external circuit creating the flow of electric current. The arrangement of different energy levels for the mPSCs three functional layers are shown in figure 2.2. In order to increase the PCE of a aforementioned device, a general strategy is to optimize charge carrier transport pathway by utilizing new materials with accurate fabrication approaches. Fabrication approach include optimized of mPSCs by changing the thickness of the three layers and the viscosity conformation of the paste used for printing of compact and $mTiO_2$, $mZrO_2$ and mcarbon layers. Hence, performance of mPSCs depend upon various factors such as sufficient infiltration of the perovskite precursor [56], additive in perovskite quality of the perovskite materials [57], the size of TiO_2 particles [58] and the thickness of ZrO2 [59] thickness and capping of carbon layer. [60]

Review on mPSC:

A monolithic device with three mesoporous layer architecture having mesoporous counter carbon electrode made with carbon black and graphite composite was first reported by Kay and Grätzel [61] in1998. Here they produced a new type of dye sensitized photovoltaic module. Individual photoelectrochemical cell (shown in Figure 2.2 a) of this module is having a monolithic architecture and connected in series. Each solar cell element includes three mesoporous layers on a transparent SnO_2 conducting substrate on glass.

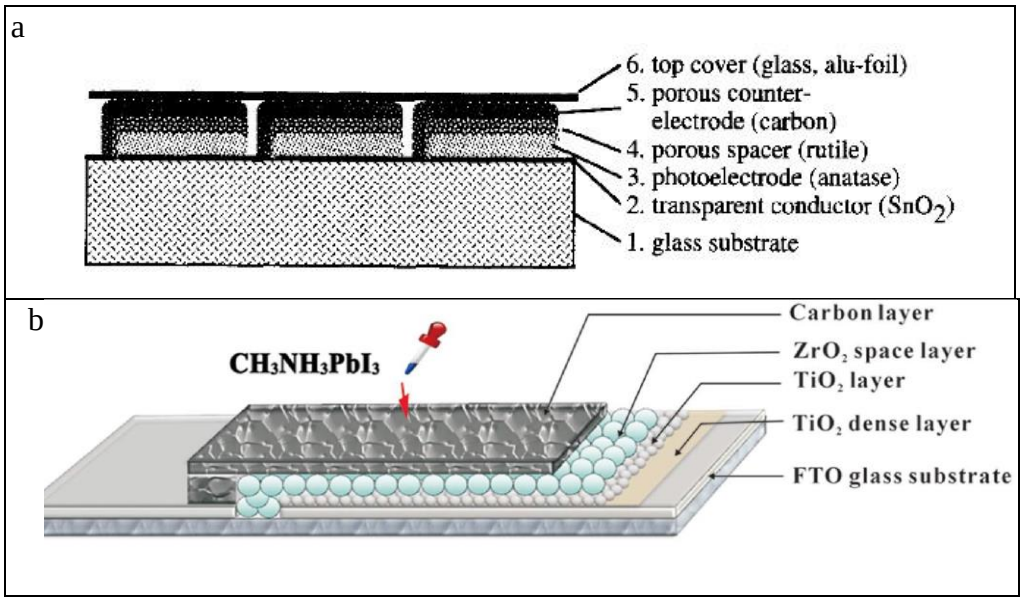

Figure 2.2: (a) Kay and Grätzel reported cross sectional representation of the liquid electrolyte used monolithic dye sensitized solar cells [61]. (b) A schematic representation of solid state mPSCs device using perovskite as photo sensitizer.[49]

First 10 µm layer is made of nanocrystalline TiO_2 having mean particle size of TiO_2 around 25 nm, second layer is an insulating layer act as a spacer made up withZrO_2, and the homologue of TiO_2, with a particle size below 20 nm, and a CE of graphite powder and carbon black made with graphite powder 20% by weight, carbon black 15% and TiO_2 is used as binder to obtain carbon paste.

The pores of mesoporous layers have been filled with a redox electrolyte containing iodide for transporting the electron and holes between the SnO_2 and carbon respectively. These individual monolithic cells show 6.67% PCE. Further series connection of the mPSCs on the SnO_2 substrate is accomplished to obtain solar cell module in non-vacuum produce 5.29% PCE in 21.67cm^2 area [61]. This work successfully shows working of

monolithic device and also provide sufficient background to print monolithic solar cell module for scale up fabrication However this module is having drawbacks associates with liquid electrolyte. The thickness of carbon layer is increased twice after liquid absorption Hence this liquid mPSCs is further modified into solid state mPSCs.

In 2013 Hongwei Han and group [49] reported first solid state mPSCs device with a PCE of 6.64% This solar cell used two types of graphite carbon black/spheroidal graphite which produced 6.64%, PCE and flaky graphite reported 4.08% PCE. Their device also shows more than 800 hours of stability under room temperature darkness. The spheroidal graphite electrode has more loose or spongy morphology of graphite in comparison flaky graphite electrode which shows morphology of graphite sheets which has been piled over the ZrO_2 layer. Hence the monolithic cell made-up by spheroidal graphite shows better performance than the flaky graphite and provide a better pore-filling in the $mTiO_2$ and $mZnO_2$ layers [49]This work initiated the research to low-cost carbon back electrode based mPSCs. $CH_3NH_3PbI_3$ perovskite accomplished task of light harvester as well as a hole conductor, hence PCE of 6.64%, is obtained which is not higher than the conventional nobel metal-based PSCs. But the fabrication method is simpler, and stability is better than the conventional PSCs. Later, the group did a series of research to improve carbon electrode based HTL free mPSCs.

For improving PCE, in next work ordered mesoporous carbon (OMC) has been mixed with flaky graphite to prepare a carbon paste which employed as an electrode for mPSCs. OMC is extensively used as electrode for electrochemistry applications, due to its good surface, consistent and tunable pore sizes, and physicochemical properties, but due to its low conductivity it is not suitable alone for mPSCs electrode hence mixed with graphite to form a paste. The OME and graphite is mixed in two dissimilar ratios and two carbon paste is prepared named OG15 and OG16. PCE of 7.02% is reported with OG15 and 6.3% for

OG16 carbon paste. The improvement in efficiency is mainly due to the improvement in the fill factor of the device [62]. For further improving device they used TiO_2 nanosheets and employ two step sequential deposition of perovskite liquid. Initially, PbI_2 were infiltrated by spin coating them mPSCs dipped in to MAI solution for 10 minutes. This process enhances the electrical linking between layers hence 10.64 % PCE obtained. [63] which enhanced to 11.6% by optimizing the thickness of the carbon counter electrode and the size of flaky graphite particle used in carbon slurry preparation [64]. For improving PCE of mPSCs many works has been done which introduced additives on perovskite liquid and optimize device engineering.

Table 2.1: Summary of the device performance depend upon mesoporous layer thickness, type of carbon perovskite and its infiltration method on the HTM-free mPSCs.

S. No	$mTiO_2$ Thick (µm)	$mZnO_2$ Thick (µm)	mCarbon Thick (µm)	Type of carbon	Perovskite	Infiltration	PCE (%)	Year	Reference
1	10	10	60	graphite/carbon black paste (GCBP)	NA	NA	6.67	1996	[61]
2	1	1	10	spheroidal graphite	$CH_3NH_3PbI_3$	1 step	6.64	2013	[49]
3	1	1	10	flaky graphite	$CH_3NH_3PbI_3$	1 step	4.08	2013	[49]
4	1	2	NA	OG15	$CH_3NH_3PbI_3$	1 step	7.02	2014	[62]
5	1	2	NA	OG16	$CH_3NH_3PbI_3$	1 step	6.3	2014	[62]
6	0.6	1	10	Carbon slurry	PbI2 →MAI	2 step	10.64	2014	[63]
7	1	2	10	(GCBP)	$(5\text{-AVA})_x(MA)_{1-x}PbI_3$	1 step	12.84	2014	[57]
8	0.4	0.5	5	(GCBP)	PbI2 →MAI	2 step	9.79	2015	[64]

S. No	$mTiO_2$ Thickness (µm)	$mZnO_2$ Thickness (µm)	mCarbon Thickness (µm)	Type of carbon	Perovskite	Infiltration	PCE (%)	Year	Reference
9	0.4	0.5	7	GCBP	PbI2 →MAI	2 step	10.02	2015	[64]
10	0.4	0.5	9	GCBP	PbI2 →MAI	2 step	11.63	2015	[64]
11	0.4	0.5	12	GCBP	PbI2 →MAI	2 step	10.56	2015	[64]
12	0.4	0.5	15	GCBP	PbI2 →MAI	2 step	10.53	2015	[64]
13	2	1	9	GCBP	PbI2 →MAI	2 step	12.7	2015	[65]
14	1	2	10	GCBP	$(5\text{-AVA})_x(MA)_{1-x}PbI_3$	1 step	13.41	2015	[58]
15	0.5	0	10	GCBP	$CH_3NH_3PbI_3$	1 step	1.56	2015	[59]
16	0.5	0.3	10	GCBP	$CH_3NH_3PbI_3$	1 step	5.92	2015	[59]
17	0.5	0.5	10	GCBP	$CH_3NH_3PbI_3$	1 step	9.02	2015	[59]
18	0.5	1	10	GCBP	$CH_3NH_3PbI_3$	1 step	10.30	2015	[59]
19	0.5	1.4	10	GCBP	$CH_3NH_3PbI_3$	1 step	9.29	2015	[59]
20	1	2	10	GCBP	$(5\text{-AVA})_x(MA)_{1-x}PbI_3$	1 step	12.9	2015	[66]
21	0.4	1.5	10	GCBP	CH3NH3PbI(3-x)(BF4)x	1 step	13.24	2016	[67]
22	1	2	10	GCBP	$CH_3NH_3PbI_3$	1 step	13.89	2016	[56]
23	0.5	2	10	carbon paste	$CH_3NH_3PbI_3$ +LiCl	1 step	14.5	2016	[68]
24	0.3	0.6	15	GCBP	$CH_3NH_3PbI_3$	1 step	7.2	2016	[60]
25	1	2	10	carbon paste	$MAPbI_3$ *x*GuCl	1 step	14.35	2017	[69]
26	0.3-0.6	1-2	10-12	Commercial carbon paste (CCP) (Solaronix)	$(5\text{-AVA})_x(MA)_{1-x}PbI_3$	Inkjet	8.15	2017	[70]
27	0.3-0.6	1-2	10-12	CCP	$(5\text{-AVA})_x(MA)_{1-x}PbI_3$	Inkjet	6.56	2017	[71]
28	0.3-0.6	1-2	10-12	CCP	$(5\text{-AVA})_x(MA)_{1-x}PbI_3$	Inkjet	14.3	2017	[72]
29	1	2	10	CCP	$(5\text{-AVA})_x(MA)_{1-x}PbI_3$	1 step	14.02	2017	[73]

In 2014, Hongwei Han [57] and group again come with a benchmark work which push mPSCs towards the stability and scalability, they (Mei et al) infiltrated mesoporous layers of TiO_2, ZrO_2, and carbon from a mixed-cation perovskite $(5AVA)_x(MA)_{1-x}PbI_3$ to substitute $MAPbI_3$. The perovskite solution has been formed in two steps, first by mixing 5-ammoniumvaleric acid iodide (5AVAI) with methylammonium iodide (MAI) in 1:20 and 1:30 molar ratios this solution is further mixed with lead iodide (PbI_2) in γ-butyrolactone. Organized 5-AVA^+ cations swapped MA cations in the cuboctahedral location of conventional perovskite and creating novel mixed-cation perovskite with orthorhombic phase. The 5-AVA molecules formed extended hydrogen-bonded chains among COOH and $NH3^+$ groups and I^- ions from the PbI_6 octahedra, which behaves as a stimulating agent to produce mixedcation perovskite $(5\text{-}AVA)_x(MA)_{1-x}PbI_3$. Crystals made with this hybrid perovskites have lesser imperfection and provide improved pore filling across TiO_2, ZrO_2, and carbon scaffolds hence create better crystallinity network between the layers. Due to this at photoluminescent, produced charges are having in a longer exciton lifetime and a higher quantum yield. This mPSCs have shown controlled certified PCE of 12.84%, with very less hysteresis and good J_{sc} of 22.8 mA/cm^2. This device is tested under 1 sun without any encapsulation and have shown stability more than thousand hours hence thick carbon layer provide strength to mPSCs absence of HTM layer further improve stability of the device. The 5-AVA cations govern development of perovskite crystals in the deep porous cavities of TiO_2 layer and encourage superior crystal development in the regular direction. The device made with conventional $MAPbI_2$ perovskite shown unfilled nanopore of mesoporous layers which is due to the precipitate formation of $MAPbI_2$ perovskite before crystallization. [57]

After this initial work many reports has been reported to improve device by improving each layer and with trying different additives in the perovskite liquid.

Mesoporous TiO_2 layer

Another crucial component of a good mPSCs is the size of TiO_2 particle in the mTiO_2 layer, hence Hen and group performed characterization of mPSCs mixed-cation perovskite $(5\text{-AVA})_x(MA)_{1-x}PbI_3$ based device.to optimization of the size of TiO_2 nanoparticle. The four sizes diameter (10,15,20,25 nm) of TiO_2 nanoparticle have been used to fabricate TiO_2 mesoporous layer. The results for overall mPSCs device show that the size of TiO_2 nanoparticle guide perovskite liquid during infiltration and help to provide good contact between perovskite liquid and TiO_2 particles. Furthermore $(5\text{-AVA})_x(MA)_{1-x}PbI_3$ crystal and TiO_2 nanoparticle interface after crystallization have significant impacts on the charge transfer characteristics of the device. The best 13.4% PCE is obtained with optimized size of 25nm TiO_2 nanoparticles. [58]

Mesoporous ZrO_2 layer

Next critical parameter needs to be studied is the thickness of ZrO_2 spacer layer. Here Liu and group made device having ZrO_2 thickness of 0,.0.3, 0.5, 1 and 1.4 µm. Maximum efficiency has been obtained with 1 µm thickness. In this work temperature of perovskite precursor solution and temperature monolithic substrate at the time of perovskite infiltration have been also studied. Furthermore, by keeping 70°C temperatures of substrate and precursor solution 12.34% PCE is obtained. Champion device fabricated under controlled parameters such as filling volume of perovskite ZrO_2.thickness, experimental temperature,

shows 13.14 % efficiency. However maximum short circuit current is obtained with 1.4 µm device. [59]

Effect of chemical solvents on perovskite precursor

Effect of different chemical solvents being used during the preparation of the perovskite precursor solutions studied by Chen and group in the next step. With contact angle measurement technique various polar solvents such as DMF, DMSO, γbutyrolactone (GBL), and1-methyl-2-pyrrolidinone (NMP), wettability has been studied DMF. The stability of intermediate phase and mPSC performance has been thoroughly examined and found that DMF and DMSO are the better characteristics than GBL and NMP. For further characterization DMF and DMSO was mixed in proper proportion hence champion device produce 13.89 % PCE. In this work it has been proven that wettability of perovskite precursor solution on mesoporous layers of mPSCs is strongly influenced by polarity and viscosity of solvents. [56]

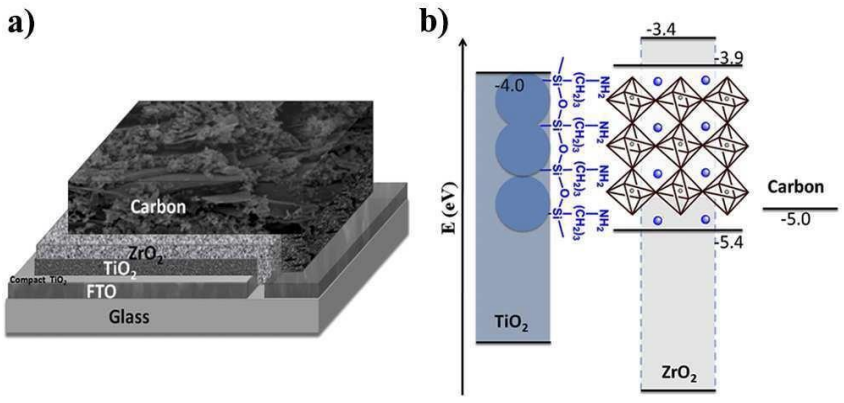

Figure 2.3: (a) The schematic structure of fully printable mPSC having carbon as top electrode; (b) energy band illustrations of the mPSC device and organic silane self-assembled monolayer between TiO_2 surface and perovskite. [65]

Surface Modification

Liu and group enhance TiO_2 and perovskite interface by introducing a self assembled organic silane monolayer. The mPSCs has been immersed in aminopropyltrimethoxysilane ($C_6H_{17}NO_3Si$ /0.05mM) in 2-propanol solvent for few hours to build silane monolayer then washed in 2-propanol and dried under nitrogen. This process form contacts between titanium and silicon and by forming Ti-Si bonds and attaching $NH_2(CH_2)_3$ across the perovskite (Figure 2.3). This surface modification of mesoporous TiO_2 not only enhance band alignment between the mesoporous layers but, also passivate the recombination of charges at the center of layers hence able to produce 12.7% PCE. [65]

Additives in perovskite liquid

5AVAI has been used as additive in $MAPbI_2$ perovskite liquid and improved device performance significantly, after this many additive have been tried and tested by researchers, because the crystallinity and morphology of perovskite crystal trapped inside the mesoporous boundaries has been enhanced after adding some additives in the perovskite precursor solutions result in a perovskite crystal with reduced imperfections and passivated boundaries and improve charge carrier loss. Chen et al. [67] developed a mixed-anion perovskite $CH_3NH_3PbI_{(3-x)}(BF_4)_x$. They reported that replacement of I^- by BF_4^- expressively enhance light harvesting ability, carrier concentration and conductivity of the device which results boost in PCE 10.54% (with $CH_3NH_3PbI_3$) to 13.24%. (with $CH_3NH_3PbI_{(3-x)}(BF_4)_x$) [67].

For further improving perovskite solution pore filling Sheng et al [68] mixed Lithium chloride (LiCl) with perovskite solution in 10, 20, and 30 wt%. The LiCl mixed perovskite superior revealed higher electronic properties because conductivity of perovskite layer due

to quicker electron transference. With 30 wt% of LiCl in perovskite precursor mPSCs improved PCE of 14.5% attained.[68] Further an additive guanidinium chloride (GuCl) (Figure 2.4) which can expand charge carrier lifetimes and reduce charge carrier loss in mPSCs when added with $CH_3NH_3PbI_3$,has been introduced by Hou et al.[69]. The Gu cation-built a cross link connection between the adjoining jots of perovskite shown in figure 2.4 results no cracks in perovskite crystal. Besides, it has been experienced that iodide ions are having inferior electronegativity than the chloride ions leading less extracted electron concentration out of the protons, which results upfield swing in the resonance signals. Therefore, the open-circuit voltage (V_{OC}) of the mPSCs has been improved from 0.88 V to 1.02 V with 14.27% PCE. [69]

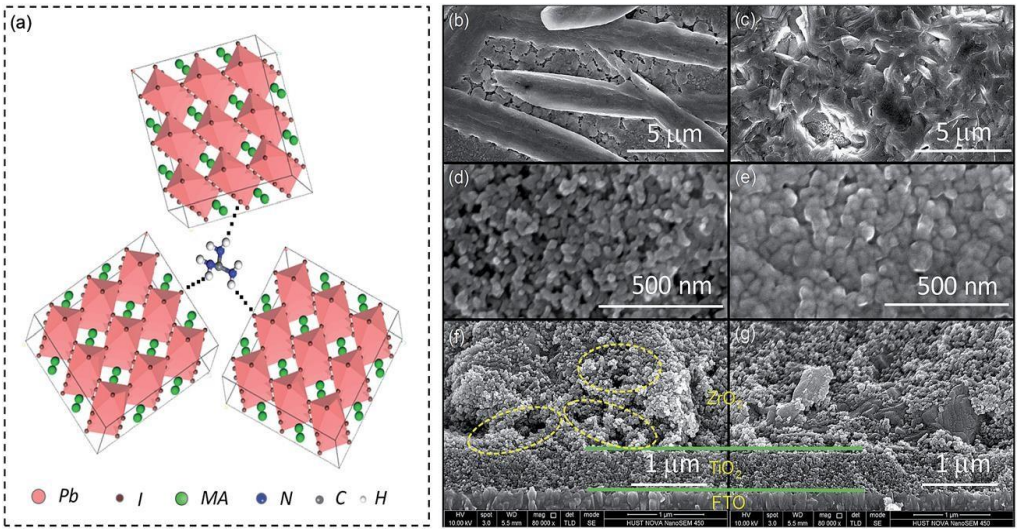

Figure 2.4: (a) Representation of crosslinked perovskite grains under the influence of GuCl. (b and c) SEM images of $MAPbI_3$ and $MAPbI_3$ xGuCl films on FTO substrates. (d and e) SEM images of $MAPbI_3$ and $MAPbI_3$ xGuCl infiltrated $mTiO_2$ layer; (f and g) cross sectional SEM images of the m TiO_2 and $mZrO_2$ with $MAPbI_3$ and $MAPbI_3$ xGuCl (x=0.25) perovskite.

Long term Stability

To validate the feasibility and stability of the triple mesoporous mPSCs architecture. Li and group have done wide investigations. The mPSCs device has been under test for a week in desert atmosphere of Jeddah, Saudi Arabia further device is kept in an oven around 85°C continuously for heat stress test for 3 months. To further determine light soaking photostability of the mPSCs device are kept under 1 sun illumination in argon environment around 45°C. The device also kept for 45 days at their highest power point and V-I characteristics were recorded in every 6 hours.

Under all above stress conditions stated above mPSCs device have shown consistent efficiency. [66]

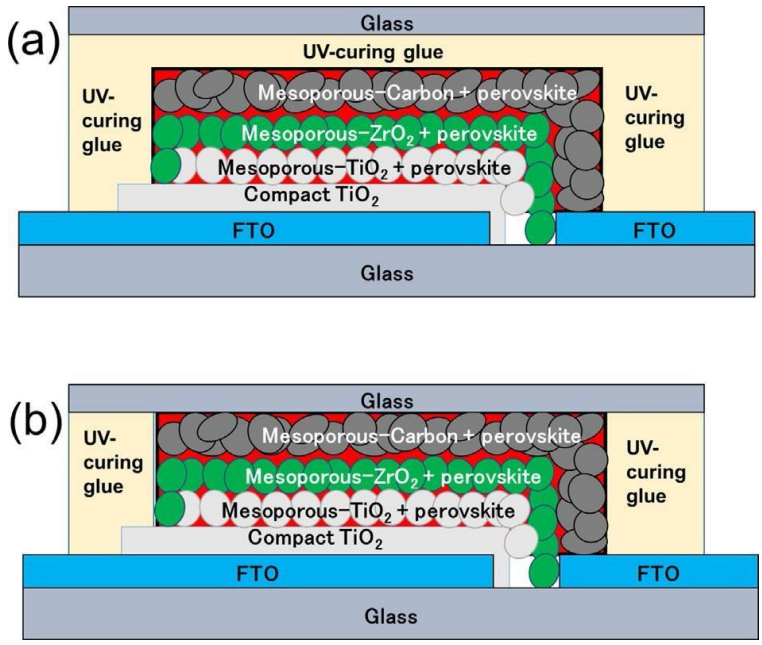

Figure 2.5: Schematic diagram of fabricated mPSCs with encapsulation: (a) over-sealed and (b) side-sealed cell. [60]

Thermal stability is further investigated by the Baranwal et al with a encapsulated mPSCs for 1500 hours at 100 °C They demonstrated that with UVcurable encapsulation shown in Figure 2.5 and thick carbon layer (~15 µm) device withstand under temperature as high as 100 °C. However, encapsulation of device with this resin trigger inner decomposition. [60]

Inkjet Infiltration of Perovskite Precursor

For perovskite infiltration usually, one-step drop casting or two-step dip coating deposition methods has been used. However, this manual perovskite infiltration methods are not applicable for large-scale commercial fabrication of mPSCs, which has been feasible for small area (around 1.5 × 1.5 cm^2) devices. Hence Hashmi et.al. [70-72] performed series of work to address issue of manual perovskite precursor solution across mPSCs and stability of device during operation.

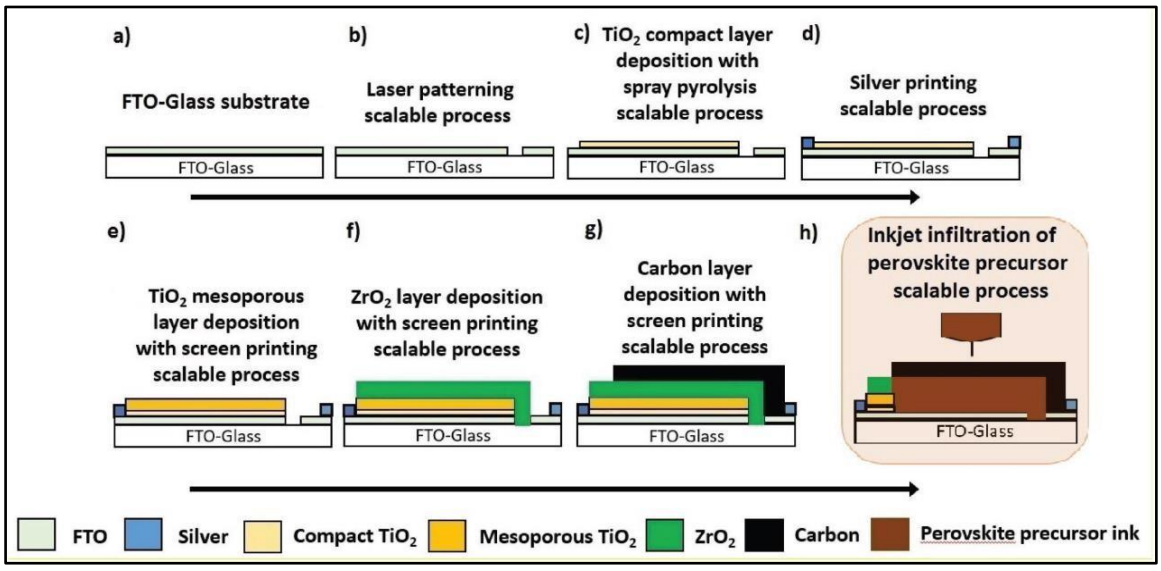

Figure 2.6: Illustration of Fully printable scalable process for mPSCs fabrication. (a-b) FTO in glass substrate and its patterning through laser. (c) c-TiO_2 printing. (d-g) screen printing of silver anode and cathode, mesoporous TiO_2,ZrO_2 and carbon electrodes. h) inkjet infiltration of perovskite precursor solution of fixed volume. [70]

Fully printable mPSCs are first time printed in ambient conditions with inkjet infiltration (Figure2.6) of perovskite. 5-AVAI perovskite additive played a crucial role in the inkjet printing of perovskite. $MAPbI_3$ alone crystalize very quickly hence choke nozzles of printer cartridge, however mixed-cation perovskite $(5\text{-}AVA)_x(MA)_{1x}PbI_3$ significantly slow down the precursor solution crystallization during the deposition of perovskite hence, prevent printer clogging. With the help of this highly reproducible device has been fabricated having 8.15% PCE. These devices withstand for 1046 hrs for extended light soaking stability test at 35 °C under 1 sun without any degradation [70]. Same mPSCs devices (on and off shielding) are tested for intense ultra-violet light soaking for 1002 hrs under 1.5 Sun UV light illumination with 150160 µm of epoxy is coated all over the mPSCs and dried under vacuum overnight before the UV radiation. mPSCs with epoxy shows thousand hours of stability under radiation and humidity. [71] To improve PCE of these inkjet infiltrated mPSCs Hashmi et.al [72] report humidity assisted thermal exposure (HTE) as a post treatment The device kept for 200 hours under THE and shown significant enhancement in the average PCE of the mPSCs from 9% to 13.1% champion device shown 14.3% efficiency with high reproducibility. [72]

Large Area Monolithic perovskite solar cell

Regardless of having remarkable photovoltaic performances with PCE more than 22%, PSC are not at all stable when exposed to environment, failing to fulfill market requirements. Various technological approaches have been proposed to overcome the scalability and instability problem, which, while delivering appreciable incremental

improvements. The development done on mPSCs large area printing has been explained below.

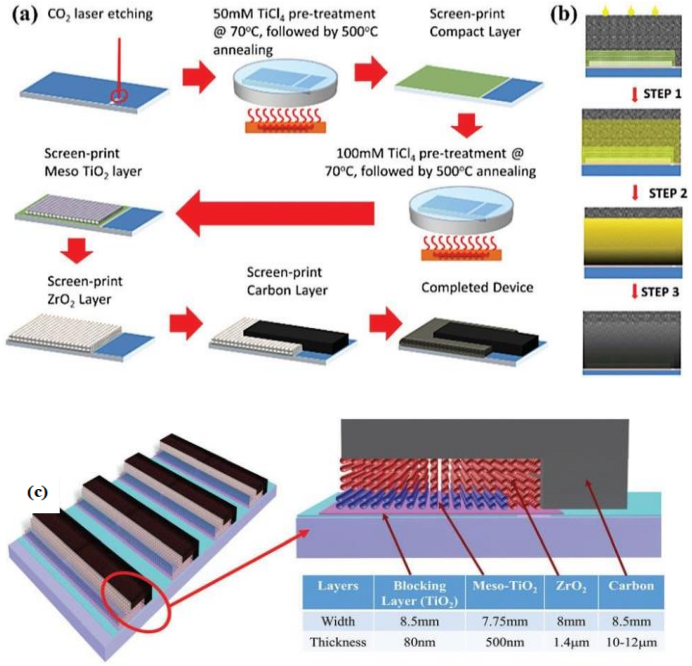

Figure 2.7: (a) Step by step fabrication of Monolithic solar cell modules using screen printing (b)Step1:Perovskite infiltration across porous layers and resting of precursor solution for 1 hour for enhanced pore filling, Step 2 and 3 Heating at 50 0°C for one and half hours allow appropriate development of perovskite crystals and further heating at 60°C for half an hour ensure (c) Graphic illustration of the mPSC module having sizes 5 cm^2 × 10 cm^2 with active area of 31cm^2.[75]

Priyadarshi et al. first demonstrated the construction of mPSCs modules of dimensions 5 cm^2 × 10 cm^2 with an active area 31 cm^2 and 10 cm^2 × 10 cm^2 with an active area 70 cm^2carbon based stable large area monolithic perovskite solar modules (PSMs) with an active area of 70 cm^2 by simplistic semi-automated screen-printing process (Figure 2.7). To prove the importance of characteristics of top mesoporous carbon layer towards the development of high efficiency mPSCs in this work three types of carbon paste were used. Paste one and two are obtained by blending around 500nm size carbon with binder (ethyl cellulose) and oil (terpineol) in different weight ratios. Oil is necessary to provide good

dispersion of particles, however reduced quantity of binder enhances conductivity of the film. Third paste is commercial paste provided by DYESOL, Australia. Furthermore, all tiny details that are important to fabricate good mPSCs device are explained in detail. They described that for proper filling of perovskite liquid inside meso ZrO_2 and meso-TiO_2 droplet size and drop timing of perovskite should be optimum. Supreme pore filling within the pores governs by many other parameters, such as wettability and the relative attraction of the liquids to the solid. It has been discovered that with improving the wettability of the infiltration fluid pore filling enhances on the contrast deteriorates as the flow rate of liquid increases and viscous uncertainties become prominent. [74].

After pore filling annealing is also important part for good quality crystal formation This step is very critical because it assist to enhance the quality of interconnection between the TiO_2 / ZrO_2 layers and ZrO_2 / carbon layers. High quality perovskite crystal with good interface provide barrier for recombination. Here drop volume was 1.5 µl for optimum pore filling. Also, the location of the droplet at large area and release time is important. The comprehensive studies about dispersion and absorption of perovskite liquid in pores indicate that the size of droplet and viscosity of liquid and pore size and surface area of mesoporous layers which provide capillary flow for liquid are very important [76, 77].

Moreover, perovskite infiltration from sides of the printed layers has not been worked, because horizontal diffusion of liquid from the point of dispersion to the other end leads by capillary action which is more prominent in large area devices. After keeping all above stated constraints the active area 31 cm^2 mPSCs has given 10.46% PCE and active area 70 cm^2 mPSCs has produced 10.75% PCE.%. Both device shows excellent stability with standard deviation of 0.01% in PCE for more than 2000 hours under ambient conditions. [75, 78]

Optical and electronic properties of perovskite crystals are greatly tunable according to the perovskite crystal structure. Hence by applying concept of crystal engineering and supramolecular synthons 2D perovskite have been realized by mixing protonated salt of aminovaleric acid iodide ($HOOC(CH_2)_4NH_3I$) inshort AVAI with PbI_2 results low-dimensional perovskite $(HOOC(CH_2)_4NH_3)_2PbI_4$ structure. An ultrastable 2D/3D perovskite $(HOOC(CH_2)_4NH_3)_2PbI_4$ /$CH_3NH_3PbI_3$ junction can be formed by engineering both 2D and 3D perovskites (Figure 2.8).

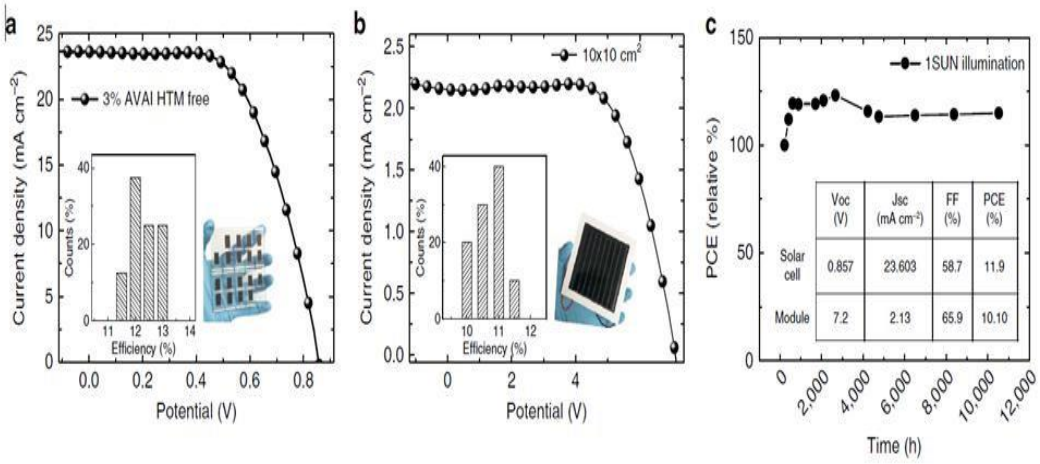

Figure 2.8: 2D/3D mPSCs characteristics and stability. (a) J–V curve with 2D/3D perovskite using 3%AVAI in mPSCs under ambient conditions 1 sun (small are device statistics in the inset). (b) J–V curve with 2D/3D perovskite using 3%AVAI in 10×10 cm^2 mPSCs large area module (Solar module statistics in the inset). (c) mPSCs module stability test under 1 sun AM and 55 and at short circuit conditions. [79]

By using this 2D/3D perovskite one-year ultra-stable mPSCs have been prepared by G. Grancini et.al. .This perovskite is having gradually-organized multidimensional

interface which result 14.6% efficiency in standard mesoporous solar cells. To validate the up-scale probability 10×10 cm^2 solar modules have been fabricated in a fully printable 3-layer TiO_2/ZrO_2/Carbon mPSCs architecture and drop casting has been performed to infiltrate 2D/3D giving 11.2% PCE, which is stable for more than 10,000h with no performance degradation measured under controlled standard conditions. It has been found that confined structure of lower dimension perovskite crystal gives more flexibility while tuning parameters This innovative stable and low-cost architecture will enable the timely commercialization of mPSCs. [79]

Similar mPSCs module with 10 × 10 cm^2 size having 10 sub mPSCs with total active area of modules 49 cm^2 prepared by Hu et.at. [69] (PSM) Each unit cell shows 14.02% PCE and 10.4% PCE for module under 1 SUN. For checking stability of modules device are checked under 1sun for 1000 hours, outdoor in China for 1 month and 1 year under dark. Active. During all mentioned different condition devices have shown good stability. This paves the way for the fabrication of efficient and stable large-area mPSC modules for commercialization. [69]

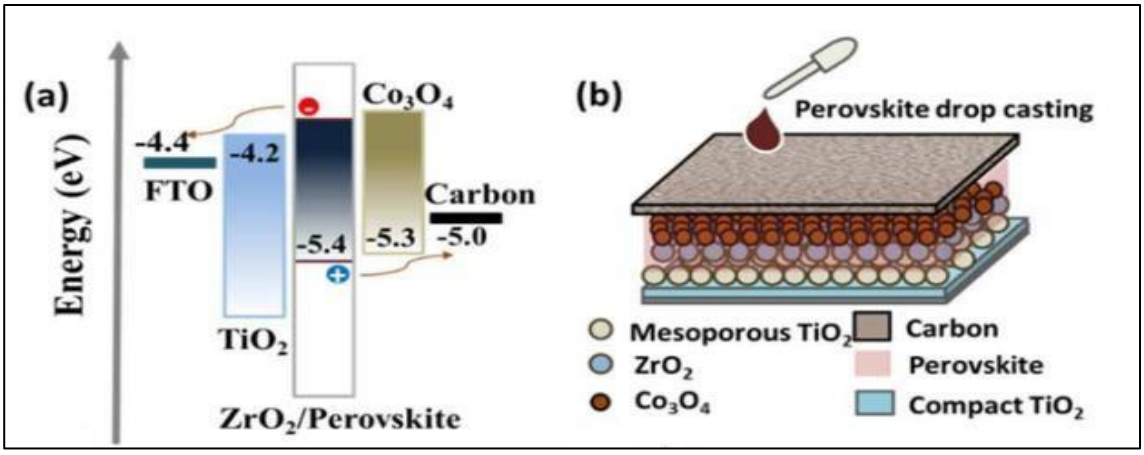

Figure 2.9: (a) Energy band diagram, (b) schematic illustration of the $MAPbI_3/ZrO_2/Co_3O_4$/Carbon mPSCs device. [80]

Bashir et.al. introduced an inorganic interlayer of spinel cobaltite oxides (Co_3O_4) as hole transport material in mPSCs architecture which can greatly enhance mPSCs performance for 70 cm^2 active area mPSCs module. The device has shown 13.27% efficiency along with long-term stability, up to 2500 hours under ambient conditions with almost no hysteresis. [80]

Table 2.2: List of large area carbon-based top electrodes for hole transport layer free printable mPSCs

S. No	$mTiO_2$ Thick (µm)	$mZnO_2$ Thick (µm)	mCarbon Thick (µm)	Perovskite	Infiltration	Active Area (cm^2)	Stability (hours)	PCE (%)	Year	Reference
1	0.5	1.4	10-12	$(5\text{-AVA})_x(MA)_{1-x}PbI_3$	1-Step	31	2000	10.46	2016	[75]
2	0.5	1.4	10-12	$(5\text{-AVA})_x(MA)_{1-x}PbI_3$	1-Step	70	2000	10.74	2016	[75]
3	1	2	10	$(5\text{-AVA})_x(MA)_{1-x}PbI_3$	1-Step	49	1000	10.4	2017	[69]
4	1	2	10	$(AVA)_x(MA)_{1-x}PbI_3$	1-Step	47.6	12000	11.2	2017	[79]
5	0.5	1.3	10-12	$(5\text{-AVA})_x(MA)_{1-x}PbI_3$	1-Step	70	2500	11.06	2018	[80]

Carbon Electrode

The success mPSCs device is greatly depend upon top carbon electrode. According to the fabrication engineering, carbon electrode must be high in conductivity, have large

pore size so that perovskite solution has been allowed to infiltrate till TiO_2 layer easily and cover the TiO2 surface easily, [81]. Apparently, the top electrode in mPSCs must possess good electrochemical activity and high lateral conductivity [82]. To make mPSCs device perform better, many researchers has been focused on the ingredients of carbon paste recipe which is mainly carbon material and binders used to make paste.

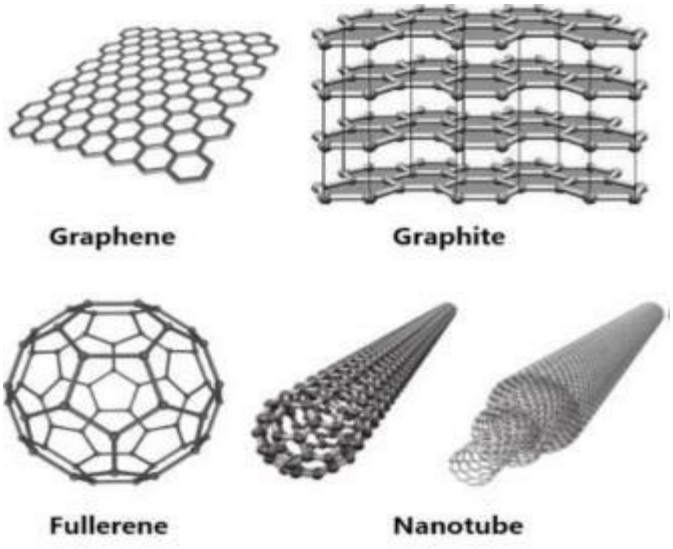

Figure 2.10: Structure of various carbon materials. [83]

Carbon materials are differentiated according to the bonding pattern and crystalline structures of the carbon atom According to the single, double or triple bonded carbon atom the, allotropes of carbon are having very different chemical and physical properties. Carbon is broadly divided into diamond graphite and fullerene However, according to the application PSCs are using various modified form of carbon which is derivatives of fullerene and graphene, single wall and multiwall carbon nanotube, and conductive carbon

paste and inks. Depend upon their diverse electric parameters and energy orientations, these carbon-based materials can be used as electron transporting layer, hole transporting layer, modifier to improve interface between the layers and charge collecting top electrode. [84, 85]

Graphene prepared from graphite, a single-layer 2D carbon nanosheet, possesses many intriguing properties, such as great charge mobility, stability and electrical conductivity. It is one of the hottest subjects in materials science, chemistry and physics, due to its various application in transparent conducting films (TCF), optoelectronic devices and energy storage. Graphene have derivatives, graphene oxide (GO) and reduced graphene oxide (rGO), is considered as a promising support material for metal catalysts. Energy-storage applications of graphene found both as active components in batteries and supercapacitors, and inactive components (conductive additive or substrates for electrochemically active particles). Anodes of lithium-ion batteries and electrodes of electrochemical capacitors are among the most studied applications. Graphene and graphene derivatives have been utilized as templates for the synthesis of various noble-metal nanocomposites. [86, 87]

Carbon paste, often used for electrode printing, is primarily prepared by carbon black and graphite powder and a binder (pasting liquid). Graphite is soft, soapy, hexagonal layered crystal with superior features such as high-temperature resistance, excellent electrical and thermal conductivity, lubricity, corrosion and thermal shock free [88, 89]. All these characteristics of the graphite are very vital for the stable performance of the corresponding device when employed as electrodes [90]. Carbon paste-based electrodes are reproducible and easy to tune which is very important for large-scale commercial production [91, 92]. In context of PSCs the water resistance property graphene surface would offer protection against humid air moisture from the environment which further

improve lifetime performance of the devices. Graphene can be used as charge transport layer, stabilizer and top electrode in high performance stable PSC. [93, 94]

By rolling monolayer of graphite sheet carbon nanotube (CNTs) can be prepared. CNTs have a 1D hollow tubular structure shown in Figure 10 which is further modified as single wall and multiwall CNTs. The CNTs electrical properties such as conductivity and chemical stability, can be accustomed by chemical doping and produce CNT/graphene hybrid films as well as CNT/polymer composites Wei et al. prepared PSCs using three types of with carbon which is multiwall CNTs, carbon black (CB) and graphite flakes. They fabricated device using spin-coating and drop casting techniques which provide great interface between the perovskite and different types of carbon material. However best results are produced by multiwall CNTs, due to two properties of CNT, they will not produce any crack in device assembly hence provide good electrical conductivity and continuous charge transfer happen between different layers of PSC. Hence achieve high fill factor of 0.75 and PCE of 10.30% with multiwall CNT device. The carbon black created PSC have inferior performance with the values of 0.65 and 9.35% respectively. [88, 95]

Carbon-based PSCs are most recent development in optoelectronic device fabrication techniques. Carbon is chemically stable, provide good electrical conductivity and its work function is very close to the Au [96]. The carbon electrodes are easy to deposit using low temperature printing deposition processes such as screen printing, doctor-blading, inkjet-printing, rolling transfer, press transferring, and dropcasting [97, 98].

Recent development in carbon-based PSC devices

Due to the inherent nonconductive characteristics of carbon particles (like graphite, carbon black), it is very difficult to prepare carbon paste from pure carbon particles. Hence, polymers have been added as a binder. To evade disbanding of the polymer binder with

perovskite solvent high temperature annealing has been performed. To get the optimized carbon paste and carbon paste based electrode, Hongwei Han's group demonstrated the impacts of thickness of carbon counter electrode and the size and shape of graphite particles, role of the binder, the properties of these carbon paste and fabricated layers has been are already explained in detail. [49, 62, 64, 81].There are many other modifications has been suggested by researchers to improve carbon layer, few recent developments on carbon related to PSCs has been listed below.

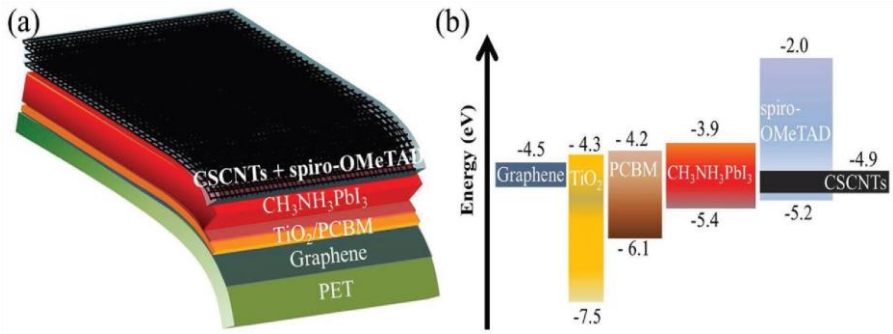

Figure 2.11: Device architecture (a) and energy band diagram

(b) of the all-carbon-electrode based flexible PSCs. [99]

Tiong et.al. [100] developed to perovskite films consisting octadecylamine functionalized single-walled carbon nanotubes (ODA-SWCNTs) With this film PCE of 16.1% has been attained and remarkable stability for 45 days with more than 60 % humidity has been obtained. This work successfully morphology manipulation of perovskite films which has been improved device stability using carbon material. [101] has been explored

an additive of acetonitrile (ACN) into carbon slurry, which has been efficiently enhanced the interface between carbon and perovskite [101].

All-carbon-electrode-based flexible PSCs have been developed by [99]. they manufactured device using graphene as transparent anode and carbon nanotubes as cathode. This flexible device has shown 11.9% PCE with spiroOMeTAD and 8.4 % without spiro-OMeTAD hole transport layer. These flexible all carbon PSC shown in Figure 11 have remarkable toughness against mechanical deformation in contrast with flexible PSC built on flexible ITO substrates. Furthermore, they have shown expressively greater stability under constant light illumination at 60 °C temperature, maintaining more than 90% of PCEs after 1000 h. The promising robustness and stability highlight that flexible PSCs are highly compatible with carbon materials and pave the way toward the realization of roll to roll fabrication of low-cost flexible PSC. [99]

Pie et.al. [97] demonstrated a highly-conductive, low-temperature annealable and perovskite-compatible carbon paste using additives of titanium (IV) isopropoxide and acetic acid. The functional additives in the carbon paste has been generated newly complex polymeric Ti-O-Ti species performing the role of binder as well as plasticizer. It enhances the electrical conductivity of carbon film increase to 1.13×10^4 S m−1, with 4 Ω $\square^{-1}$ sheet resistance for a 20 μm thick film, which is very higher than transparent FTO/ITO electrode (15 Ω $\square^{-1}$). Fully printable mesoscopic perovskite solar cells have been fabricated using this carbon film and obtain 14.04% PCE. The series resistance of the resultant device is 13 cm^2 which is quite lower than high temperature treated device (21 cm^2) This low-temperature, low cost, highlyconductive carbon film shows promising application in the future module design of fully printable mesoscopic perovskite solar cells. [97]

Hence Graphene and related materials (GRM) are promising aspirants to tune interface engineering of PSCs plays a pivotal role in achieving high PCE. Using this concept

Wang and et.al.[102] fabricated a mesoporous planner PSCs device with high stability and efficiency in using a carbon nanotube (CNT) bridging method. Here single-walled CNTs (SWCNTs) have been added in both perovskite and carbon layers to procedure superior perovskite layer and carbon layer interface. It has been shown that CNT bridge penetrated into perovskite and carbon electrode, results greater charge extraction and charge transfer ability, furthermore CNT bridge enhance electrical conductivity of the top carbon electrode hence grown a significant PCE of 15.73% by an outstanding stability of 90 days in the dark and under high-humidity [102].In another work, Najafi et.al.[103] fully exploit the potential of GRM, reduced graphene oxide (RGO) and molybdenum disulfide (MoS_2) has been used as both asa hole transport layerr (HTL) and active buffer layer (ABL) to control optoelectronic properties of PSCs. Because two-dimensional nature of RGO successfully plugs the pinholes of the MoS_2 Quantum Dots films. Hence PCE up to 20.12% (average PCE of 18.8%) has been achieved. However, these experiments have been performed in planner mesoporous architecture but the possibility to combine graphene and GRMs as interfacial layer in monolithic architecture have not been denied [103]. To improve interface graphene flakes has been added into the m-TiO_2 by Busby el.al.[104]. It has been shown that graphene addition into the m-TiO_2 enhance the stability of the PSCs by reducing the locally-inhomogeneous light-induced back-conversion of the $CH_3NH_3PbI_3$ layer into PbI_x and PbO_x species and resulting release of iodine species, which diffuse across the interfaces of the top electrode and trigger degradation[104]. In a recent work Chu et.al. [105] has been added GRM with Poly(3-hexylthiophene2,5-diyl) (P3HT) to fabricate HTL which has been well-matched with paintable carbon-electrodes. Space-charge-limited-current measurements disclose that the P3HT/graphene composite shows outstanding charge mobility and thermal tolerance and produced efficiency of 17.8%. The outstanding device stability is demonstrated by only 3% drop after storage in ambient conditions (humidity:

50%) for 1680 h (nonencapsulated), in comparison of their original output under continuous 1-Sun illumination at room-temperature for 600 h (encapsulated) in a nitrogen environment. [105]

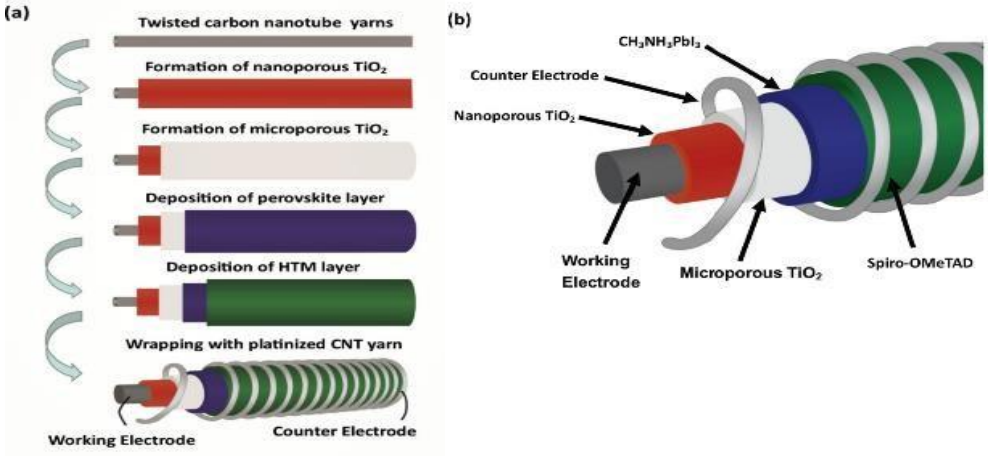

Figure 2.12: Schematic illustration of the dimensional CNT yarn based perovskite solar cell (a) fabrication process (b) structure. [106]

An all solid-state carbon nanotube yarn-based perovskite solar cell has been developed by Hussain et.al.. Three-dimensional perovskite solar cells based on CNT yarn exhibit high open current voltage. Carbon nanotube yarn based cells are flexible and capable of harvesting incident photons from any direction. [106] This three-dimensional all solid-state carbon yarn based PSC shows a promising prospect in portable and wearable textile electronics.

In another work by Ishikawa et.al. [107] Graphene layer has been manufactured on top of perovskite layer on a mesoporous planer PSCs using a thermal chemical vapor deposition (CVD) system. A multilayered graphene film has been built by H_2 and CH_4 gas.

This device has shown stability better than similar device. However, efficiency is poor but successful shown fabrication of good carbon layer on PSC by CVD.

Recent developments in mPSCs

Based on the coordination interaction of different components and the colloidal characteristic of precursor solution the crystal size and crystallinity of perovskite can be well controlled by additive adding Many additives have been added with perovskite precursor solution to improve mPSCs device. Firstly [6,6]-phenylC_{61}-butyric acid methyl ester (PCBM) has been introduced by Gaun et.al.[108]as an effective additive in the perovskite precursor solution. PCBM powders has been added to two types of perovskite $MAPbI_3$ and $MAPbI_{2.95}(BF_4)_{0.05}$ precursor solutions from a 0 to 1 mg / ml concentration. It has been found that 0.25 mg / ml PCBM is enough for PCE improvement. PCE of mPSCs. $MAPbI_3$ and $MAPbI_{2.95}(BF_4)_{0.05}$ precursors have given 8.58% and 12.77% PCE which has been improved to 12.36% and 14.26% after adding 0.25 mg / ml. It has been shown that PCBM additive improve perovskite morphology, stimulate charge separation and diminish charge recombination in the mPSCs device [108]. In another work Zou et.al. [109] combined carbon quantum dots (CQDs) in the perovskite precursor solution before infiltration It has been found that the little addition of CQDs to the perovskite solution can enhance the photocurrent density of mPSCs and produce around 7% PCE. [109]

Another bifunctional conjugated organic additive 4-(aminomethyl) benzoic acid hydroiodide (AB) is added with $MAPbI_3$ precursor, and results are Compared with the monofunctional cation benzylamine hydroiodide (BA) and the nonconjugated bifunctional organic molecule 5-ammonium valeric acid. Devices based on AB+$MAPbI_3$ show a good stability and a maximum PCE of 15.6%. The results are clearly compared in SEM images

of the film made with the precursor solution on glass substrate, clear grains of $MAPbI_3$ and $BA+MAPbI_3$ can be seen in figure (a and c) particles. However smaller compact grains are visible with $AB+MAPbI_3$ and AVA+MAPbI3. This pattern is continued during cross-sectional images of different layers with perovskite, $MAPbI_3$ and $BA+MAPbI_3$ did not penetrate fully TiO_2 and ZrO_2 particles can be observed from SEM on the other hand $AB+MAPbI_3$ and AVA+MAPbI3 showed a superior pore-filling. This is mainly due to ability of – COOH groups anchor a monolayer of AB or AVA to the surface of the mesoporous TiO_2 and ZrO_2 by coordinative binding to the exposed Ti(IV) or Zr(IV) ions, attaching the perovskites close to the metal oxides and serve as nucleation sites from perovskite growth.

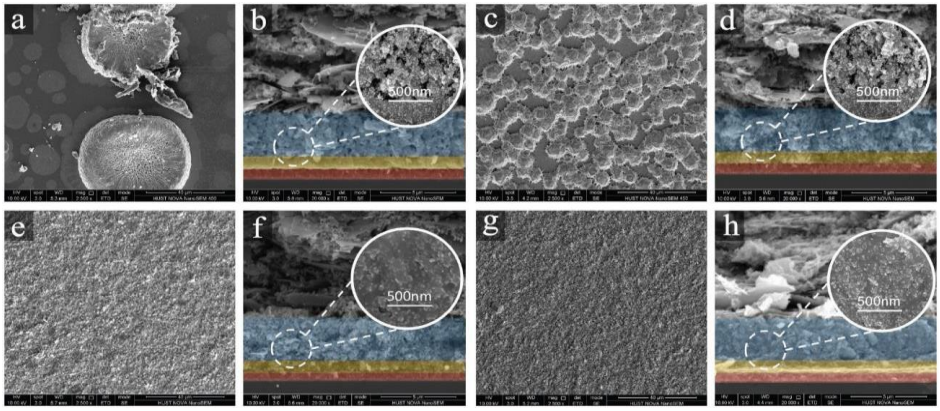

Figure 2.13: The top view scanning electron microscopy (SEM) images for a) $MAPbI_3$, c) BA- $MAPbI_3$, e) AVA-$MAPbI_3$, and g) AB-$MAPbI_3$ on 500 nm TiO_2/2 μm ZrO_2 and their cross-sectional SEM images of the cells filled with b) $MAPbI_3$, d) BA- $MAPbI_3$, f) AVA-$MAPbI_3$, and h) ABMAPbI$_3$. [110]

The bifunctional conjugated cation not only benefits the growth of perovskite crystals in the mesoporous network, but also facilitates the charge transport. This investigation helps explore new approaches to rational design of novel organic cations for perovskite materials.[110] By applying a molten-salt-based MAPbI3 precursor solution, dense filling

and improved perovskite crystallization inside the nano porous graphite based monolithic contact scaffold of the cell are achieved. A stabilized photovoltage as high as 1 V is achieved, representing the highest VOC reported for HTL-free $MAPbI_3$- based devices. [111]

Table 2.3: Recent developments in mPSCs

S. No.	$mTiO_2$	$mZrO_2$	m-C	Comment	PCE(%)	Year	Reference
1	600nm	2µm	12µm	$MAPbI_3$	8.58	2018	[108]
2	600nm	2µm	12µm	$MAPbI_3$ wih PCBM (0.25 mg /ml)	12.36	2018	[108]
3	600nm	2µm	12µm	MAPbI2.95(BF4)0.05	12.77	2018	[108]
4	600nm	2µm	12µm	$MAPbI_{2.95}(BF_4)_{0.05}$ with PCBM (0.25 mg /ml)	14.26	2018	[108]
5	NA	NA	NA	$MAPbI_3$ with 5 % carbon quantum dots (CQDs)	7	2018	[109]
6	500nm	2µm	15µm	$MAPbI_3$	6.47	2018	[110]
7	500nm	2µm	15µm	$MAPbI_3$ with benzylamine hydroiodide (BA)	12	2018	[110]
8	500nm	2µm	15µm	$MAPbI_3$ with 5-aminovaleric acid hydroiodide (AVA)	14.1	2018	[110]
9	500nm	2µm	15µm	$MAPbI_3$ with 4-(aminomethyl) benzoic acid hydroiodide (AB)	15.6	2018	[110]
10	700nm	1.6 µm	9 µm	molten-salt-based $MAPbI_3$ precursor solution	12.6	2018	[111]
11	500nm	3µm	10µm	room-temperature liquid metals added with carbon paste	13.51	2018	[112]
12	600nm-NR18	-	10µm	Cs0.1FA0.9PbI3	9.35	2019	[113]
13	600nm-NR30	-	10µm	Cs0.1FA0.9PbI3	13.92	2019	[113]
14	600nm-NR30	1.2µm	10µm	Cs0.1FA0.9PbI3	8.02	2019	[113]
15	600nm-NR30	2µm	10µm	Cs0.1FA0.9PbI3	14.38	2019	[113]
16	600nm-NR30	3µm	10µm	Cs0.1FA0.9PbI3	12.74	2019	[113]
17	500nm	2 µm	10µm	ZTO-3 (20 nm) and ZTO-1 (50 nm) printed between FTO and $mTiO_2$	15.86	2019	[114]

Thick carbon layer in the mPSCs working as hole transport layer as well as counter electrode which often lead to inefficient hole extraction. Hence liquid metal (LM) as an interface modifier material is combined with carbon paste to build carbon electrode. LMs can significantly increase the conductivity of the carbon electrode and optimize the contact property between carbon and perovskite result 13.51 efficiency. [112]

Zong et.al. [115] added Ammonium chloride (NH_4Cl) in different concentration in perovskite precursor solution to demonstrate stability improvement of PSCs by using simple solution-process. Under ambient air and no encapsulation conditions this device exhibited more than 576 hours of stability and able to maintain 96% of the initial PCE.[115]

Hou et.al. [113] applied formamidinium lead triiodide ($Cs_{0.1}FA_{0.9}PbI_3$) as the light synthesizer. In this work high-quality α- $Cs_{0.1}FA_{0.9}PbI_3$ phase inside the mesoporous scaffold has been built using a mixed solvent of DMF and DMSO, and further adding CsI in the precursor solution. Vapor assisted crystallization approach has been produced 15% of PCE with a spectral response up to 840 nm. The phase transition and crystal growth of $Cs_{0.1}FAPbI_3$ are carefully monitored in the mesoporous scaffold. This work not only opens up new methods for fabricating efficient and stable solar cells but also provides a deeper understanding of crystal growth inside constrained nanostructures.[113].

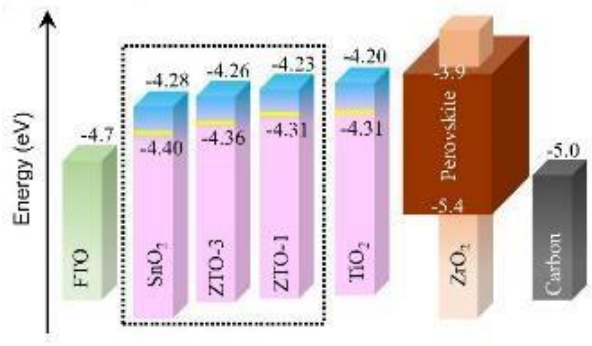

Figure 2.14: Possible band alignment of perovskite solar cell based on different Electron Transport Layer according to their fermi levels, conduction bands and bandgaps. [114]

For improving mPSCs device gradient bilayered zinc tin oxide (ZTO) has been introduced as electron transport layer (ETL) by Zhao et.al. The ZTO films has been prepared by mixing Di-n-butyltin bis(2,4-pentanedionate) ($C_{18}H_{32}O_4Sn$) and zinc acetate dihydrate ($Zn(CH_3COO)_2 \cdot 2H_2O$) in different weight percentage in methanol solvent and printed using spray pyrolysis annealing is performed at 400℃ to stabilize layer

Rest $mTio_2$/$mZrO_2$/mCarbon layers have been printed with conventional protocol. The use of ETL suppress energy loss and supplements the V_{oc}, which is due to suitable matching of cascade level between perovskite and the ZTO ETL. Gradient energy level has been achieved by using different carrier concentrations of Zn in ZTO films. The champion device produces a high V_{oc} of 1.02 V and PCE of 15.86%. and long-term stability with $(5\text{-AVA})_x(MA)_{1-x}PbI_3$ perovskite precursor. These findings provide a simple pathway to design the interface between ETL and perovskite, and to tailor the band alignment to suppress interfacial trap-assisted recombination of mPSCs for enhancing V_{oc} and charge extraction simultaneously. [114]

Future trend in monolithic

mPSCs fabricated in ambient conditions by using inkjet infiltration of perovskite precursor ink. The inkjet infiltration technique demonstrates remarkable performance reproducibility. Hence open new path for batch printing [70]. But the use of this technique is mainly limited by quick conversion of perovskite liquid precursors to perovskite crystals, hence the nozzles of the printer cartridges experience blockage very rapidly and stop working for specific materials deposition. However this problem is quite solved with the introduction of 5-AVAI in the precursor solution, which significantly slows down the perovskite crystal growth before and after the deposition of the precursor ink. $(5\text{-AVA})_x(MA)_{1-x}PbI_3$ precursor prevent the inkjet printer cartridge from clogging and

provides an opportunity for precise patterning and controlled volume dispensing of precursor ink. The capabilities of the other additives in $MAPbI_3$ such as carbon quantum dots (CQDs) [47], 4-(aminomethyl) benzoic acid hydroiodide (AB)[110], molten-salt [111], must be explored through inkjet printer.

Furthermore, perovskite precursor such as formamidinium lead triiodide ($Cs_{0.1}FA_{0.9}PbI_3$) [113] Methyl ammonium lead bromide ($MAPbBr_3$) [116] which has produced good results in small scale must be tested for larger scale printing with inkjet perovskite infiltration.

The mesoporous layer and the properties of the precursor solution would critically determine the perovskite filling fraction and its quality. For improving perovskite precursor filling parameter precursor which is used by other researchers in PSC must be infiltrated in monolithic architecture as well. Highly stable planner perovskite solar cells (PSCs) have been prepared under 30% humidity, where $CH_3NH_3Pb(I_{1-x}Br_x)_3$ perovskite was used as the absorber. With appropriate Br doping PCE around 10% with active area of 0.2 cm^2 under 1sun radiation has been achieved with almost no change in efficiency for 56 days [117]. To make perovskite crystal water resistant 2-Aminoethanethiol (2-AET) ligand has been introduced in the preparation of MAPbI3 perovskite. film. With this perovskite crystal structure can retain for 10 minutes in water. due to the formation of water-resistant MAPbI3 $(x)_2$AET perovskite [118]. The 2D Ruddlesden-Popper perovskites attracted increasing research attention in recent years. The general formula of the 2D perovskite is $(RNH_3)A_{n-1}B_nX_{3n+1}$) where R is an aromatic group or long-chain alkyl have shown great stability as compared to 3D perovskites..[119]. Another demonstrated perovskite is a chlorine-containing methylammonium lead iodide precursor formulation along with solvent tuning to enable a wide precursor-processing window (up to 8 min) and a rapid grain growth rate

(as short as 1 min)[120]. All the above stated perovskites should be further explored for mPSCs architecture. Because they have all potential to being commercialized [52].

Despite of material improvement developing a fabrication method that is less sensitive to the fabrication environment is also very necessary. In all the above fabricated mPSCs carbon film annealing has been performed at 400°C .But now it has been shown that this much temperature may produce high efficiency mPSCs but it had a negative impact on quality of carbon film [121]. To enhance term stability of mPSCs hydrophobic additives with the combination of different annealing temperature must be tested. New packaging technique that does not crosslink with perovskite must be introduced.

The large-scale solar cell modules can be improved by developing fullerene and graphene derivatives which improve the conductivity and match the energy alignment between perovskite and electrode Furthermore, reducing series resistance must be kept minimum by using FTO substrates with higher conductivities and without sacrificing optical transmittance. The carbon counter electrode with smaller resistance needs to be developed as well, by modifying the combination of the conducting graphite and the catalyzing carbon black powders. The active area of the module should be enlarged, while at the same time, the mismatch loss and internal resistance should be reduced, by careful optimization of the module design.

Conclusion

In this review, we have focused on the recent progresses and advances of the low-cost HTM-free mPSCs with respect to the perovskite modification, optimization of functional layers (carbon layer, ETL and spacer layer), perovskite deposition technology and post-treatment, and then larger-area PSMs. Particularly, (5AVA)x(MA)1_xPbI3 based HTM-free CPSCs exhibit high stability under continuous illumination and outdoor

condition, making it among the most promising solar cells for commercialization. However, the current PCE of HTM-free mPSCs is still lower than that of conventional HTM-based PSCs. Therefore, improving the PCE of the device has become the priority.

Chapter 3: Experimental Materials and Methods

Introduction

The first chapters explained impotence of photovoltaics in the current scenario, its general operation and limitations with currently commercially available silicon solar cells. Second chapter explain state of the art carbon-based hole transport material free Monolithic Perovskite Solar Cell (mPSCs) and challenges during fabrication of mPSCs. The current chapter summarizes all the materials, characterization tools and general fabrication methods.

Materials

Indium Tin Oxide (ITO)

Optically transparent, electrically conductive and thin pinhole free compact printability make ITO very useful for photovoltaic applications [122]. For our work fully oxidized ITO coated on the glass substrate with sheet resistance $16\Omega\square^{-1}$ has been purchased from Ossila.

Titanium Dioxide (TiO_2)

The compact TiO2 layer is very important to enhance efficiency of PSCs because it avoids direct connection between the perovskite and ITO, which is very necessary to prevent charge recombination and reduce series resistance of the device. [123] Ti-Nanoxide BL150/SP paste from Solaronix has been used for fabrication of compact layer.

The importance and requirement of mesoporous TiO_2 ($mTiO_2$) have been explained in detail during the last chapter. Ti-Nanoxide T165/SP nanoparticle paste from Solaronix has been used for $mTiO_2$ printing.

Zirconium Dioxide (ZrO_2)

Zr-Nanoxide ZT/SP nanoparticle paste from Solaronix has been used for printing insulating layers in mPSCs.

Carbon

Elcocarb B/SP paste brought from Solaronix has been used for mesoporous carbon (mCarbon) layer printing. This paste consists of graphite and carbon-black nanoparticles of size 1–20 µm.

Perovskite Precursor

The perovskite precursor solution was made by lead iodide (PbI_2) brought from TCI, methylammonium iodide (MAI) and 5-aminovaleric acid hydroiodide (5AVAI) purchased from Greatcell. Solvent γ-butylactone (GBT) supplied by Sigma Aldrich.

Fabrication Techniques.

Substrate cleaning

Glass substrates cut into pieces of 80 × 15 mm using a glass cutter. They were cleaned sequentially in an ultrasonic bath with acetone (VWR Prolab chemicals), methanol (VWR Prolab chemicals) and DI water (obtained from a custom in-house system) with the addition of 1% Hellmanex-II Ossila) for 10 mins. Subsequently substrates were rinsed with plenty of deionized water after each cycle and lastly dried under a blow drier. The substrates were stored under vacuum to maintain their surface clean.

c-TiO_2 printing

Ti-Nanoxide BL150/SP paste is intended for screen-printing fabrication and printed using 150 polyester mesh screen, resulted thin, dense, and pinhole-free compact layer after annealing at 500°C for 30 minutes.

m-TiO_2 printing

Screen-printing has been performed with Ti-Nanoxide T165/SP past a 165 polyester mesh stencil and after annealing at 500°C for 30 min, an 800nm to 1µm thick layer has been printed.

m-ZrO_2 printing

After annealing at 500°C for 30 minutes 1.5 - 2µm thick layer of zirconia has been printed. Screen printing method with 90 polyester mesh has been used for printing.

m-Carbon printing

A screen made from nylon mono filament fabric with 130 mesh count per inch was used for printing After annealing at 400°C for 30 minutes it will give 10 - 12µm thick layer of carbon.

Perovskite precursor solution preparation

The perovskite precursor solution was made by dissolving 0.55g PbI_2, 0.19g MAI and 0.015 g 5-AVAI in 1 ml GBT in a glass vial. A clear yellow solution was obtained after stirring them for 2 hours at 70 °C for with magnetic beat. Perovskite precursor solution

allowed to cool down to room temperature and filtered through a PTFE filter before infiltration to mPSCs.

Characterization Techniques

Electrical Characterization

Sheet Resistance Measurement

Sheet resistance measurement techniques (Ossila's Four-Point Probe) is used to study electrical properties. A four-point probe is a simple device for measuring the resistivity of thin films. By passing a current through two outer probes and measuring the voltage through the inner probes allows the measurement of the substrate resistivity.

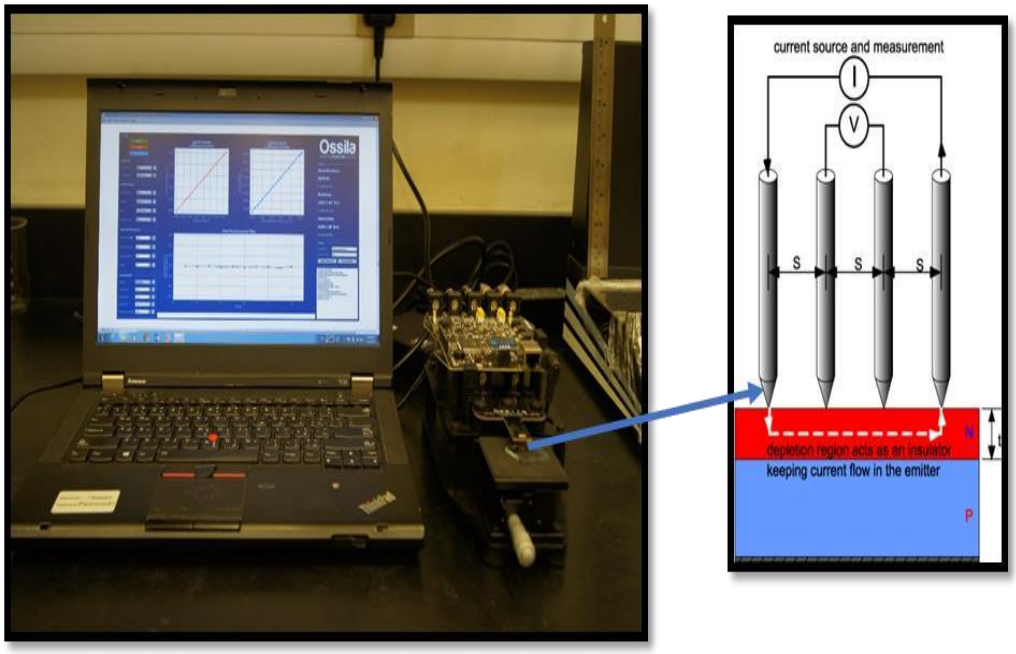

Figure 3.1: Ossila 4-point probe system for sheet resistance measurement.

Morphological characterization

Scanning electron microscopy (SEM) and Energy-dispersive X-ray spectroscopy (EDS) analysis

The surface morphology of the samples was investigated using Nova Nano Scanning Electron Microscopy with Bruker EDX Detector. SEM creates images by focusing a high energy electron beam onto the surface of samples and produce high resolution images, which help in understanding the surface morphology.

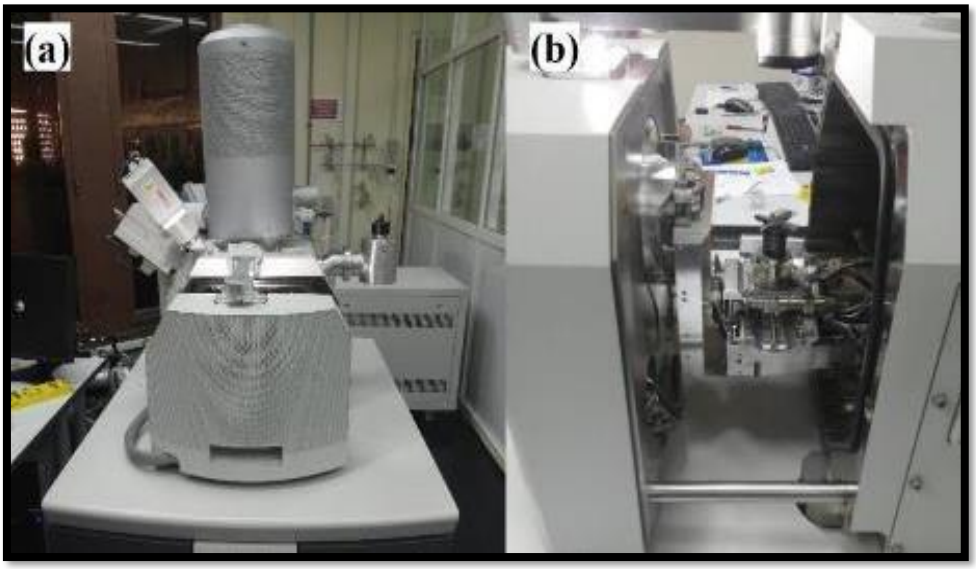

Figure 3.2: Nova Nano Scanning Electron Microscopy with Bruker EDX Detector

In conjunction with an X-ray Energy Dispersive Spectroscopy device (EDAXEDS), qualitative and semi-quantitative elemental analysis can be done on the sample under investigation SEM is used for the surface morphology study of a wide range of specimens, with use in biological, biomedical and material sciences. It has the ability to magnify typically to 200,000 times.

Atomic force microscopy (AFM)

Atomic Force Microscopy (AFM) from Asylum Research is a unique heavy duty tribometer used to measure 3D images of the studied surface. Floor standing with easy to interchange various modules, close loop down force control makes this tribometer a power tool for determination of friction coefficients on traditional industries such as coating, oil, lubricant etc.

Figure 3.3: Atomic Force Microscopy (AFM)

Transmission electron microscopy (TEM)

Transmission Electron Microscope (TEM) model TECNAI G2 TEM, TF20 by Field Electron and Ion Company, (FEI) has been used for our sample analysis. The ultra-high magnifications of TEM have made it a very powerful tool for material science. A high energy electron beam has been excelled through sample, further interactions between the electrons form TEM machine and the sample atoms can be observe and produce information regarding crystal structure and grain boundaries. High resolution can be used to analyze the quality, shape, size and density of quantum wells, wires and dots. However,

sometimes high energy beam damage samples as well. TEMs can reveal the finest details of internal structure as small as a few angstrom units (10^{-10}m).

Figure 3.4: Transmission Electron Microscope (TEM)

Thermal Characterization

Thermogravimetric analysis (TGA)

Temperature dependent characteristics are examined by thermogravimetric analysis (TGA) Perkin Elmer TGA 4000 Analyzer under a nitrogen environment. During the measurement a sample has been heated in TGA equipment and releases volatile materials. The 900°C temperature can be attained by the TGA. TGA measurement can be used to identify the structure for many organic and inorganic compounds, Identify impurity, combustion properties and loss of water in a material by weight percentage.

Differential scanning calorimetry (DSC)

Temperature dependent characteristics have been examined by differential scanning calorimetry (DSC) Perkin Elmer DSC 8500 instrument under a nitrogen environment. The differential scanning calorimetry is a fundamental tool in thermal analysis. It looks at how a material's heat capacity is changed by temperature. A sample of known mass is heated or cooled and the changes in its heat capacity are tracked as changes in the heat flow. The information these instruments generate is used to understand amorphous and crystalline behavior, polymorph and eutectic transitions, curing and degree of cure, and many other material properties used to design, manufacture and test products.

Figure 3.5: (a) Differential scanning calorimetry (DSC). (b) Thermogravimetric analysis (TGA)

Spectroscopic Analysis

Raman spectroscopy

The Raman spectra were obtained by a Raman spectroscopy, Jobin-Yvon HR800 UV-Vis-NIR Raman spectrometer equipped with an Olympus BX 40 attachment. The excitation wavelength was 514.5 nm with an energy setting of 1.2 mV from a coherent Innova model

308 argon-ion laser. The Raman spectra were collected by means of back scattering geometry with an acquisition time of 50 seconds.

Fourier-transform infrared spectroscopy (FTIR)

Fourier transform infrared spectroscopy (Spectrum 2000, Perkin Elmer), spectra were recorded with a resolution of 2 cm−1 over the wave number range 4000~400 cm−1.FTIR Spectrophotometer 760 Nicolet and 670 Thermo Nicolet: determine compounds based on the absorbance in the Mid-IR (4000-400 cm-1) and Far-IR 600-5 cm-1. FTIR spectrophotometer can identify the functional groups (alcohol, carbonyl, carboxyl, ester, ether, cyanide...etc). This instrument can analyze samples as solid, liquid or gaseous. Thus, this instrument is useful for the analysis of petroleum products, drugs, paints, detergents, oils, fibers and polymers. Electronic libraries equipped with the Nicolet instruments allow fast identification via matching the obtained results with the one available in the library.

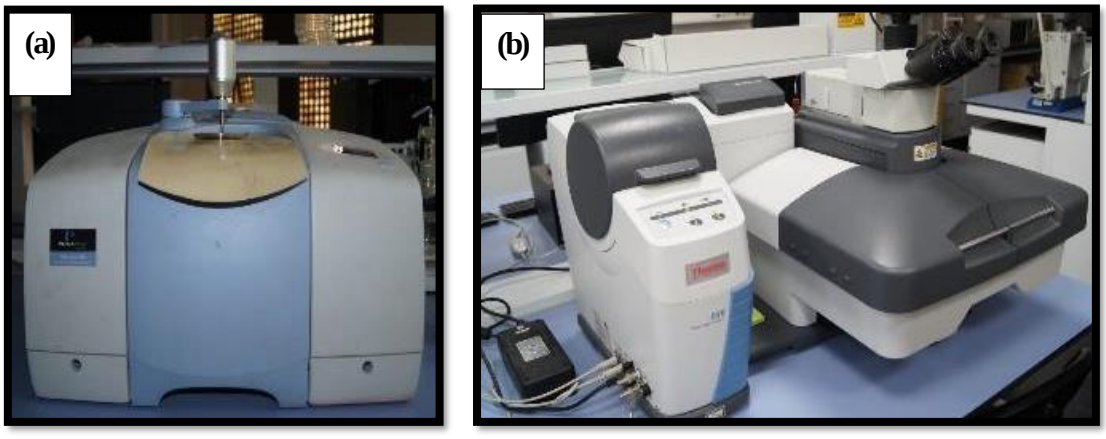

Figure 3.6: (a) Fourier-transform infrared spectroscopy (FTIR) and (b) Raman spectroscopy

Electrochemical Impedance Spectroscopy (EIS)

Electrochemical Impedance spectroscopy is a powerful method for characterizing the electrical properties of solar cells. Analysis of EIS spectrum of a mPSCs provides information about several important charge transport, charge transfer, and hole/electron accumulation processes in mPSCs. For our experiment Gamry 3000 potentiostat has been used.

Quantitative Analysis

X-ray powder diffraction (XRD) analysis

Figure 3.7: X-ray powder diffraction (XRD)

X-ray diffraction (XRD) patterns was documented with an EMPYREAN Advanced diffractometer operated at 45 kV and 40 mA with K-Alpha1 radiation of wavelength

1.540598Å and K-Alpha2 radiation of wavelength 1.544426Å with scan speed of 1 s/step and a step size of 0.013° 2θ.

X-ray photoelectron spectroscopy (XPS) analysis

X-ray photoelectron spectroscopy (XPS) has been used to perform quantitative elemental composition analysis of the samples. XPS is a useful measurement technique because it shows all the elements bonded in the sample. However, it can be used only for surface analysis because the instrument will only probe 20 nm into a sample.

I-V characterization

mPSCs I-V Characteristics Curves have been recorded using Abet Sunlite Solar Simulator, with Keithley 2400 SMU using Kickstart software program. I-V curves are basically a graphical representation of the operation of a solar cell. I-V curves provide the information essential to configure a solar system to operate its maximum power point (MPP).

Chapter 4: Characterization of Printable Carbon Electrodes for Monolithic Perovskite Solar Cells.

Introduction

Top carbon electrode has been printed using carbon paste, often, by carbon black and graphite powder and a binder (pasting liquid). Graphite is soft, soapy, hexagonal layered crystal having properties such as temperature resistance, excellent electrical and thermal conductivity, corrosion and thermal shock free [88, 89]. Polymer binders are used to provide lubrication between graphite and carbon black particles All the above stated characteristics the graphite reflects device performance when built as electrodes. Carbon paste-based electrodes are highly repeatable with different dimensions, hence very important characteristics for large area solar module fabrication [91, 92]. However, during our experimentation for the fabrication of mPSCs, it has been observed that the carbon films start to peel off and carbon dust has been coming out of the glass and ITO substrates after heating at 400 °C Hence, fabrication of carbon films by screen printing method and their characterization has been explored. In this chapter impact of annealing temperature on the electrical and morphological properties of the screen-printed carbon film has been examined.

Experimental Procedure

Carbon paste (Elcocarb B/SP, purchased from Solaronix) was used for the deposition of conductive carbon films by screen printing shown in Figure 1. Glass substrates cut into pieces of 80 × 15 mm. They were cleaned with cleaning protocol explained in chapter 3. A screen from nylon mono filament fabric with 130 mesh count per inch have been prepared for printing. The carbon paste was printed on glass and ITO substrate using a hard squeegee with an angle of 45° for three times. Each substrate is printed with four 5 × 5 mm carbon

electrodes. Then the different substrate was annealed on hot pate for 30 min ranging from 100°C to 400°C.All the experimental procedure have been performed on ambient conditions.

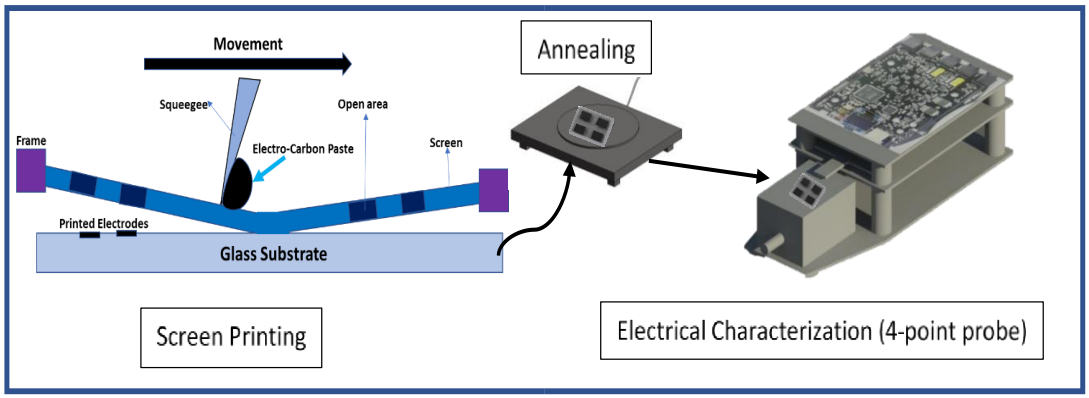

Figure 4.1: Schematic and graphical illustration of the screen-printing, annealing and electrical characterization using 4-point probe procedure for the carbon films.

Electrical Characterization

The effect of annealing temperature on the electrical conductivity of the carbon films has been measured by 4-point probe sheet resistance measurement system provided by Ossila. The carbon film annealed at 100°C produced 6.875 KΩ /□ sheet resistance of the glass substrate and it reduced exponentially with the increase in temperature. Heating carbon film above 300°C drastically decreases carbon sheet resistance to 171.5 Ω /□ but further increase in the annealing temperature (above 300°C) deforms carbon films (as shown in the inset of Figure 2). Annealing leads to greater inter particle contact, allowing easier charge transfer across the film and reducing carbon film sheet resistance [124].

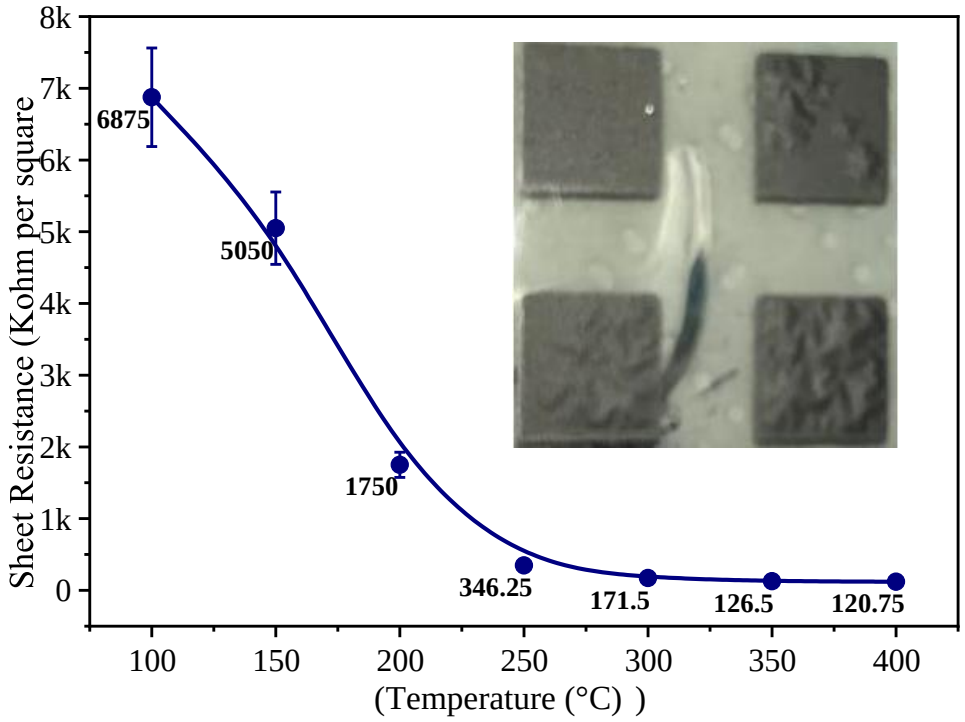

Figure.4.2: Sheet resistance of carbon film annealed at different temperatures.

Insets show deformation of carbon film annealed at 400°C

Thermal Characterization

Thermogravimetric analysis (TGA)

The sample annealed at 100°C and 200°C showed two major weight loss steps as shown in the derivative TGA plots given in Figure 4.3 (a). First weight loss step started around 130°C might be related to vaporization of the solvent or moisture, which remains even after the annealing process. Whereas the second weight loss step started around 225 °C. The reason of this weight loss might be related to decomposition of the binders present in the electro carbon paste. However, this mass change is not present in the samples annealed at higher temperatures (300°C- 400°C) over the entire range of temperature. This indicates that the weight loss of the films has already been done during the annealing process. In fact, various parameters, such as functional groups, packing density, presence of catalyst particles and graphitic structures could affect the TGA curve. Each of the above

mentioned parameters change the physical properties of the carbon films during annealing process [125].

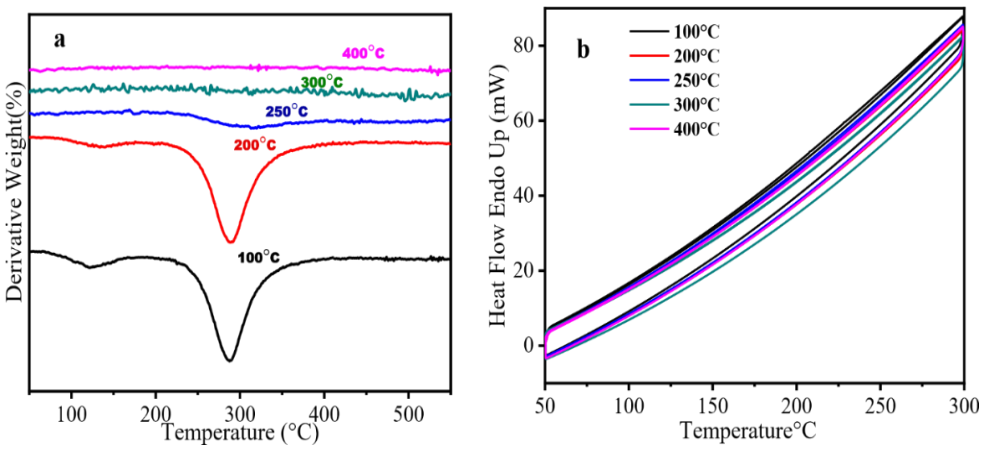

Figure 4.3: (a) Derivative thermogravimetric analysis (50-550 °C) of carbon films annealed at different temperatures.
(b) DSC thermal curves of heat flow versus temperature.

Differential Scanning Calorimetry (DSC)

DSC was also conducted to understand the sample's stability and exothermic phenomenon of thermal decomposition reaction shown in Figure 4.3 (b) in the carbon film during the annealing process. However, no peaks were observed on DSC curves in the 50°C - 300°C measurement range. This indicates that the crystallization temperature of the samples is higher than 300°C. However, performing DSC over 300°C is not required for carbon thin films because the electrodes deform at higher temperatures as mentioned above.

Morphological characterization

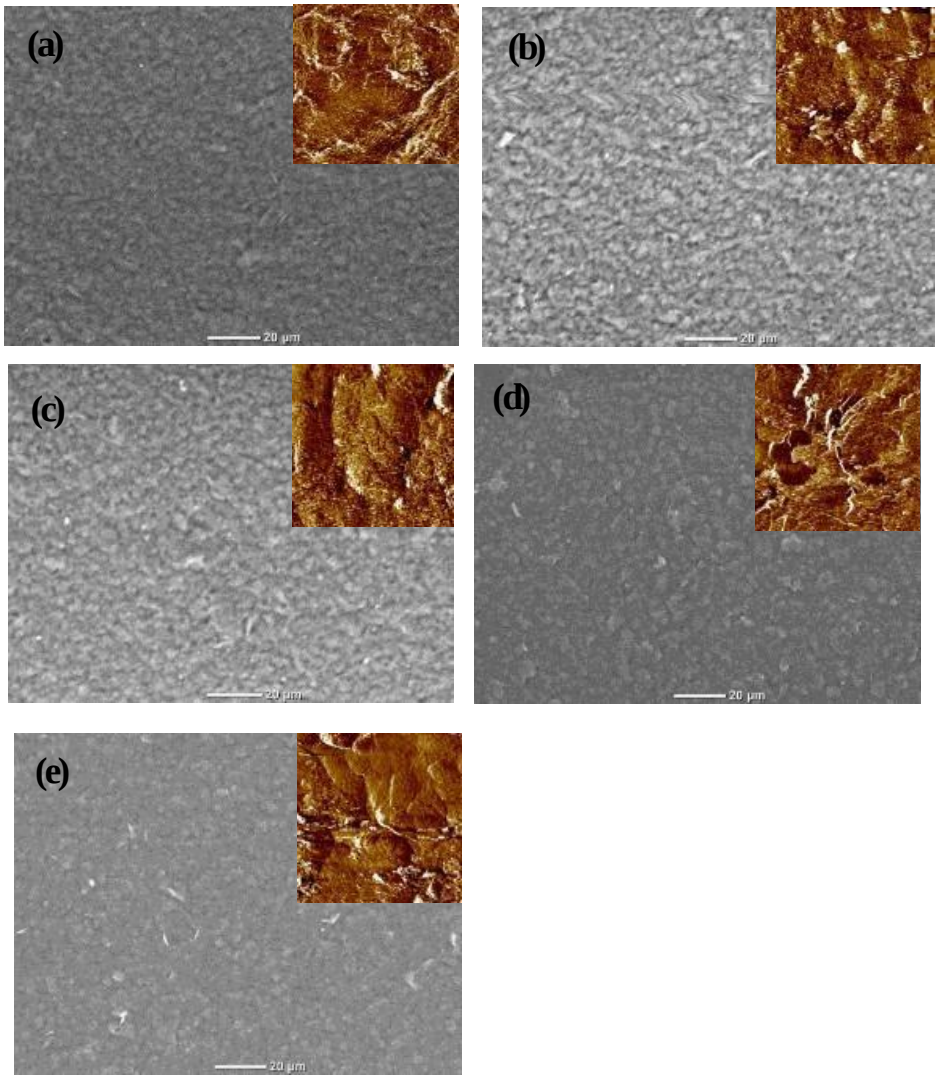

Figure 4.4: SEM and AFM (insets) images of the annealed carbon films: (a) at 100°C, (b) at 200°C, (c) at 250°C and (d) at 300°C (e) at 400°C.

Scanning Electron Microscopy (SEM)

Figure 4.4 shows the SEM images of the annealed carbon films in the temperature range 100°C to 400°C. SEM images show the dense, uniform and defect free carbon coating having an irregular particle morphology. The distribution of the graphite particles on the

surface of the films can be clearly seen. There is no significant change in the surface morphology has been observed in this annealing temperature range. However, a close look at the SEM images show that the sample annealed at 300°C and 400°C exhibit a very clear and distinguished distribution of the graphite particles as compared to the others SEM images taken from lower annealing temperature. The surface roughness also seems to increase with the increase in the annealing temperature.

Atomic Force Microscopy (AFM)

To validate the SEM results and to find the surface roughness of the films, the AFM images were also recorded. The surface roughness taken from AFM images (shown in the insets of SEM) are given in Table 4.1. This confirms that the surface roughness increases with the increase in the annealing temperature, which might be due to decomposition of the binders present in the electro carbon paste.

Table 4.1: RMS roughness of the carbon films annealed at different temperature.

S.No.	Annealing Temperature (°C)	RMS roughness (nm)
1	100	39.6
2	200	47.6
3	250	53.9
4	300	64.4
5	400	65.6

Spectroscopic Analysis

Raman spectroscopy

Raman spectroscopy is used to identify the dissimilarity of carbon films annealed at different temperature. The Raman spectra for carbon film is presented in Figure 4.5 show the existence of the D, G and 2D bands. The peak positions and their intensities have been given in Table 4.2. The presence of disorder in the graphitic lattice is associated with the occurrence of D band (at 1333 cm^{-1}). The G band is located around 1581 cm^{-1} is a common feature in all graphene and carbon graphitic materials and corresponds to the zone-center vibration of carbon atoms in the layer planes [15]. A broad second order 2D band at 2690 cm^{-1} present the first overtones of the D band. The intensity ratio of D band to G band (I_D/I_G) is used to measure of the quality of graphitization or defective disorders in the crystalline graphite. The highest value of the Raman.

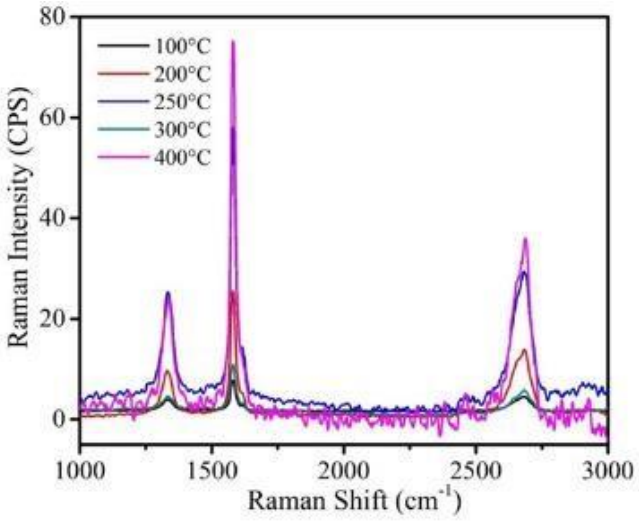

Figure 4.5: Raman spectra of annealed carbon films (100°C - 400°C).

Table 4.2: Band peaks, intensities and ratios (I_D/I_G and I_{2D}/I_G).

Annealing Temperature (°C)	D-Band Peak, cm^{-1}	D-Band Intensity, cps	G-Band Peak, cm^{-1}	G-Band Intensity, cps	2D-Band Peak, cm^{-1}	2D-Band Intensity, cps	*ID/IG*	*I2D/IG*
100	1333	65.4	1580.93	127.8	2686	73.7	0.52	0.57
200	1333	61.8	1580.65	163.7	2682	88.9	0.38	0.54
250	1334	63.8	1581.42	146.2	2682	73.9	0.43	0.50
300	1335	30.6	1580.73	73.1	2682	39.4	0.42	0.53
400	1336	18.3	1581.32	56.6	2687	27.1	0.32	0.47

Ratio (I_D/I_G) is obtained from carbon annealed at 100°C confirms the low graphitization degree of carbon film. The (I_D/I_G) value is obtained minimum for 400°C, which shows reduced defect region in graphite. The intensity ratio 2D band to G band (I_{2D}/I_G) shows that initially carbon is multilayer. However, decreasing 2D peak intensity, with increasing annealing temperature is an indicative of decreasing of the number of graphene layers in samples [126, 127].

Fourier-transform infrared spectroscopy (FTIR)

FTIR spectra of the carbon films is given in Figure 4.6. The relative increase of bands around 900-1300 cm^{-1} region points out the increase in the amounts of hydrated surface oxides (O-H deformation and C-O stretching). An absorption peak occurs at 1270 cm^{-1} band shows C=C stretching. However, these peaks are observed for the samples annealed at 300°C and above which is obvious because partial oxidation of the carbon happens at higher temperature only.

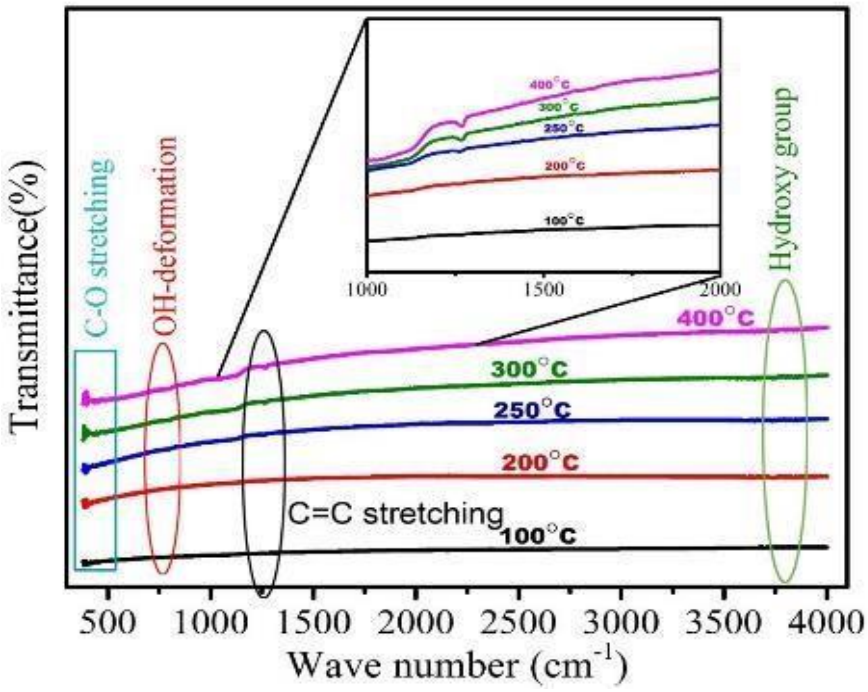

Figure 4.6: FTIR spectra of carbon annealed at different temperature.

The absorption peaks in the range of 3600-3900 cm^{-1} correspond to hydroxyl groups, indicating existence -OH on the surface of the carbon or it can be produced due to the adsorption of some atmospheric water during FTIR measurements. Those at below 500 cm^{-1} are the C-O stretching mode of the functional groups on the surface of the carbon [128-130].

The X-ray diffraction (XRD)

The X-ray diffraction (XRD) patterns of the carbon film is presented in Figure 4.7. The XRD plot shows the existence of a peak at 2θ ~26.5° for pristine graphite this represents the (002) plane with an interlayer spacing of 0.34 nm. The peak at 2θ ~ 54.6° indicates the existence of (004) plane with interlayer spacing of 0.16 nm [131]. The (002) and (004) reflections in the diffraction patterns are asymmetric, they can be considered as a

superposition of two components corresponding to the structural phases of graphite with different inter-planar spacings. This diffraction peak that corresponds to graphite plane is not very sharp which indicated that the graphite particles are not very well-ordered.

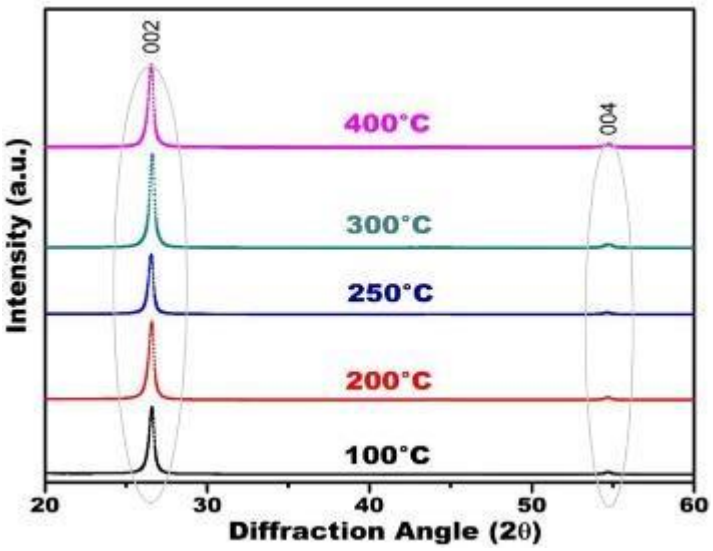

Figure 4.7: XRD patterns of carbon films annealed at different temperatures.

Conclusion

The electrical, structural and morphological properties of the carbon film have been investigated in the annealing temperature range 100°C - 400°C. The results show that best electrical characteristics are obtained for 250°C-300°C and further heating deforms and peels off the carbon film from substrates. Raman and XRD results show that electro-carbon quality improved with the increase of temperature. However, no significant change in the surface morphology of the films has been observed.

Chapter 5: Electrochemical Impedance Spectroscopy (EIS) of Monolithic Perovskite Solar Cells

Introduction

There is a need to correlate all the physical properties/processes taking place in the mPSCs to gain a deeper understanding of mPSCs operation: What is the role of the contacts? What limits the efficiency of existing perovskite solar cells? How many charge carriers are there in the cell under operating condition. Hence in Chapter 5, Electrochemical Impedance spectroscopy (EIS) spectrum is explained, which is performed on the mPSCs having highest efficiency during previous experiments. The EIS spectrum of mPSCs quantitatively explain the role of contacts, layers, charge generation, drift and diffusion of charge carriers and recombination. Which further provides insight into performance-limiting physical processes of mPSCs.

Experimental Procedure

Photocurrent and voltage were measured by Abet technology Sun light solar simulator equipped with a 450 W Xenon lamp and a Keithley 2400 source meter under one sun illumination (100mW/cm^2) using Kickstart software. The electrochemical impedance measurements have been performed with Gamry-3000 potentiostat. A sinusoidal AC potential perturbation of 10 mV has been overlaid over the applied DC bias potential. The 0.01 Hz to 1 MHz frequency range applied for the DC bias potential of zero, 300 and 500mV. During the measurements the devices has been kept in a dark faradaic cage to ensure isolation. The resultant impedance spectra have been fitted with Gamry Echem Analyst software.

J-V characteristics for mPSCs annealed at different temperature

To investigate the effect on the sintering temperature of the Elocarb conductive carbon paste explained in chapter 4 in actual solar cells, devices with an HTM-free mesoscopic architecture was fabricated. The fully printable substrates provided by Solaronix are made from a stack of FTO/c-TiO_2/m-TiO_2/m-ZrO_2/Elocarb carbon. The perovskite is introduced at a later stage by drop-casting the perovskite precursor solution onto the printed substrates to infiltrate the mesoporous structure and form a dense perovskite layer in the mesoporous scaffold after a slow annealing procedure.

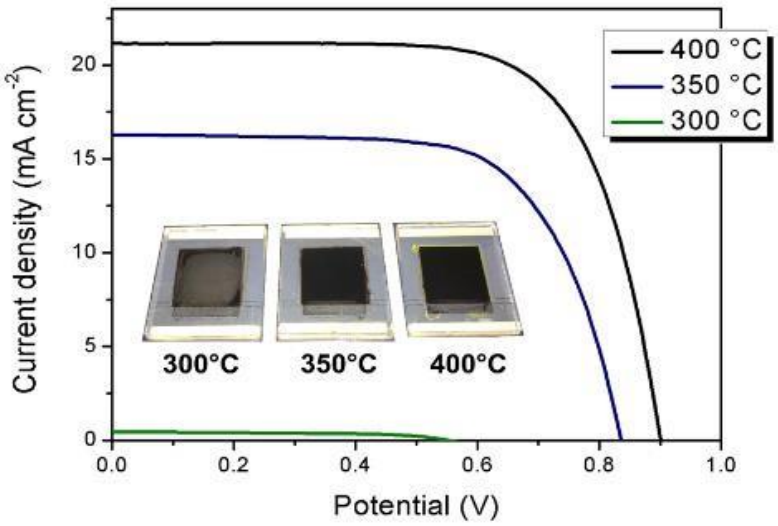

Figure 5.1: JV-curves of the corresponding champion devices fabricated from HTM-free printed mesoscopic substrates annealed at 300°C, 350°C and 400°C prior to the infiltration of the perovskite precursor solution.

The printed substrates were produced and stored in ambient atmosphere and fired at different temperatures prior to infiltration of the perovskite precursor solution.

The substrates are heated for 30 minutes at the desired temperature and afterwards cooled down to room temperature. Infiltration of the perovskite precursor solution as well as annealing of the devices was performed as described elsewhere [72].

Table 5.1: Summary of photovoltaic parameters from solar cells fabricated using printed substrates annealed at different temperatures. Values in bold are obtained from the corresponding champion devices; average values are shown in brackets.

Annealing temperature	*Voc* (mV)	*Jsc* (mA cm^{-2})	*FF* (%)	*PCE* (%)
300 °C	554 (546)	0.55 (0.54)	57.3 (54.5)	0.14 (0.13)
350 °C	836 (824)	16.3 (15.5)	67.7 (65.4)	9.2 (8.4)
400 °C	900 (885)	21.4 (20.4)	69.1 (66.8)	13.3 (12.4)

Figure 5.1 shows the J-V curves of the champion devices using different annealing temperatures of the substrates, and the corresponding photovoltaic parameters are summarized in Table 5.1. A sintering temperature of 400°C showed the highest device efficiency of over 13 %. Using lower sintering temperatures for the printed substrates has a huge impact on the device performance. While substrates heated at 350°C showed efficiencies around 9 %, sintering temperatures of 300 °C or lower were not able to produce a working solar cell. If we relate the performance of the solar cells and SEM images, it can be noticed that at 250°C and 300°C the carbon films are well packed which may provide the limited sites for the infiltration of the perovskite precursor solution as compared to the film annealed at 400°C.

Electrochemical Impedance Spectroscopy (EIS) analysis

EIS analysis has been performed on the champion device obtained in the above experiment. To elucidate the role of contacts, layers, charge generation, drift and diffusion of charge carriers, recombination and the photovoltaic performance Electrochemical Impedance Spectroscopy (EIS) analysis has been performed. The frequency domain in the Nyquist plot which belongs to the photo generation and recombination process has been

presented in Figure 5.2. The behavior of the recombination or charge transfer-resistance R_{CT} near short circuit is dominated by the interface between the hole conductor and the layer under the holes [14]. In conventional mesoporous PSCs with the structure of TiO_2 /perovskite/HTM/Carbon , there are mainly three interfaces of TiO_2/perovskite, TiO_2 /HTM, and HTM/carbon, equivalent to three RC elements in the equivalent circuit [63, 69, 100, 132].

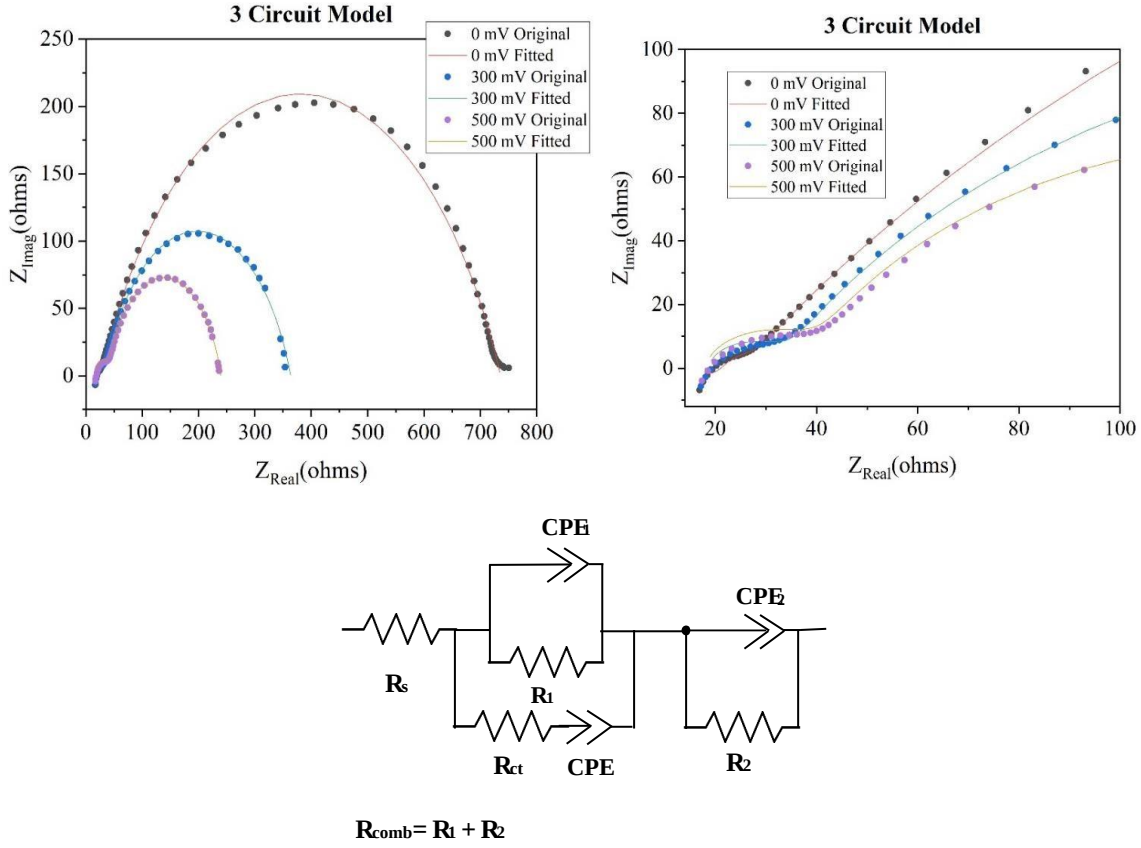

Figure 5.2: Nyquist plots of mPSCs biased at zero, 300mV and 500mV with three circuit equivalent fitted. Equivalent three circuit model used to fit the impedance results.

However, some devices are represented by only two RC elements which represent interfaces at TiO_2/perovskite and perovskite/Carbon and assumed that perovskites act as

both the light harvester and hole transporting of HTM free PSCs [67, 68]. Where the first semicircle stands for the impedance at the perovskite/Carbon interface and the second semicircle represents the impedance at the TiO_2 /perovskite interface. The larger semicircle in low frequency indicates much slower recombination rate for perovskite.

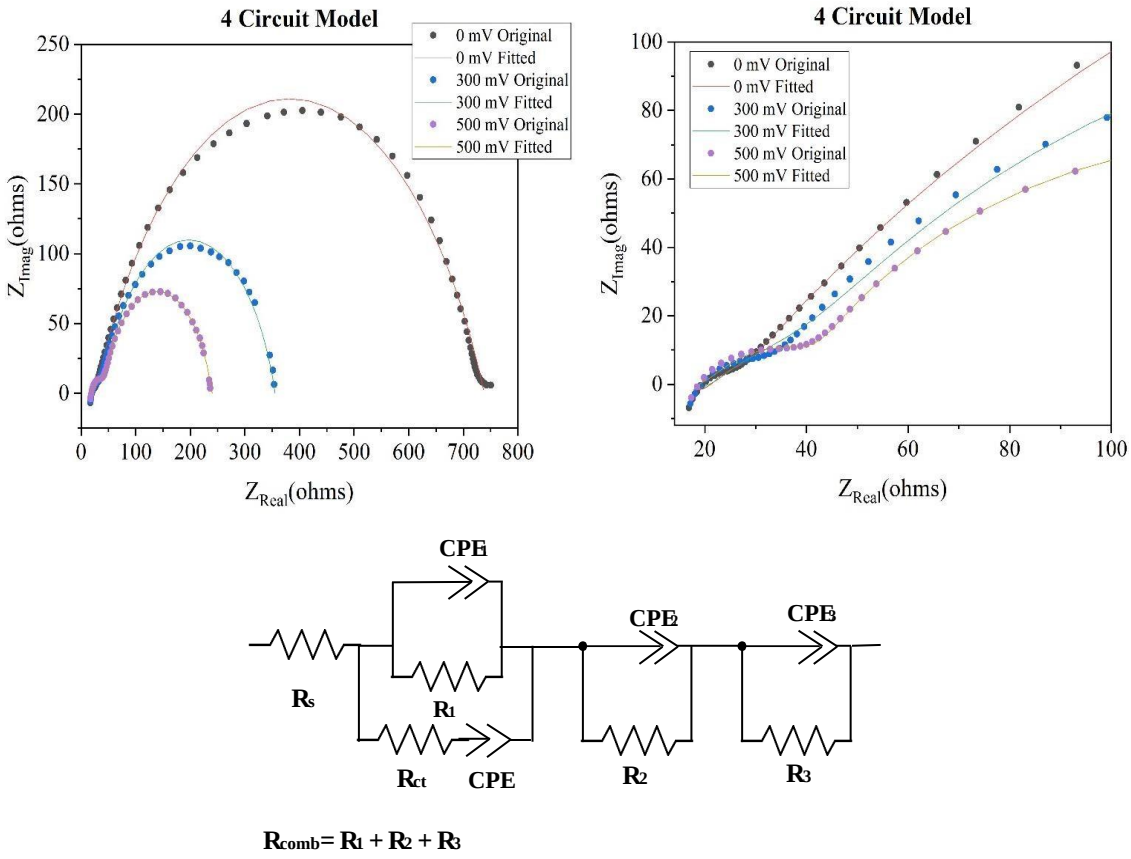

Figure 5.3: Nyquist plots of mPSCs biased at zero, 300mV and 500mV with four circuit equivalent fitted. Equivalent four circuit model used to fit the impedance results.

EIS measurement plots of the mPSCs from 1 MHz to 0.01 Hz at an applied bias of zero, 300 mV and 500mV under dark condition have drawn in Figure 2 no distinct transmission line behavior has been observed in given conditions. In case of zero dc biasing

three semicircles have been obtained, however in case of in case of 300mV and 500mV two semicircles has been observed. The first semicircle in the low-frequency region represents the resistance at TiO_2/Perovskite interface. The semicircle at high-frequency region represents the charge transfer impedance (Rct) at the interface between the perovskite and carbon electrode. Rs represents the sum of the sheet resistance of the FTO, conductive glass and contact resistance at the TiO_2/ITO interface. The fitted parameters are listed in the table 5.1. These two semicircle results are similar to previous [51, 59, 114, 133] results.

Table 5.1: Summary of the parameters of EIS investigated in Figure 2 and 3 with fitting the Nyquist plots.

0 mV				
Model	Rs	R_{ct}	R_{comb}	Goodness of fit
3 Circuits	19.8	20	718.7	5.42E-03
4 Circuits	16	21.3	714.8	1.35E-03
300 mV				
Model	Rs	R_{ct}	R_{comb}	Goodness of fit
3 Circuits	20.2	26	339.7	5.1E-03
4 Circuits	14.0	26	335.0	1.59E-03
500 mV				
Model	Rs	R_{ct}	R_{comb}	Goodness of fit
3 Circuits	19.06	30.1	219.4	3.3E-03
4 Circuits	15	27.9	225.5	9.5E-04

The Nyquist plots of zero bias are composed of three semi-circles. A small arc at high frequency, a large arc at low frequency and again a small arc at low frequency. The mPSCs have ITO/c-TiO_2/m-TiO_2/m-ZrO_2/m-carbon layers and perovskite has been infiltrated through carbon layers to all other layers. The starting point in the real part of the Nyquist

plot resembles to the series resistance Rs. The performance of the mPSCs solar cells is a result of the synergistic effect produced by all of these layers in combination with perovskite. The value of resistance R_1, R_2, R_3, is mainly depend upon recombination across m-TiO_2, m-ZrO_2 and m-carbon layer hence it has varied during different biasing conditions. As the biasing voltage increases the contact between mesoporous layers and perovskite enhances which improves the electron extraction efficiency and reduces the recombination rate. As a result, the mesoporous device exhibits a lower charge transfer resistance (5.43 Ω, 27.9 Ω) and a higher recombination resistance (832.3 Ω, 225.5 Ω) at zero and 500mV biasing. The deprived electron extraction ability of c-TiO_2 affect the device performance, hence it is very important to have a pinhole free and compact c-TiO_2 on the other hand a carbon electrode with insufficient hole extraction leads to a serious hole accumulation in the-ZrO_2 results in serious carrier recombination leading to the poor device performance. A larger semicircular diameter in the low frequency region, indicating in a greater recombination resistance at the mesoporous layers and perovskite interface. However, goodness of fit for 4 -circuit model (9.5×10^{-4} for 500mV biasing) is better than the 3-circuit model (4.9×10^{-3} for 500mV biasing) and will able to explain function of all 4 layers and interface between layers and perovskite.

Conclusion

The deprived electron extraction ability of c-TiO_2 affect the device performance hence it is very important to have pinhole free and compact c-TiO_2 on the other hand a carbon electrode with insufficient hole extraction leads to a serious hole accumulation in the m-ZrO_2 results in serious carrier recombination leading to the poor device performance. As biasing voltage increases the recombination resistance reduces and improves device performance.

Chapter 6: Synthesis of 1D Perovskite Extra-Long (Centimeters) Micro Rods

Introduction:

For improving mPSCs device, synthesis of one-dimensional microrods (4mm5mm) of PbI_2, $PbBr_2$, and $CH_3NH_3PbI_3$ ($MAPbI_3$) has been explained in this Chapter. These microrods consist of unique structural and morphological properties and has been grown at room temperature. After the mechanical exfoliation of two-dimensional (2D) graphene [134], it has been proved that material (conductor, semiconductor and insulator), when scaffolded to its physical limits, exhibits extraordinary intrinsic properties over their bulk counterparts [135]. Extraction of 1D and 2D crystals is the subject of massive research due to their unprecedented matter quality from a magnetic lattice distorted to superconducting characteristics [50, 136]. Crystal contains less heterostructure defects and provide better electronic, mechanical, optical and transport properties, hence technologically more suitable in diversified engineering and medical applications [137]. Among the all available 2D crystals [138], the semiconductors specifically transition metal halides (TMHs) family is pertinent in electronic and optoelectronic devices due to good intrinsic properties such as optical bandgap, absorption coefficient and carrier diffusion length [139, 140]. Moreover Lead-based TMHs have been attained great attention because they used to synthesize metal halide perovskite solar cells (PSCs). PSCs have certified 22.7% power conversion efficiency (PCE) and performance has been progressively improving [141]. Polycrystalline films [142] and bulk crystals [143] are two main forms of perovskites. Currently, film format PSCs has been intensively researched, produced high-efficiency solar cells and moving towards commercialization with addressing all challenges during upscaling [46, 79, 144, 145]. However, perovskite single crystals are not thoroughly explored by researchers till now. Perovskites single crystals shapes vary from three-dimensional large sized single

crystals [146, 147], two-dimensional nanoplates[148, 149], one- dimensional nanowires [150, 151], to zero-dimensional quantum dots [152, 153]. Shape and size of perovskite crystal have profound impacts on electrical and optical properties of cell [154]. The carrier diffusion length measured in perovskite has been strongly dependent on material morphology, which makes single crystals, highly conducive because single crystals have less defects [155]. However, conventional crystals growth procedures have been very complicated for non-experts [156, 157] mostly require seed crystal, control environment and suffers from very slow growth rates [118, 158]. Furthermore, reproducible device performance and cost-effective solar energy production have not been achieved by single crystal technology. Many questions remain to be addressed regarding the crystal chemistry of perovskite materials, and the nature of charge transfer in a single crystal [159].

A crystal structure provides positive identification of a single crystal and give absolute proof that the compound or complex is the stated material. It provides the exact connectivity of the atoms and the bond distances and angles between these atoms in the solid state which result in the complete identification of the compound. It also provides Inter and Intra molecular interactions which may provide insight into the chemistry and properties of the compound. The studies of all above stated fundamental intrinsic photo physics is necessary for further improvement of functions of single crystals perovskites. In this context, we performed solution-based synthesis of PbI_2, $PbBr_2$ and $MAPbI_2$ perovskite to produce 1D crystal milli rods. The analyses confirm the existence of strong interactions between different stable groups in these crystals. The morphological, structural and thermal properties of the one-dimensional perovskite micro-rods have been examined using various characterizations.

Experimental

1 M solution of PbI_2 (462mg), MAI (159 mg), $PbBr_2$(367 mg) and MABr (112 mg) have been prepared with solvents in all possible combinations (Figure 6.1) and kept for overnight stirring at 70 °C with magnetic beat, results transparent yellow solution of PbI_2 and MAI and transparent white solution of $PbBr_2$ and MABr. After cooling the solutions at room temperature, equi molar solutions of PbI_2 and MAI is mixed to form $MAPbI_3$. Similarly, $PbBr_2$ and MABr is added to form $MAPbBr_3$ perovskites.

Figure 6.1: PbI_2 Perovskite precursor with solvents after first heating (1) $PbBr_2$ + DMF (2) $MABr_2$ + DMF (3) PbI_2 + IPA (4) PbI_2 + DMF (5) PbI_2 + MAI + DMF (6) PbI_2 + MAI + IPA (7) MAI + IPA (8) PbI_2 + MAI + DMF + IPA.

After mixing perovskites are in thick precipitate form, however stirring and heating them again at 100 °C gives a clear yellow solution of $MAPbI_3$ and the transparent blue solution of $MAPbBr_3$. Second heating is performed for rest of the solutions also. Crystallization occurs after cooling down solutions to room temperature without stirring. After some time, crystals observed at the PbI_2 (Figure 6.2A), $MAPbI_3$ (Figure 6.2B) and $PbBr_2$ (Figure 6.2C). However, other solutions do not produce any crystals. All the crystal

maintains their size after removing liquid. Crystals have been dried at room temperature without heating or blow drying for further characterizations.

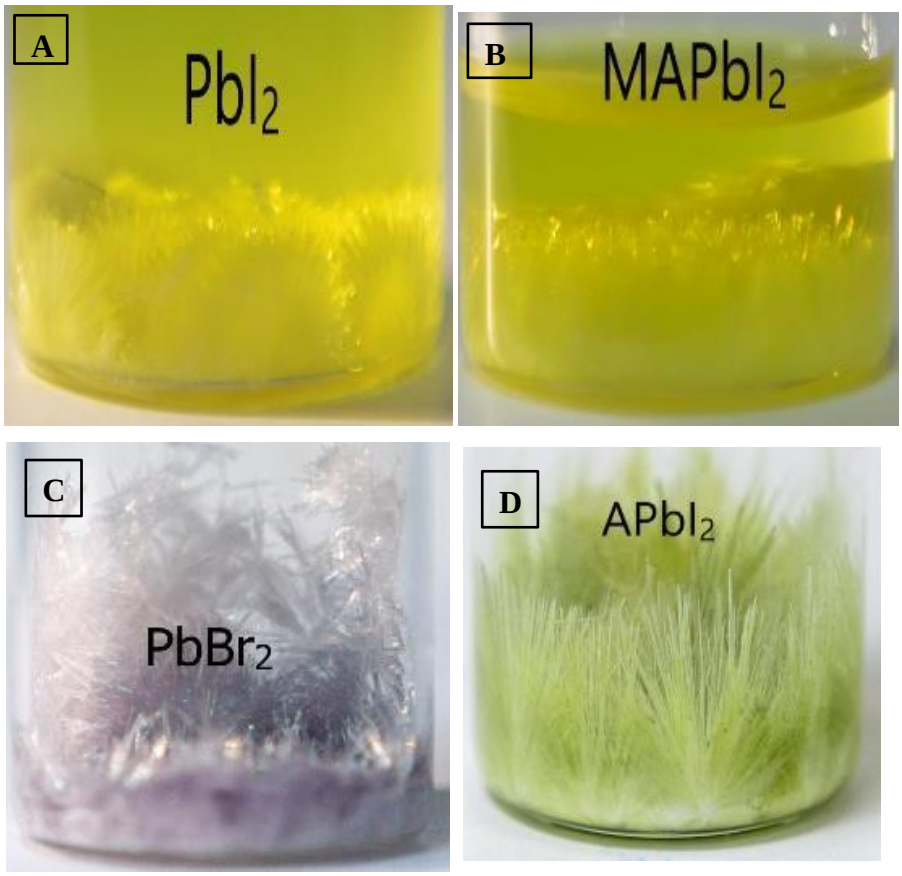

Figure 6.2: Pictures of crystals taken from outside the glass bottle. (A) PbI_2 crystals inside the DMF solution (B) $MAPbI_2$ crystal in DMF and IPA solvents (C) Dry $PbBr_2$ crystals. (D) Dry $APbI_2$ crystals

X-ray Diffraction (XRD)

X-ray diffraction spectra used for structural characterization of crystal shown in Figure 6.3 – 6.6. To compare starting materials with resultant crystals the XRD from the reactant samples was also measured and is included in Figure 6.3 – 6.6.

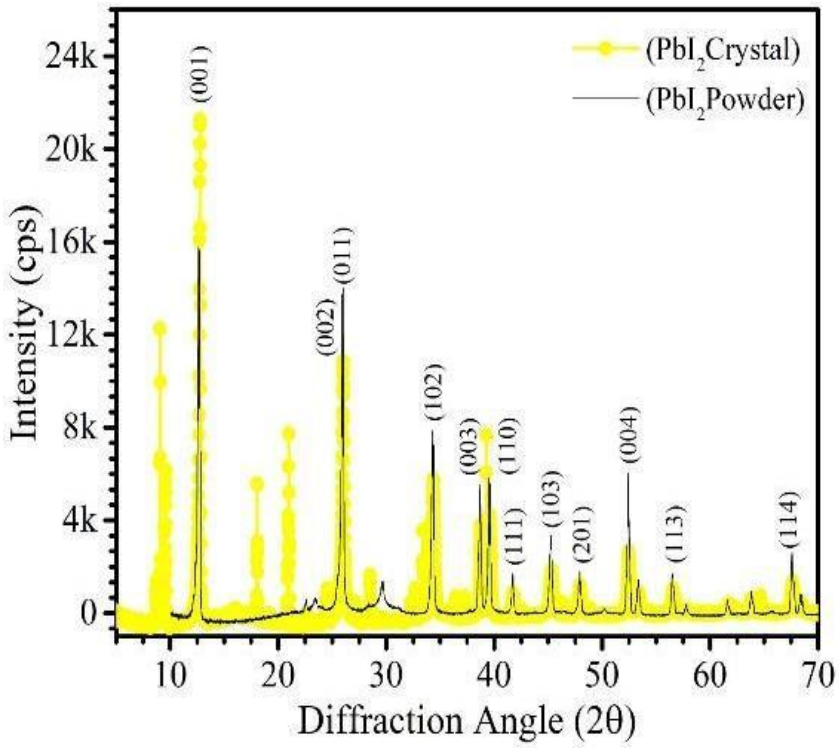

Figure 6.3: PbI_2 crystal (yellow data points) and PbI_2 powder (black line) diffraction patterns obtained at room temperature.

Figure 6.3 corresponds to the spectrum of the PbI_2 crystal (yellow circles) and original PbI_2 powder (black lines) procured from Sigma-Aldrich. Both showed the hexagonal system (P $\bar{3}$ m 1 (164) space group) with a = b = 0.4557 nm and c = 0.6979 of PbI2 and 2H polytype structure (hematite, JCPDS file No. 07-0235). The most intense diffraction peak is obtained at 12.60° that corresponds to the (001) lattice plane. However, peak intensity at this angle for PbI_2 crystal is much higher than the PbI_2 powder. Other prominent peaks observed at 25.5°, 25.93°, 34.2°, 38.67° and 52.3° corresponding to the (002), (011), (102), (003), and (004) lattice planes of PbI_2. Peaks (113), and (114) are observed at higher diffraction angles 56.4° and 67.5° as indicated in the Figures. The crystalline orientations of the present work are different from previous literature for $MAPbI_2$ films as well as bulk

crystals [160, 161]. In the grown crystal the d- spacing is fingerprints of specific sample which is determined by XRD. The d- spacing for the PbI_2 crystal is more the original powder hence shifting the lattice plane at lower angles with high intensity signals. The shifting of plane spacing (d-value) is due to rearrangement of lattice positions which is due to doping of ions, atoms and impurity. Another thing which affects the d value is stress forces either electrostatic forces or external forces. Although the basic structure is a simple I-Pb-I layered structure with a $[PbI_6]4-$ near-octahedron being the basic building block, there are many ways of stacking the layers which results in around 23 polytypes. [162]

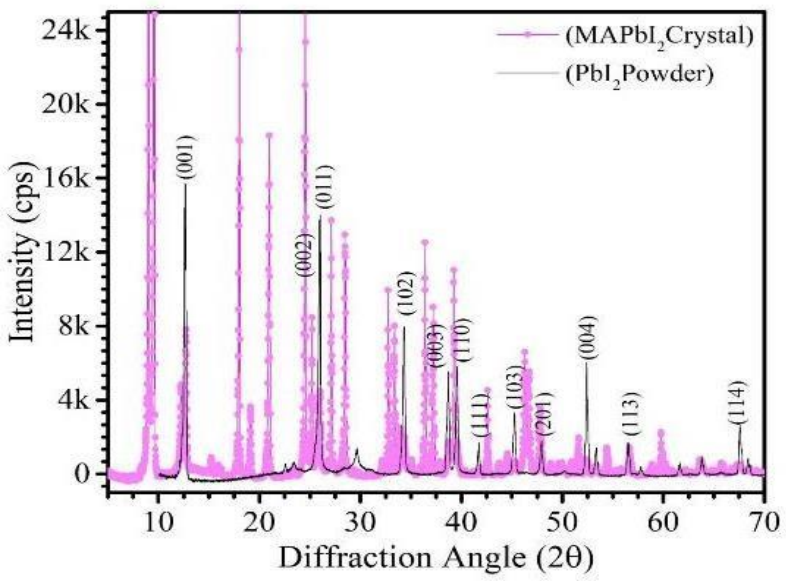

Figure 6.4: $MAPbI_2$ crystal (magenta data points) and PbI_2 powder (black line) diffraction patterns obtained at room temperature.

The $MAPbI_2$ crystal adopted the hexagonal P3m1 space group at room temperature. High intensity diffraction peak which intensity is more than 25K were obtained at lower angle positions (Figure 6.4) 9.0°, 9.5°, 18.1° and 24.5 overwhelmingly dominate the diffraction pattern. The diffraction peak widths (fwhm) for the given angles are 0.09°, 0.01°,

0.064°, and 0.064° generally in the range 0.1- 0.5. Hence, high intensity diffraction peaks were obtained signifying that the crystals were reasonably well- crystallized. The c-axis diffraction peaks obtained in PbI_2 powder at (001), (002), (003), and (004) is also obtained in $MAPbI_2$ crystals at angles 12.67°, 25.5°, 38.67° and 52.3°. The unidentified peaks did not match either the pure PbI2 or MAI tetragonal phase, which was stable at room temperature. This suggested that intermediate phase, which might be a complex of PbI_2-DMF, complex of PbI_2-MAI-DMF, or hydrate compound $(CH_3NH_3)_4PbI_6 \cdot 2H_2O$ is present. [163]

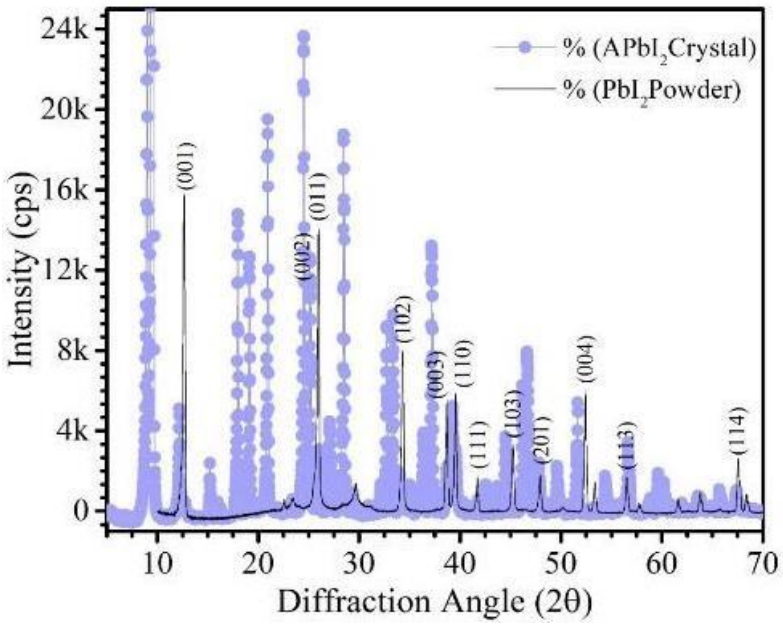

Figure 6.5: $APbI_2$ crystal (Blue data points) and PbI_2 powder (black line) diffraction patterns obtained at room temperature.

The $APbI_2$ crystal is the hexagonally close-packed layer of lead between two planes of iodine in 4H polytype structure. This crystallizes space groups P3m1 (156) with a = b = 0.4554 nm and c = 1.3962 nm. The peak is obtained at 6.32°, 12.67°, 19.054°, 22.52°,

23.42°, 25.49° corresponds to the (001), (002), (003), (010), (011), (004) lattice plane shown in Figure 6.5. For same lattice planes ((001), (002), (003), (010), (011), (004)) the PbI_2 powder peaks are obtained at angle 12.60, 25.5°, 25.93°, 34.2°, 38.67° and 52.3°. Hence all diffraction peaks are shifted towards lower diffraction angles with improved intensity except (001) peak. 001 lattice plane intensity is higher in PbI_2 powder. However, significant high intensity new peaks have been appeared in the $APbI_2$ crystals. [164]

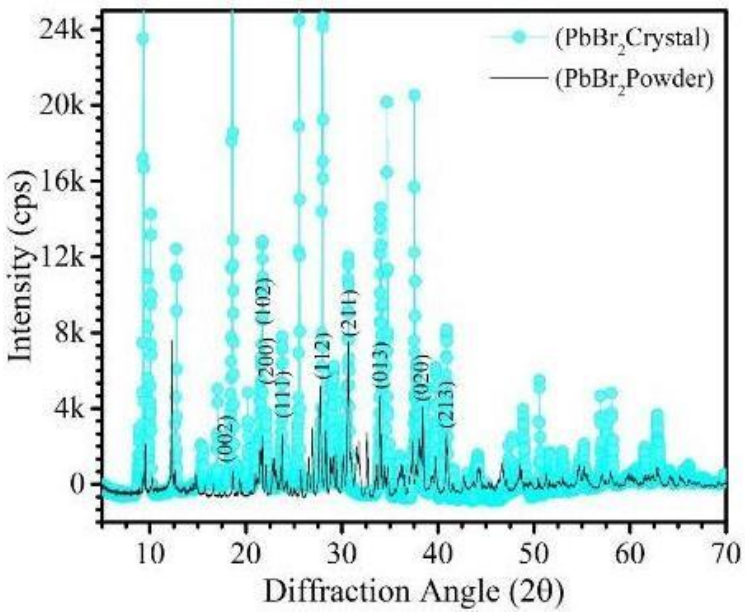

Figure 6.6: $PbBr_2$ crystal (cyan data points) and $PbBr_2$ powder (black line) diffraction patterns obtained at room temperature.

It should be noted that lead halide has a highly oriented growth direction along the a -axis in the case of $PbBr_2$ and along the c -axis for PbI_2. Figure 6.6 corresponds to the spectrum of the $PbBr_2$ crystal (cyan circles) and original $PbBr_2$ powder (black lines) procured from Sigma-Aldrich. Both showed the orthorhombic system (P n m a (624) space group) with a = b = 0.8059 nm and c = 0.4732 of $PbBr_2$ (hematite, JCPDS file No. 07-0235). However, the exciton absorption bands shifted to short wavelength (higher photon

energy) for $PbBr_2$ crystals compared to powder. Peak intensity at angles for $PbBr_2$ crystal is much higher than the $PbBr_2$ powder. Other prominent peaks observed at 14.37°, 18.58°, 21.63°, 22.04° and 23.69° corresponding to the (101), (002), (011), (102), and (111) lattice planes of PbI_2. Peaks (112), and (211) are observed at diffraction angles 28.76° and 30.58° as indicated in the figure 3 (D).

Raman Spectroscopy:

Raman spectroscopy was used to further characterize the crystalline structure of individual platelets for each lead halide compound. Characteristic internal vibrational appear (figure 6.7) at three energetic regions, at 600−1100 cm^{-1} (C−N stretching), around 1300−1600 cm^{-1} (CH_3 and NH_3 bending) and at around 3000 cm^{-1} (CH_3 and NH_3 stretching).

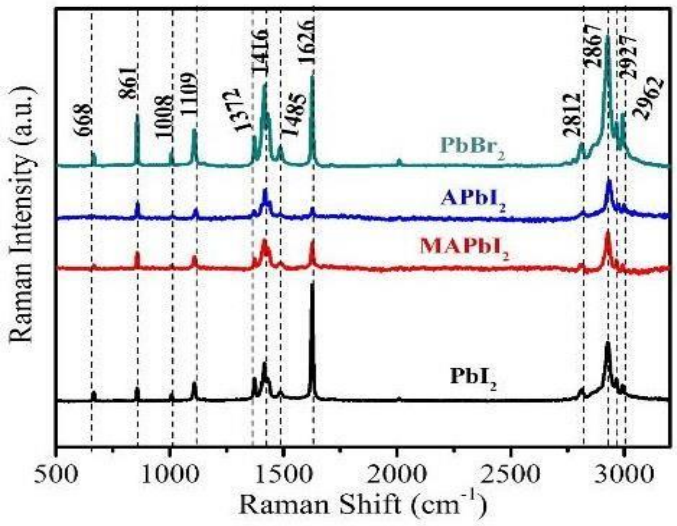

Figure 6.7: Raman spectra of PbI_2, $MAPbI_2$, $APbI_2$ and $PbBr_2$ rods.

Qualitatively, each PbI_2, $MAPbI_2$, Advanced PbI_2 ($APbI_2$) and $PbBr_2$ shows similar vibrational properties with three energetic regions, hence there is no phase change during the crystallization. These ranges are consistent with previous computational reports. The

frequency modes would involve twist around the C-N axis (668, 861 cm^{-1}), vibration along the C-N axis (1008,1109 cm^{-1}), bending of the C-H bonds (1372,1416 cm^{-1}), bending of the N-H bonds (1485, 1626 cm^{-1}), stretching of the C-H bonds (2812, 2867 cm^{-1}), and stretching of the N-H bonds (2927, 2962 cm^{-1}).[165-167]

Fourier Transform Infrared Spectroscopy (FTIR)

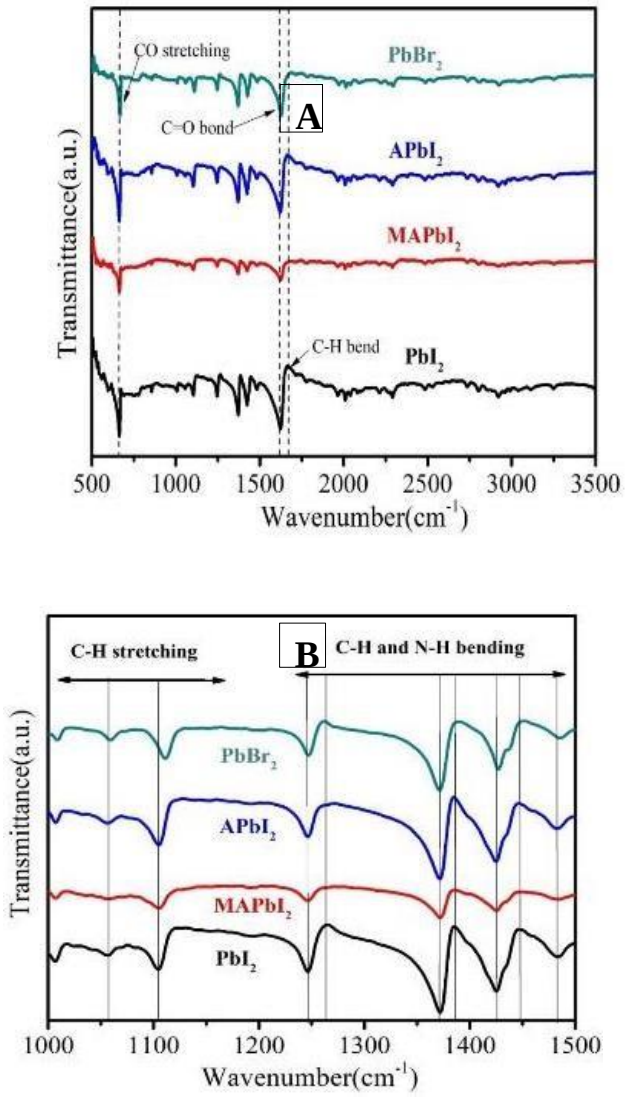

Figure 6.8: FTIR spectra of PbI_2, $MAPbI_2$, $APbI_2$ and $PbBr_2$ rods for range (A) 500 - 3500 cm^{-1} and (B)1100 – 1500 cm^{-1}.

The chemical structure of the synthesized crystals has been examined by the FTIR measurements as shown in Figure 6.8. The FTIR vibrations at 660 and 860 cm^{1}show the features characteristic to CO stretching and C-N stretching. Peaks at 1007, 1058 cm^{-1} (not in present in MAPbI) belongs to sp^3 C-H stretching. 1105 cm^{-1} peak is shifted at 1115 cm^{-1} in $PbBr_2$ (shown in figure 5 b). Peaks between 1250 -1550 cm^{-1} of the frequency of vibration belongs to C-H and N-H bending. However, overshoots at 1265 and 1385 cm^{-1} is not visible in MAPbI. The stretch vibration due C=O bond appeared at 1620 cm^{-1} (which is shifted at 1625 cm^{-1} in $PbBr_2$) and at 1660 cm^{-1}.

However, the C=O bond strength decreased with the MAI addition in PbI_2. It has been observed that there was no O-H stretching vibrations around 3500 cm^{-1} suggesting no hydrated or adsorbed water existed. [168, 169] The OH oscillations of water molecules are embedded in such a way that they affect the hydrogen bonds between the NH group and the iodide and bromide because the N-H stretch vibrations are known for their sensitivity to the strength of the interaction between the methylammonium and the iodide.

FTIIR results reveal the existence of a strong interaction between different groups in the crystals which cause not only the displacement of the position, but also a variation in the intensity of the peaks or even the appearance of new peaks. The MAI ions are not present in the solutions except $MAPbI_2$ but C–H and N-H stretching and bending vibrations are very similar for all the dry crystals. Hence effect of DMF [$(CH_3)_2NC(O)H$] during the crystallization and after drying of crystals is evident. The FTIR peaks in the 500 - 1700 cm^{-1} range well corresponds to the Raman features as shown in Figure 4. Though, some peaks cannot be found in the infrared spectra, but are present in the Raman spectra precisely above 1700 cm^{-1}. This is because the vibration energy is Raman active if it causes a change in

polarizability whereas IR active intensities may be stronger or weaker than expected, depending on dipole moment. [170, 171]

Th

thet

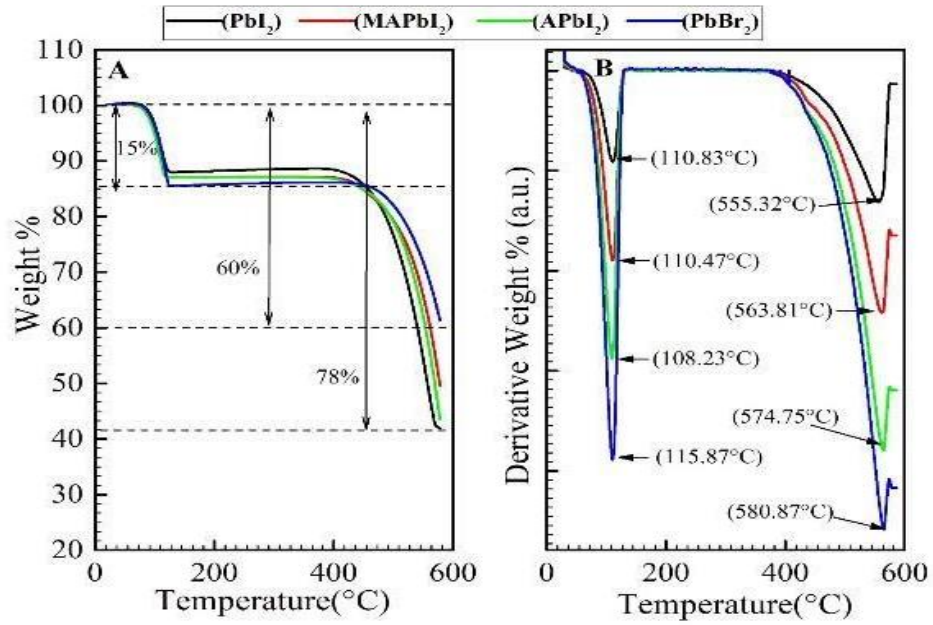

Figure 6.9: TGA heating curves of individual crystals expressed as (A) weight % and its (B) derivatives as a function of applied temperature

Thermogravimetric analysis (TGA) is used to determine the mass loss behavior of the individual crystals. The TGA curves are presented in Figure 6.9. Where two mass losses are observed. 1st is between 110°C - 116°C which shows less than 15% for all samples. Minimum (12%) mass loss is obtained in PbI_2 crystal at 110.83°C and maximum (15%) is in $PbBr_2$ crystal at 115.87°C. The TGA weight loss profile implies that these inorganic materials have not undergone thermal decomposition or sublimation during 1st stage and mass loss is solely due to the removal of absorbed moisture from the crystals.

Because sublimation has been defined as the point where at least 20% of mass loss of the sample has happened. [172] The 2nd mass observed between 550°C and 600°C for crystals. This sequential decomposition is observed in the perovskite where organic component decomposes by the subsequent loss of HI and CH_3NH_2 because the latter species is more tightly incorporated in the perovskite matrix. Sequential decomposition pathway occurs only when the organic species are combined into the perovskite structure. This type of decomposition is not observed in the pure PbI_2 and MAI powder. PbI_2 powder (99% pure) undergoes 90% weight loss at 646°C and MAI undergoes 100% weight loss at 185 °C, which means pure organic material and inorganic material shows single step mass loss decomposition behavior. [174] This single step loss is not observed in the TGA of all the crystal samples. Crystal decomposition is in good agreement with previous results.

Differential scanning calorimetry (DSC)

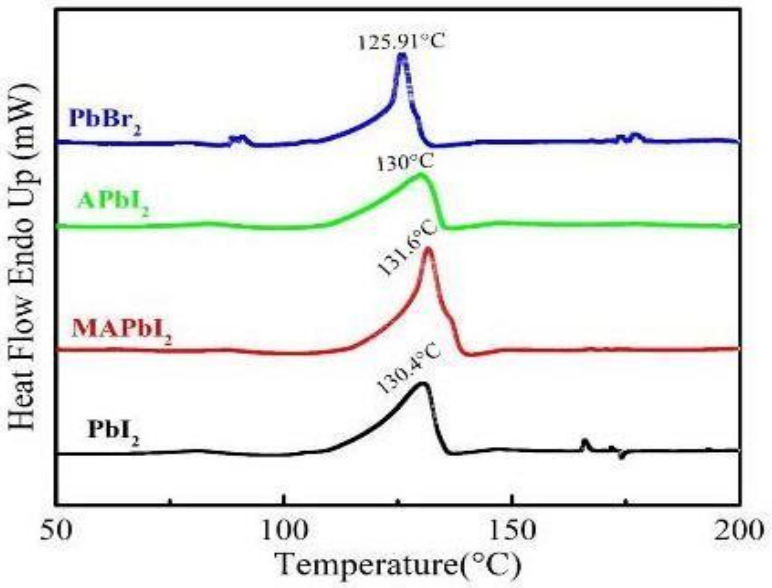

Figure 6.10: DSC heating curves of individual milli-rod crystals.

DSC was used to effectively detect phase transitions and gain further insight into the thermal behavior of the crystals. The heating−cooling cycle DSC measurements over the temperature range of 35-300°C has been carried out, and corresponding results are shown in figure 6.10, which revealed narrow endothermic peaks between 125 -132°C. This can be explained by realizing that a polymorphic transformation took place while heating. [175]

Scanning Electron Microscope (SEM)

Figure 6.11, 6.12 and 6.13 show morphology of crystals at different magnification. It has been found that the resulting crystals were in the form of smooth, rectangular platelets like structure but different in size. It can be clearly observed from morphological examination of figure 6.11 that the crystallites grow in longitudinal dimension as narrow platelets with lengths up to 400 - 500 mm. The lateral dimensions of the crystals were also calculated and shown in figure 6.12.

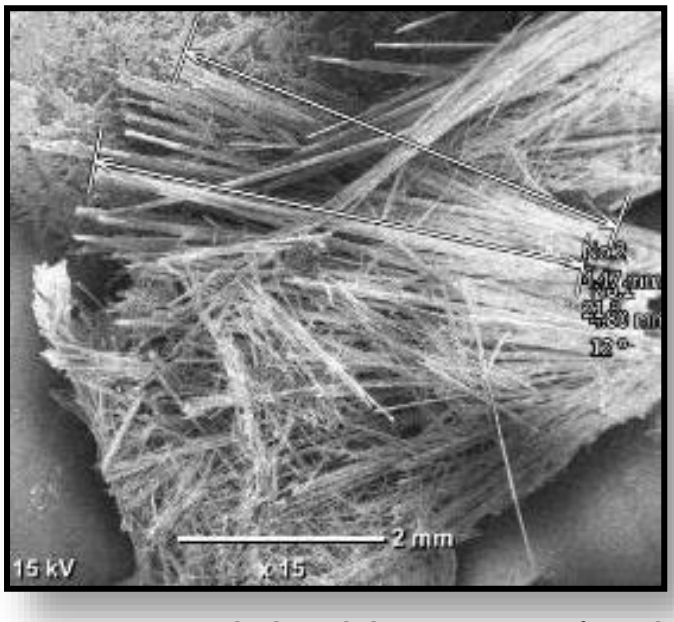

Figure 6.11: Longitudinal morphology examination of crystals.

The results in Figure 6.12 showing that they are bundles of crystals with thickness 10−100 μm (diameter). All four samples have shown the same structure at this level.

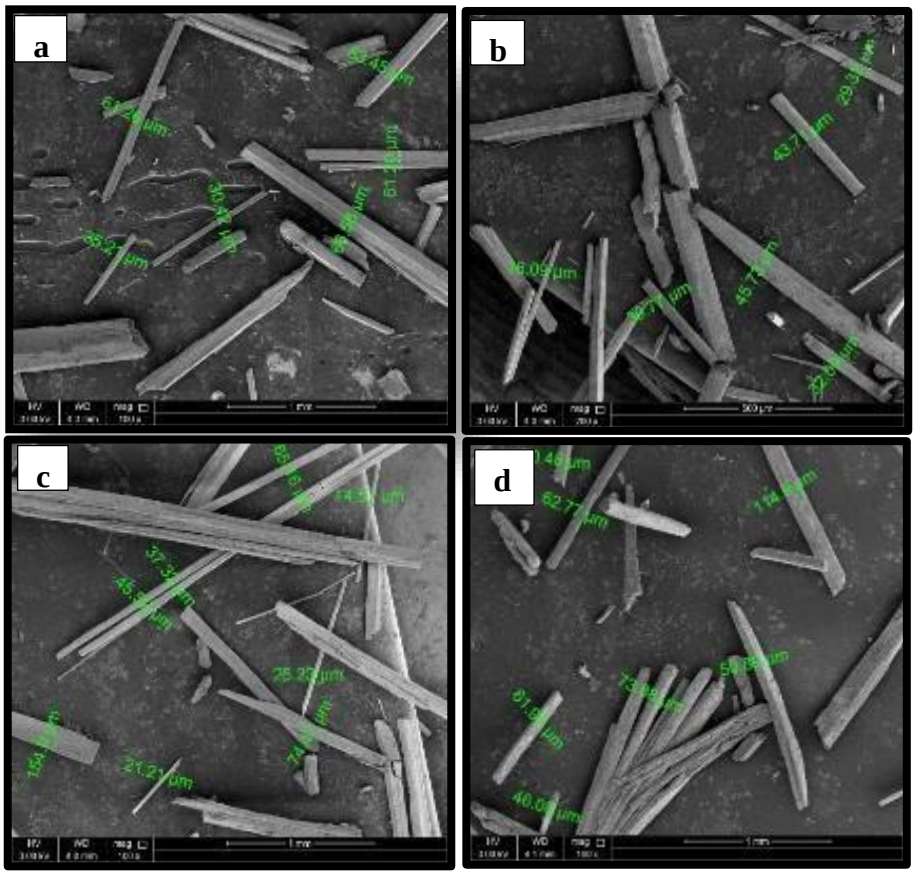

Figure 6.12: Dimension of crystals. PbI_2 (a), $MAPbI_2$ (b), $APbI_2$ (c) and $PbBr_2$ (d)

From surface morphology of PbI_2, $MAPbI_2$ and $APbI_2$ (figure 6.13) it has been observed that there are holes with diameters of nanometer throughout the body of the crystal. The higher magnification image of the crystal shows many 1D nanowires, these are perpendicular to each other and their lengths range from one nanometer to more are joined longitudinally to form a large crystal.

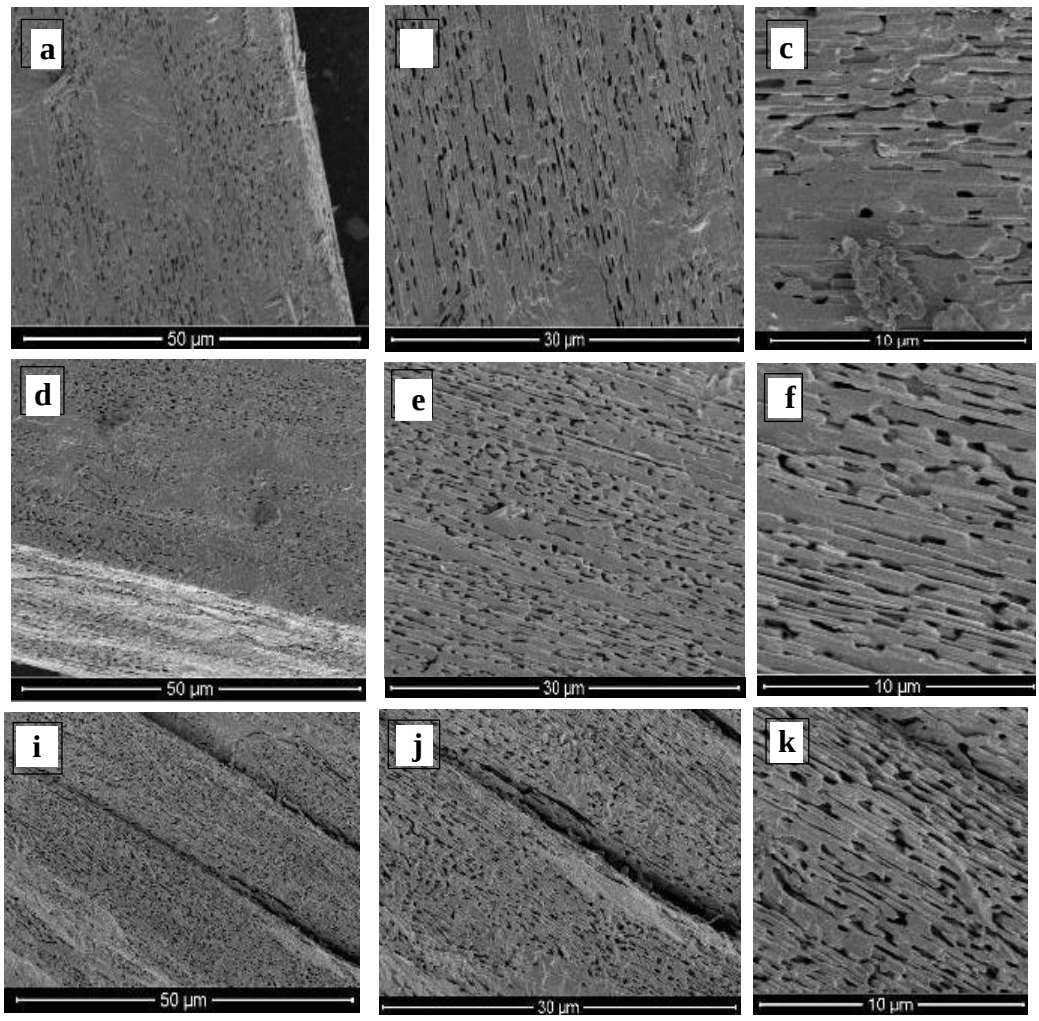

Figure 6.13: SEM images of crystal rods of PbI_2 (a, b and c), $MAPbI_2$ (d, e and f), $APbI_2$ (I, j and k)

Due to little difference in the dimension of nano wires while joining they have space between wires which results in holes. Hence the surfaces of these crystals are not smooth at nano level, but the joint between nano wires are strong hence overall big crystals are compact.

Furthermore, crystals inner body is having the same characteristics as surface which is visible from outside, hence we may conclude that the crystals are not hollow from inside. All these properties are further confirmed with TEM. To the best of our knowledge, this is the first report of PbI_2 1D crystals of such morphological characteristics. It has been

observed that the porous structure of PbI_2 support efficient conversion of PbI_2 to $CH_3NH_3PbI_3$ perovskite, resulting in a highly oriented perovskite film [176].

It can be noticed that the surface morphology of $PbBr_2$ microcrystals is quite different from the PbI_2 microcrystals (Figure 6.14). It has been observed that there are holes with diameters of a nanometer in their bodies.

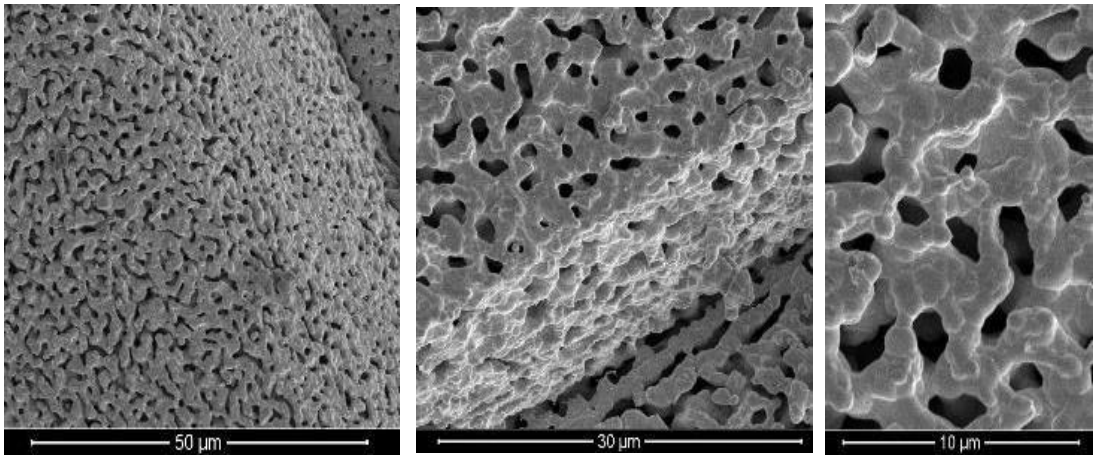

Figure 6.14: SEM images of crystal rods of $PbBr_2$

However, one dimensional nanowires are not seen in the $PbBr_2$ microcrystal. The higher magnification image of the $PbBr_2$ microcrystals shows the presence of many adjacent nanodiscs on their surfaces which are combined parallel fashion to form a large microcrystals. However, it has been observed that pores of $PbBr_2$ crystal are spherical and relatively bigger in size as compared to PbI_2 microcrystals. It is, further noticed that the surfaces of the developed microcrystals are not smooth at the nanometric level, however, the joints between these nanodiscs are strong enough to grow all big microcrystals possessing uniform properties.

Energy-dispersive X-ray spectroscopy

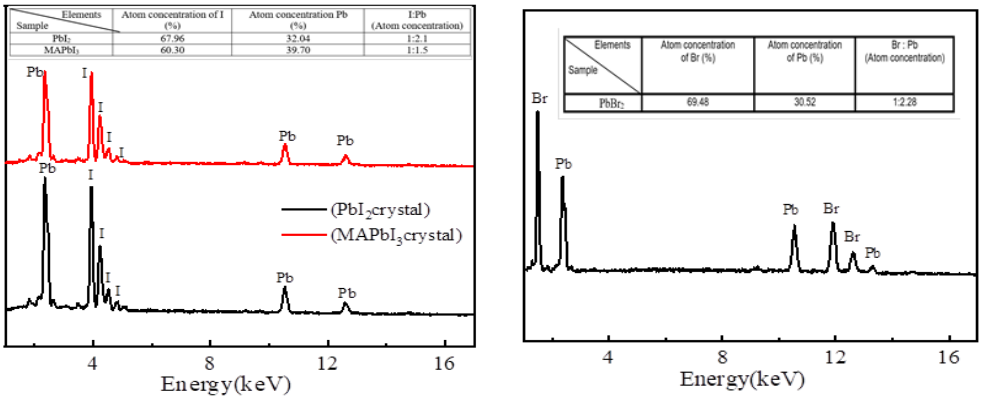

Figure 6.15: EDS spectrum of the micro-rods: PbI_2 and $MAPbI_3$.

The compositional analysis of the developed microcrystals has been performed using EDS and the results are shown in Figure 6.15 (a & b). For all crystals the EDS spectra show well defined peaks corresponding to elements such as carbon lead, Bromine and Iodine. There are two feature peaks at 2.48 and 10.5 keV corresponding to the lead and two feature peaks at 0.5 and 3.98 keV which can be assigned to iodine elements in PbI_2 crystals (Figure 6.15 a). In the case of PbI_2, the atomic composition of the microcrystals indicates the presence of Pb with I in a 1:2.1 ratio, which is in close agreement with the PbI_2, confirming the formation of pure phases. However, in the case of $MAPbI_3$ this ratio is turned to 1:1.5 confirming the existence of intermediate phases due to the addition of the MAI.

There are two feature peaks at 2.48 and 10.5 keV corresponding to the lead and two feature peaks at 1.5 and 11.75 keV which can be assigned to Bromine elements in $PbBr_2$ crystals (Figure 6.15 b). In the case of PbI_2, the atomic composition of the microcrystals

indicates the presence of Pb with Br in a 1:2.28 ratio, which is in close agreement with the $PbBr_2$, confirming the formation of pure phases.

Transmission Electron Microscopy (TEM)

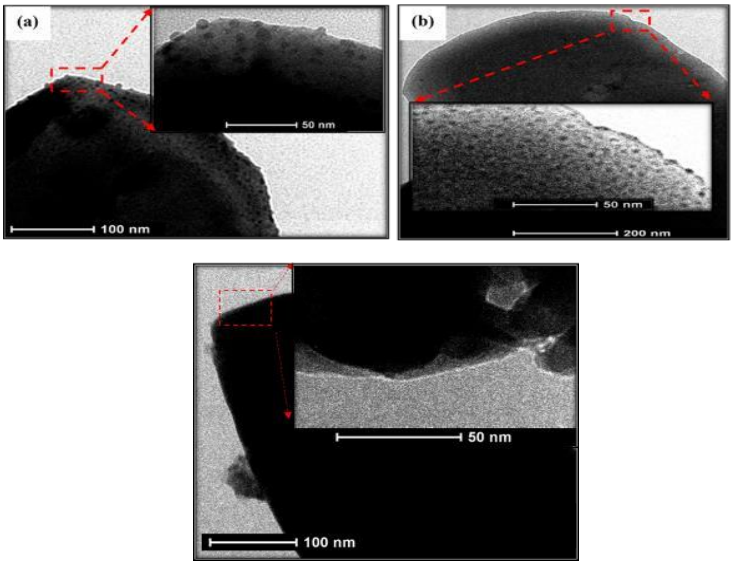

Figure 6.16: TEM images for crystal rods PbI_2 (a), $MAPbI_3$ (b), and $PbBr_2$ (c) Insets shows higher magnification images of the same surface.

In order to have more insight of the developed microcrystals of PbI_2, $PbBr_2$ and $MAPbI_3$, HRTEM analysis was conducted and the results are presented in Figure 6.16 (a, b & c). TEM images taken from the selected region to show the existence of pores in the micro-rods which agrees with the porous SEM observations in Figure 8 and no cracks are observed in a microcrystal surface. Further high-resolution TEM images of PbI_2 $MAPbI_3$ and $PbBr_2$ crystals cannot be obtained because the PbI_2 and $MAPbI_3$ crystals are sensitive to high-energy electron beam irradiation, which can cause distortion of their crystal structure.

X-ray photoelectron spectroscopy (XPS)

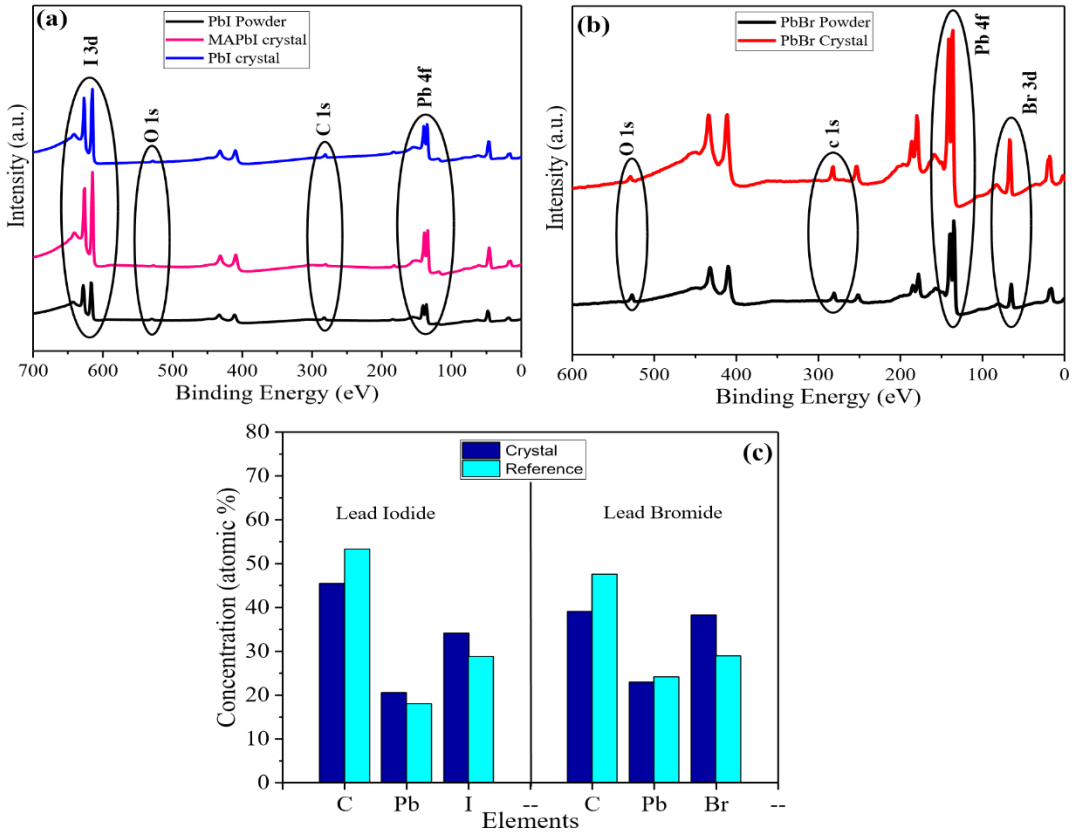

Figure 6.17. XPS survey spectra of the (a) PbI_2 crystal MAPbI crystal and PbI_2 powder (b) $PbBr_2$ crystals and $PbBr_2$ powder. (c) Shows a comparison of the concentrations (in atomic %) of C, Pb, I, and Br between powder crystal.

To determine the elemental composition of PbI_2 crystal and powder (Fig. 6.17 (a)), $PbBr_2$ crystal and powder (Fig. 6.17 (b)), and MAPbI (Fig. 6.17 (a)) crystals, XPS survey spectra were recorded at different time spans in the binding energy range of 0 to 800 eV. To compare starting powder materials with resultant crystals the XPS from the reactant samples was also measured and is included as PbI_2 powder and $PbBr_2$ powder. The identified elements in the samples are lead, bromide, iodine, oxygen, and carbon. Figure 6.17 (c) shows a comparison of the elemental concentrations in crystals and starting

materials. The elemental concentration data are taken from the XPS survey spectra given. It has been found that the atomic concentration of lead (22.49 %) in PbI_2 crystals is more than the reference sample (17.94 %), whereas, atomic concentration of lead 22.88 % in $PbBr_2$ crystals is less than the reference sample 24.15 %. Carbon contents are found to be reduced from 53.32% to 45.4% in PbI_2 and 47.48 % to 38.95 % in $PbBr_2$. However, iodine concentration in PbI_2 crystal 34.10 % is more than reference PbI_2 28.75 %. Similarly, bromide concentration in $PbBr_2$ crystal 38.17 % is more than reference $PbBr_2$ 28.38 %. Carbon contents are found to be reduced from 53.32 % to 45.4 % in PbI_2 and 47.48 % to 38.95 % in $PbBr_2$ after crystal growth.

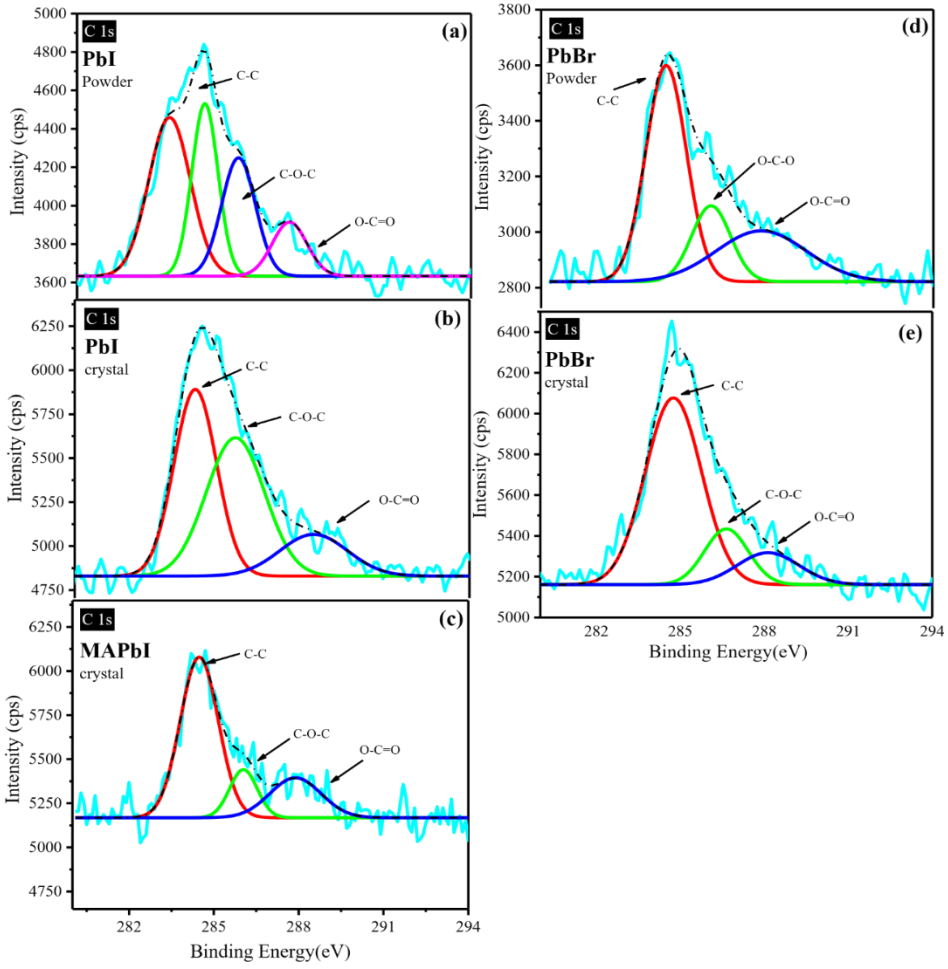

Figure 6.18: Core level XPS spectra for carbon (C 1 s)

XPS core spectra were acquired to explain changes in chemical bonding after crystal growth. Figure 6.18 (a-e) shows the C 1 s spectra on the surface of the crystals and reference powder. The intensity of carbon peaks expressively improves after crystal growth. In C 1 s spectrum for the MAPbI crystals have components at 284.6, 286.3 and 288.3 eV refer, respectively, to C-C bond, C-O-C bond and O-C=O. The peaks are consistent in all the samples.

The O 1 s spectra for crystals and reference powder have shown in Figure 6.19 (a-e), respectively. The components near to 529, 531.5, and 533 eV in the samples assign to metal oxide, organic C-O and organic C=O.

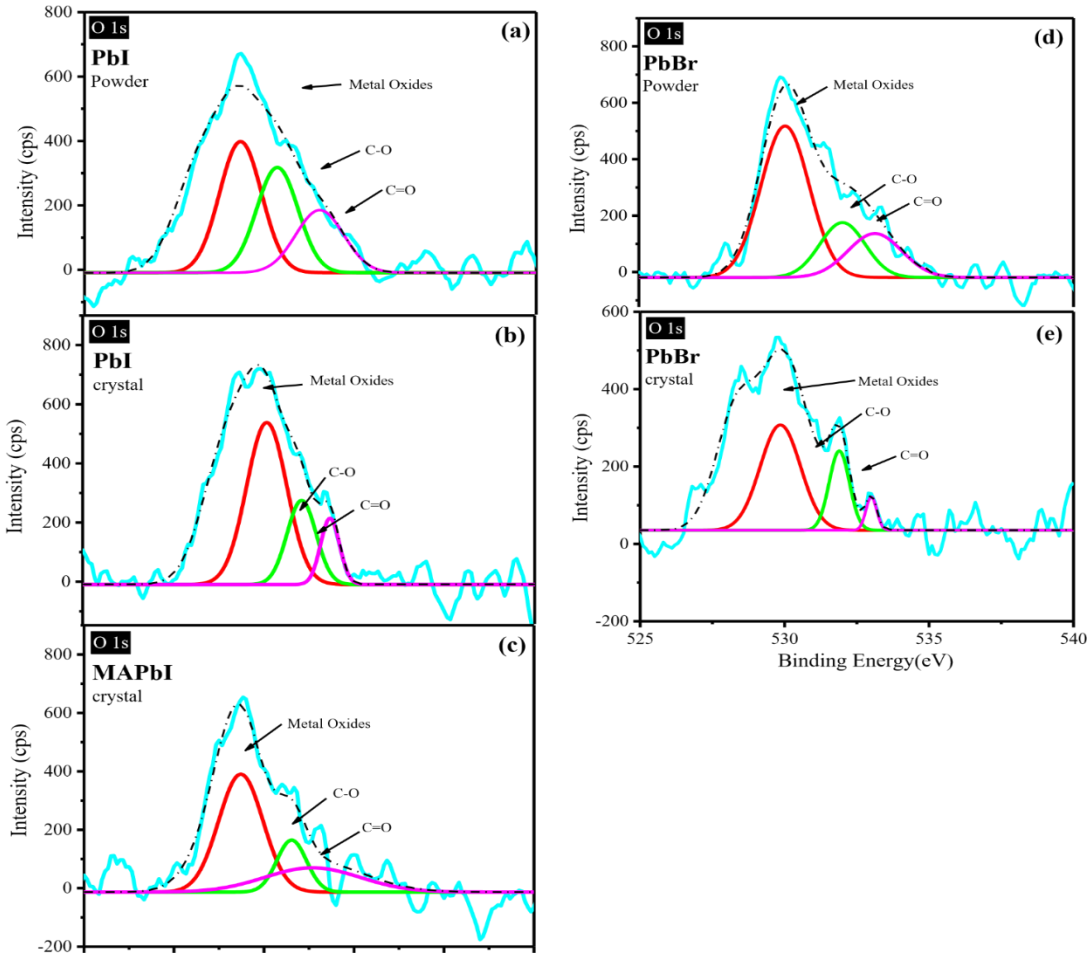

Figure 6.19: Core level XPS spectra for Oxygen (O 1 s)

The core level spectrum of lead (Figure 6.20 a-e) shows two different peaks of lead first at approximately 136.8 eV for Pb $4f_{7/2}$ and other at 141.6 eV for Pb $4f_{5/2}$. Pb4f region has well separated spin-orbit components (Δ_{metal}=4.87eV). The intensity of lead peaks has significantly improved in the crystals as compared to reference powder. Peaks in the Pb4f region of PbI_2 powder and crystal have an asymmetric peak oxide component as well.

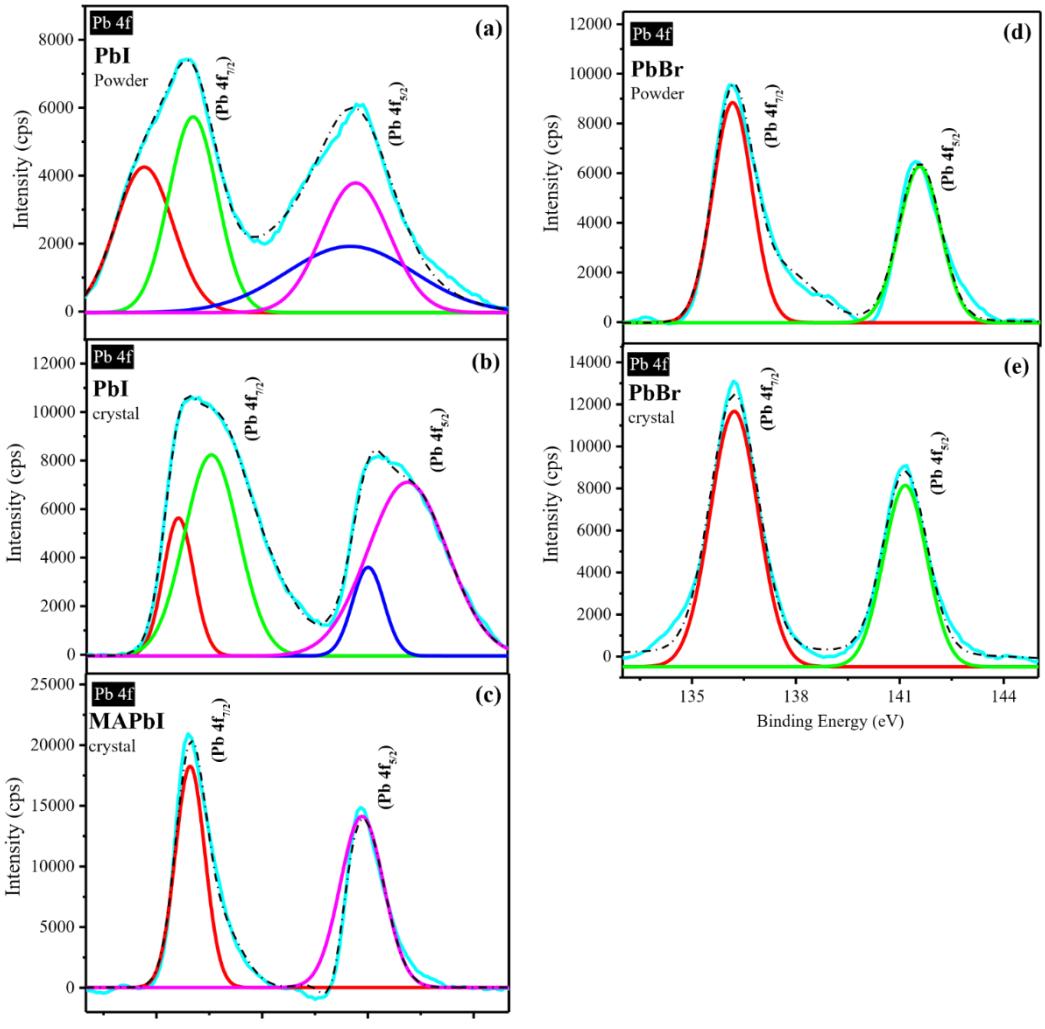

Figure 6.20: Core level XPS spectra for Lead (Pb 4f)

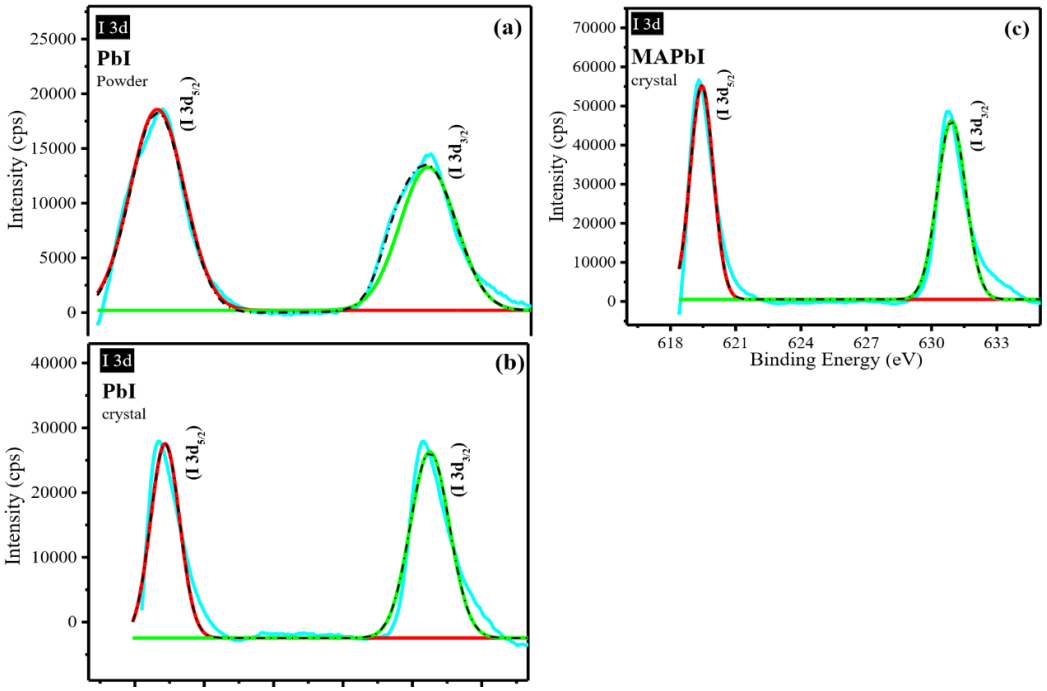

Figure 6.21: Core level XPS spectra for Iodine (I 3d)

Figure 6.21 (a-c) shows core level spectrum of iodine. Two different peaks of iodine first at approximately 619 eV for I $3d_{5/2}$ and other at 630 eV for I $3d_{3/2}$. The intensity of lead peaks has significantly improved in the crystals as compared to reference lead iodide powder. Furthermore, FWHM is fairly narrow at crystals.

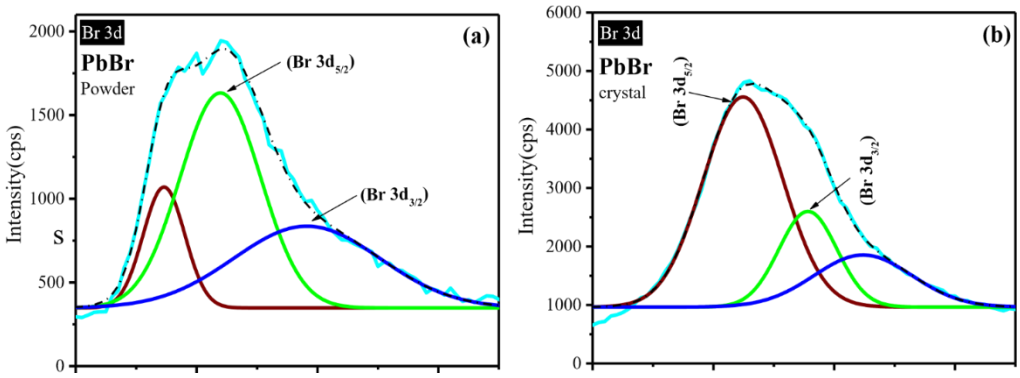

Figure 6.22: Core level XPS spectra for Bromine (I 3d)

Figure 6.22 (a-b) shows core level spectrum of Bromine. Two different peaks of Bromine first at approximately 68.5 eV for Br $3d_{5/2}$ and other at 70.1 eV for I $3d_{3/2}$. The intensity of bromine peaks has significantly improved in the crystals as compared to reference lead bromide powder.

Conclusions

In summary, facial growth of one-dimensional PbI_2 and $MAPbI_3$ based perovskite micro rods has been undertaken. The morphological, structural and thermal properties of the one-dimensional perovskite micro-rods have been examined using various characterization techniques. X-ray diffraction and SEM/EDX analyses confirm phase purity and high crystallinity of the developed micro-rods. Thermal analysis (TGA) indicates decent thermal stability of PbI_2, $PbBr_2$ and $MAIPbI_3$ microcrystals. The decomposition of PbI_2 microcrystals observed in the temperature of 500-600 °C is in good agreement with the thermal decomposition of the one dimensional perovskites. FTIR and Raman spectroscopy analyses confirm the existence of strong interactions between different stable groups in the crystals. The morphological studies (SEM/TEM) confirm crack free morphology of PbI_2 and $MAPbI_3$ micro-rods with porous structure. XPS results show elementals purity in crystal composition. The micro-rods of PbI_2 and $MAPbI_3$ may be considered for the application in perovskites photovoltaics and beyond. Hence, the development of these unique one-dimensional micro-rods represents a novel concept in materials design and synthesis that may foster ground-breaking research.

Chapter 7: Summary and Future Work

Summary

The various studies done in the presented work treat various aspects of monolithic perovskite solar cells, including fabrication and characterization of carbon layer, EIS study for mPSCs and growth of one-dimensional PbI_2 and $MAPbI_3$ rods.

In the first part electrical, structural and morphological properties of the carbon film have been investigated in the annealing temperature range 100°C - 400°C. The results show that best electrical characteristics are obtained for 250°C-300°C and further heating deforms and peels off the carbon film from substrates. Raman and XRD results show that electro-carbon quality improved with the increase of annealing temperature. However, no significant change in the surface morphology of the films has been observed. [119]

The second part consists of Calculation of power conversion efficiencies of the characterized mPSCs and the EIS study of the champion devices. The results show that the deprived electron extraction ability of c-TiO_2 affects the device performance, hence it is very important to have a pinhole free and compact c-TiO_2. On the other hand, a carbon electrode with insufficient hole extraction leads to a serious hole accumulation in the m-ZrO_2 results in serious carrier recombination leading to the poor device performance. However, with the increase in biasing voltage recombination resistance reduces and improves device performance.

In the Final part facial growth of one-dimensional PbI_2 and $MAPbI_3$ based perovskite micro rods has been undertaken. The morphological, structural and thermal properties of the one-dimensional perovskite micro-rods have been examined using various characterization techniques. X-ray diffraction and SEM/EDX analyses confirm phase purity and high crystallinity of the developed micro-rods. Thermal analysis (TGA) indicates decent thermal stability of PbI_2 and $MAPbI_3$ microcrystals. The decomposition of PbI_2

microcrystals observed in the temperature of 500-600 °C is in good agreement with the thermal decomposition of the one-dimensional perovskites. FTIR and Raman spectroscopy analyses confirm the existence of strong interactions between different stable groups in the crystals. The morphological studies (SEM/TEM) confirm crack free morphology of PbI_2 and $MAPbI_3$ micro-rods with porous structure. XPS results show elementals purity in crystal composition. The micro-rods of PbI_2 and $MAPbI_3$ may be considered for the application in perovskites photovoltaics and beyond. Hence, the development of these unique one-dimensional micros-rods represents a novel concept in materials, design and synthesis that may foster groundbreaking research. [174]

Future Work

Future work can be pursued by applying micro-rods of PbI_2, $PbBr_2$ and $MAPbI_3$ for the fabrication of mPSCs. The biggest disadvantage with the mPSCs is that high temperature heat treatment is required for different mesoporous layer fabrications. However, with the help of these micro-rods mPSCs may be produced without high temperature heat treatment. Furthermore, these micro-rods have a great potential for other opto-electronic device fabrication as switches and memories. They may also find applications in FET and OFETs.

References

[1] U. S. E. I. Administration., "Analysis of the Impacts of the Clean Power Plan [Accessed: 2019-02-0].".

[2] (2018). *Frankfurt School UNEP Centre and Bloomberg New Energy Finance*.

[3] J. Jean, P. R. Brown, R. L. Jaffe, T. Buonassisi, and V. Bulović, "Pathways for solar photovoltaics," *Energy & Environmental Science,* vol. 8, no. 4, pp. 12001219, 2015.

[4] M. A. Green *et al.*, "Solar cell efficiency tables (Version 53)," *Progress in Photovoltaics: Research and Applications,* vol. 27, no. 1, pp. 3-12, 2019.

[5] M. K. Nazeeruddin, "In retrospect: Twenty-five years of low-cost solar cells," (in eng), *Nature,* vol. 538, no. 7626, pp. 463-464, Oct 27 2016.

[6] B. O'Regan and M. Grätzel, "A low-cost, high-efficiency solar cell based on dye-sensitized colloidal TiO2 films," *Nature,* vol. 353, p. 737, 10/24/online 1991.

[7] U. Bach *et al.*, "Solid-state dye-sensitized mesoporous TiO_2 solar cells with high photon-to-electron conversion efficiencies," *Nature,* vol. 395, pp. 583585, 1998.

[8] N. Cai *et al.*, "An organic D-pi-A dye for record efficiency solid-state sensitized heterojunction solar cells," *Nano Lett,* vol. 11, no. 4, pp. 1452-6, Apr 13 2011.

[9] J. Burschka *et al.*, "Tris(2-(1H-pyrazol-1-yl)pyridine)cobalt(III) as p-type dopant for organic semiconductors and its application in highly efficient solidstate dye-sensitized solar cells," (in eng), *J Am Chem Soc,* vol. 133, no. 45, pp. 18042-5, Nov 16 2011.

[10] A. Kojima, K. Teshima, Y. Shirai, and T. Miyasaka, "Organometal halide perovskites as visible-light sensitizers for photovoltaic cells," (in eng), *J Am Chem Soc,* vol. 131, no. 17, pp. 6050-1, May 6 2009.

[11] M. I. Ahmed, A. Habib, and S. S. Javaid, "Perovskite Solar Cells: Potentials, Challenges, and Opportunities," *International Journal of Photoenergy,* vol. 2015, pp. 1-13, 2015.

[12] N. G. Park, "Perovskite solar cells: an emerging photovoltaic technology," *Materials Today,* vol. 18, no. 2, 2015.

[13] J. H. Im, C. R. Lee, J. W. Lee, S. W. Park, and N. G. Park, "6.5% efficient perovskite quantum-dot-sensitized solar cell," (in eng), *Nanoscale,* vol. 3, no. 10, pp. 4088-93, Oct 5 2011.

[14] H. S. Kim *et al.*, "Lead iodide perovskite sensitized all-solid-state submicron thin film mesoscopic solar cell with efficiency exceeding 9%," (in eng), *Sci Rep*, vol. 2, p. 591, 2012.

[15] M. M. Lee, J. Teuscher, T. Miyasaka, T. N. Murakami, and H. J. Snaith, "Efficient hybrid solar cells based on meso-superstructured organometal halide perovskites," (in eng), *Science*, vol. 338, no. 6107, pp. 643-7, Nov 2 2012.

[16] J. H. Heo *et al.*, "Efficient inorganic–organic hybrid heterojunction solar cells containing perovskite compound and polymeric hole conductors," *Nature Photonics*, Article vol. 7, p. 486, 05/05/online 2013.

[17] Y. Yovel, M. O. Franz, P. Stilz, and H. U. Schnitzler, "Plant classification from bat-like echolocation signals," *PLoS Computational Biology*, vol. 4, no. 3, p. e1000032, Mar 2008.

[18] NREL, "Efficiency chart," 2018.

[19] W. S. Yang *et al.*, "Iodide management in formamidinium-lead-halide-based perovskite layers for efficient solar cells," (in eng), *Science*, vol. 356, no. 6345, pp. 1376-1379, Jun 30 2017.

[20] D. Bi *et al.*, "Efficient luminescent solar cells based on tailored mixed-cation perovskites," (in eng), *Sci Adv*, vol. 2, no. 1, p. e1501170, Jan 2016.

[21] M. Grätzel, "The light and shade of perovskite solar cells," *Nature Materials*, vol. 13, p. 838, 08/21/online 2014.

[22] N.-G. Park, "Organometal Perovskite Light Absorbers Toward a 20% Efficiency Low-Cost Solid-State Mesoscopic Solar Cell," *The Journal of Physical Chemistry Letters*, vol. 4, no. 15, pp. 2423-2429, 2013/08/01 2013.

[23] M. Liu, M. B. Johnston, and H. J. Snaith, "Efficient planar heterojunction perovskite solar cells by vapour deposition," *Nature*, vol. 501, no. 7467, pp. 395-8, Sep 19 2013.

[24] J. Y. Jeng *et al.*, "$CH_3NH_3PbI_3$ perovskite/fullerene planar-heterojunction hybrid solar cells," *Adv Mater*, vol. 25, no. 27, pp. 3727-32, Jul 19 2013.

[25] Z. Xiao *et al.*, "Efficient, high yield perovskite photovoltaic devices grown by interdiffusion of solution-processed precursor stacking layers," *Energy Environ. Sci.*, vol. 7, no. 8, pp. 2619-2623, 2014.

[26] H. J. Snaith, "Present status and future prospects of perovskite photovoltaics," *Nat Mater*, vol. 17, no. 5, pp. 372-376, May 2018.

[27] M. A. Green and A. Ho-Baillie, "Perovskite Solar Cells: The Birth of a New Era in Photovoltaics," *ACS Energy Letters,* vol. 2, no. 4, pp. 822-830, 2017.

[28] W.-J. Yin, J.-H. Yang, J. Kang, Y. Yan, and S.-H. Wei, "Halide perovskite materials for solar cells: a theoretical review," *Journal of Materials Chemistry A,* vol. 3, no. 17, pp. 8926-8942, 2015.

[29] H. Tang, S. He, and C. Peng, "A Short Progress Report on High-Efficiency Perovskite Solar Cells," *Nanoscale Research Letters,* 2017.

[30] T. Schnier, J. Emara, S. Olthof, and K. Meerholz, "Influence of Hybrid Perovskite Fabrication Methods on Film Formation, Electronic Structure, and Solar Cell Performance," *Journal of Visualized Experiments,* no. 120, 2017.

[31] T. Oku, T. Matsumoto, A. Suzuki, and K. Suzuki, "Fabrication and Characterization of a Perovskite-Type Solar Cell with a Substrate Size of 70 mm," *Coatings,* 2015.

[32] M. Ye *et al.,* "Recent advances in interfacial engineering of perovskite solar cells," *Journal of Physics D: Applied Physics,* vol. 50, no. 37, 2017.

[33] A. Kojima, K. Teshima, Y. Shirai, and T. Miyasaka, "Organometal halide perovskites as visible-light sensitizers for photovoltaic cells.," *Journal of the American Chemical Society,* vol. 131, no. 17, 2009.

[34] J. Cui *et al.,* "Recent progress in efficient hybrid lead halide perovskite solar cells," *Sci Technol Adv Mater,* vol. 16, no. 3, p. 036004, Jun 2015.

[35] B. Saparov and D. B. Mitzi, "Organic-Inorganic Perovskites: Structural Versatility for Functional Materials Design," (in eng), *Chem Rev,* vol. 116, no. 7, pp. 4558-96, Apr 13 2016.

[36] C. H. Henry, "Limiting efficiencies of ideal single and multiple energy gap terrestrial solar cells," *Journal of Applied Physics,* vol. 51, no. 8, pp. 44944500, 1980.

[37] T. J. Coutts, K. A. Emery, and J. Scott Ward, "Modeled performance of polycrystalline thin-film tandem solar cells," *Progress in Photovoltaics: Research and Applications,* vol. 10, no. 3, pp. 195-203, 2002.

[38] Z. Yu, M. Leilaeioun, and Z. Holman, "Selecting tandem partners for silicon solar cells," *Nature Energy,* Comment vol. 1, p. 16137, 09/26/online 2016.

[39] A. Ibraheem, H.-B. Anita, and A. G. Martin, "Ultimate efficiency limit of single-junction perovskite and dual-junction perovskite/silicon two-terminal devices," *Japanese Journal of Applied Physics,* vol. 54, no. 8S1, p. 08KD04, 2015.

[40] M. H. Futscher and B. Ehrler, "Efficiency Limit of Perovskite/Si Tandem Solar Cells," *ACS Energy Letters*, vol. 1, no. 4, pp. 863-868, 2016/10/14 2016.

[41] L. Liang, Y. Cai, X. Li, M. K. Nazeeruddin, and P. Gao, "All that glitters is not gold: Recent progress of alternative counter electrodes for perovskite solar cells," *Nano Energy*, vol. 52, pp. 211-238, 2018.

[42] R. Fu, W. Zhou, Q. Li, Y. Zhao, D. Yu, and Q. Zhao, "Stability Challenges for Perovskite Solar Cells," *ChemNanoMat*, 2019.

[43] M. Saliba *et al.*, "A molecularly engineered hole-transporting material for efficient perovskite solar cells," *Nature Energy*, vol. 1, no. 2, 2016.

[44] J. A. Christians *et al.*, "Stability at Scale: Challenges of Module Interconnects for Perovskite Photovoltaics," *ACS Energy Letters*, vol. 3, no. 10, pp. 25022503, 2018.

[45] Y. Rong *et al.*, "Challenges for commercializing perovskite solar cells," *Science*, vol. 361, no. 6408, Sep 21 2018.

[46] H. Wei *et al.*, "Free-standing flexible carbon electrode for highly efficient hole-conductor-free perovskite solar cells," *Carbon*, vol. 93, pp. 861-868, 2015.

[47] Z. Ku, Y. Rong, M. Xu, T. Liu, and H. Han, "Full printable processed mesoscopic $CH_3NH_3PbI_3/TiO_2$ heterojunction solar cells with carbon counter electrode," (in eng), *Sci Rep*, vol. 3, p. 3132, Nov 4 2013.

[48] Y. Rong *et al.*, "Toward Industrial-Scale Production of Perovskite Solar Cells: Screen Printing, Slot-Die Coating, and Emerging Techniques," *J Phys Chem Lett*, vol. 9, no. 10, pp. 2707-2713, May 17 2018.

[49] W. Chen *et al.*, "A comparative study of planar and mesoporous perovskite solar cells with printable carbon electrodes," *Journal of Power Sources*, vol. 412, pp. 118-124, 2019.

[50] M. Duan, Y. Hu, A. Mei, Y. Rong, and H. Han, "Printable carbon-based holeconductor-free mesoscopic perovskite solar cells: From lab to market," *Materials Today Energy*, vol. 7, pp. 221-231, 2018.

[51] Z. Liu *et al.*, "15% efficient carbon based planar-heterojunction perovskite solar cells using a TiO_2/SnO_2 bilayer as the electron transport layer," *Journal of Materials Chemistry A*, vol. 6, no. 17, pp. 7409-7419, 2018.

[52] P. Zhang *et al.*, "Perovskite Solar Cells with ZnO Electron-Transporting Materials," *Adv Mater*, vol. 30, no. 3, Jan 2018.

[53] C. Zhang, Y. Luo, X. Chen, Y. Chen, Z. Sun, and s. Huang, *Effective Improvement of the Photovoltaic Performance of Carbon Based Perovskite Solar Cells by Additional Solvents*. 2016.

[54] J. Chen *et al.*, "Solvent effect on the hole-conductor-free fully printable perovskite solar cells " *Nano Energy*, vol. 27, pp. 130-137, 2016/09/01/ 2016.

[55] A. Mei *et al.*, "A hole-conductor–free, fully printable mesoscopic perovskite solar cell with high stability," *Science*, vol. 345, no. 6194, p. 295, 2014.

[56] Y. Yang *et al.*, "The size effect of TiO_2 nanoparticles on a printable mesoscopic perovskite solar cell," *Journal of Materials Chemistry A*, 10.1039/C4TA07030E vol. 3, no. 17, pp. 9103-9107, 2015.

[57] T. Liu *et al.*, "Critical parameters in TiO_2/ZrO_2/Carbon-based mesoscopic perovskite solar cell," *Journal of Power Sources*, vol. 293, pp. 533-538, 2015/10/20/ 2015.

[58] A. K. Baranwal *et al.*, "100°C Thermal Stability of Printable Perovskite Solar Cells Using Porous Carbon Counter Electrodes," (in eng), *ChemSusChem*, vol. 9, no. 18, pp. 2604-2608, Sep 22 2016.

[59] A. Kay and M. Grätzel, "Low cost photovoltaic modules based on dye sensitized nanocrystalline titanium dioxide and carbon powder," *Solar Energy Materials and Solar Cells*, vol. 44, no. 1, pp. 99-117, 1996/10/30/ 1996.

[60] M. Xu *et al.*, "Highly ordered mesoporous carbon for mesoscopic $CH_3NH_3PbI_3$/TiO_2 heterojunction solar cell," *Journal of Materials Chemistry A*, vol. 2, no. 23, 2014.

[61] Y. Rong *et al.*, "Hole-Conductor-Free Mesoscopic TiO_2/$CH_3NH_3PbI_3$ Heterojunction Solar Cells Based on Anatase Nanosheets and Carbon Counter Electrodes," *J Phys Chem Lett*, vol. 5, no. 12, pp. 2160-4, Jun 19 2014.

[62] L. Zhang *et al.*, "The effect of carbon counter electrodes on fully printable mesoscopic perovskite solar cells " *Journal of Materials Chemistry A*, vol. 3, no. 17, pp. 9165-9170, 2015.

[63] L. Liu *et al.*, "Fully printable mesoscopic perovskite solar cells with organic silane self-assembled monolayer," (in eng), *J Am Chem Soc*, vol. 137, no. 5, pp. 1790-3, Feb 11 2015.

[64] X. Li *et al.*, "Outdoor Performance and Stability under Elevated Temperatures and Long-Term Light Soaking of Triple-Layer Mesoporous Perovskite Photovoltaics," *Energy Technology*, vol. 3, no. 6, pp. 551-555, 2015.

[65] J. Chen *et al.*, "Hole-Conductor-Free Fully Printable Mesoscopic Solar Cell with Mixed-Anion Perovskite $CH_3NH_3PbI_{(3-x)}(BF_4)_x$," *Advanced Energy Materials,* vol. 6, no. 5, 2016.

[66] Y. Sheng *et al.*, "Enhanced electronic properties in $CH_3NH_3PbI_3$ via LiCl mixing for hole-conductor-free printable perovskite solar cells," *Journal of Materials Chemistry A,* vol. 4, no. 42, pp. 16731-16736, 2016.

[67] X. Hou *et al.*, "Effect of guanidinium on mesoscopic perovskite solar cells," *Journal of Materials Chemistry A,* vol. 5, no. 1, pp. 73-78, 2017.

[68] S. G. Hashmi *et al.*, "Air Processed Inkjet Infiltrated Carbon Based Printed Perovskite Solar Cells with High Stability and Reproducibility," *Advanced Materials Technologies,* vol. 2, no. 1, 2017.

[69] S. G. Hashmi *et al.*, "Long term stability of air processed inkjet infiltrated carbon-based printed perovskite solar cells under intense ultra-violet light soaking," *Journal of Materials Chemistry A,* 10.1039/C6TA10605F vol. 5, no. 10, pp. 4797-4802, 2017.

[70] S. G. Hashmi *et al.*, "High performance carbon-based printed perovskite solar cells with humidity assisted thermal treatment," *Journal of Materials Chemistry A,* 10.1039/C7TA04132B vol. 5, no. 24, pp. 12060-12067, 2017.

[71] Y. Hu *et al.*, "Stable Large-Area (10 × 10 cm2) Printable Mesoscopic Perovskite Module Exceeding 10% Efficiency," *Solar RRL,* vol. 1, no. 2, p. 1600019, 2017/02/01 2017.

[72] R. Holtzman and E. Segre, "Wettability Stabilizes Fluid Invasion into Porous Media via Nonlocal, Cooperative Pore Filling," (in eng), *Phys Rev Lett,* vol. 115, no. 16, p. 164501, Oct 16 2015.

[73] A. Priyadarshi *et al.*, "A large area (70 cm^2) monolithic perovskite solar module with a high efficiency and stability," *Energy & Environmental Science,* 10.1039/C6EE02693A vol. 9, no. 12, pp. 3687-3692, 2016.

[74] N. Alleborn and H. Raszillier, "Spreading and sorption of droplets on layered porous substrates," (in eng), *J Colloid Interface Sci,* vol. 280, no. 2, pp. 44964, Dec 15 2004.

[75] D. R. Heine, G. S. Grest, and E. B. Webb, 3rd, "Surface wetting of liquid nanodroplets: droplet-size effects," (in eng), *Phys Rev Lett,* vol. 95, no. 10, p. 107801, Sep 2 2005.

[76] H. Chen and S. Yang, "Carbon-Based Perovskite Solar Cells without Hole Transport Materials: The Front Runner to the Market?," (in eng), *Adv Mater,* vol. 29, no. 24, Jun 2017.

[77] G. Grancini *et al.*, "One-Year stable perovskite solar cells by 2D/3D interface engineering," *Nature Communications,* Article vol. 8, p. 15684, 06/01/online 2017.

[78] A. Bashir *et al.*, "Spinel Co3O4 nanomaterials for efficient and stable large area carbon-based printed perovskite solar cells," *Nanoscale,* 10.1039/C7NR08289D vol. 10, no. 5, pp. 2341-2350, 2018.

[79] R. Hu, L. Chu, J. Zhang, X. a. Li, and W. Huang, "Carbon materials for enhancing charge transport in the advancements of perovskite solar cells," *Journal of Power Sources,* vol. 361, pp. 259-275, 2017.

[80] G. Liu *et al.*, "A mesoscopic platinized graphite/carbon black counter electrode for a highly efficient monolithic dye-sensitized solar cell," *Electrochimica Acta,* vol. 69, pp. 334-339, 2012.

[81] Y. Cai, L. Liang, and P. Gao, "Promise of commercialization: Carbon materials for low-cost perovskite solar cells," *Chinese Physics B,* vol. 27, no. 1, p. 018805, 2018.

[82] Z. Wu, T. Song, and B. Sun, "Carbon-Based Materials Used for Perovskite Solar Cells," *ChemNanoMat,* vol. 3, no. 2, pp. 75-88, 2017.

[83] R. L. McCreery, "Advanced carbon electrode materials for molecular electrochemistry," (in eng), *Chem Rev,* vol. 108, no. 7, pp. 2646-87, Jul 2008.

[84] U. O. Uyor, A. P. Popoola, O. Popoola, and V. S. Aigbodion, "Energy storage and loss capacity of graphene-reinforced poly(vinylidene fluoride) nanocomposites from electrical and dielectric properties perspective: A review," *Advances in Polymer Technology,* vol. 37, no. 8, pp. 2838-2858, 2018.

[85] J. Liu, Q. Ma, Z. Huang, G. Liu, and H. Zhang, "Recent Progress in GrapheneBased Noble-Metal Nanocomposites for Electrocatalytic Applications," *Adv Mater,* p. e1800696, Sep 5 2018.

[86] T. T. Oo and S. Debnath, "Application of carbon nanotubes in perovskite solar cells: A review," *AIP Conference Proceedings,* vol. 1902, no. 1, p. 020015, 2017.

[87] C. Yu, L. Lusheng, and G. Peng, "Promise of commercialization: Carbon materials for low-cost perovskite solar cells," *Chinese Physics B,* vol. 27, no. 1, p. 018805, 2018.

[88] H. Luo, X. Lin, X. Hou, L. Pan, S. Huang, and X. Chen, "Efficient and airstable planar perovskite solar cells formed on graphene-oxide-modified PEDOT: PSS hole transport layer," *Nano-Micro Letters,* vol. 9, no. 4, p. 39, 2017.

[89] E. Jewell, B. Philip, and P. Greenwood, "Improved Manufacturing Performance of Screen Printed Carbon Electrodes through Material Formulation," *Biosensors,* vol. 6, no. 3, p. 30, 2016.

[90] K. S. Kim *et al.*, "Large-scale pattern growth of graphene films for stretchable transparent electrodes," *Nature,* vol. 457, p. 706, 01/14/online 2009.

[91] N. N. Rosli, M. A. Ibrahim, N. Ahmad Ludin, M. A. Mat Teridi, and K. Sopian, "A review of graphene based transparent conducting films for use in solar photovoltaic applications," *Renewable and Sustainable Energy Reviews,* vol. 99, pp. 83-99, 2019.

[92] E. L. Lim, C. C. Yap, M. H. H. Jumali, M. A. M. Teridi, and C. H. Teh, "A Mini Review: Can Graphene Be a Novel Material for Perovskite Solar Cell Applications?," *Nanomicro Lett,* vol. 10, no. 2, p. 27, 2018.

[93] Z. Wei, H. Chen, K. Yan, X. Zheng, and S. Yang, "Hysteresis-free multiwalled carbon nanotube-based perovskite solar cells with a high fill factor," *Journal of Materials Chemistry A,* vol. 3, no. 48, pp. 24226-24231, 2015.

[94] Z. Liu *et al.*, "Efficient Carbon-Based $CsPbBr_3$ Inorganic Perovskite Solar Cells by Using Cu-Phthalocyanine as Hole Transport Material," *Nano-Micro Letters,* vol. 10, no. 2, p. 34, 2018.

[95] P. Jiang *et al.*, "Fully printable perovskite solar cells with highly-conductive, low-temperature, perovskite-compatible carbon electrode," *Carbon,* vol. 129, pp. 830-836, 2018/04/01/ 2018.

[96] G. J., Z. Zhou, K. Sumathy, H. Yang, and Q. Qiao, "Activated graphene nanoplatelets as a counter electrode for dye-sensitized solar cells," *Journal of Applied Physics,* vol. 119, no. 13, p. 135501, 2016.

[97] Q. Luo *et al.*, "All-Carbon-Electrode-Based Endurable Flexible Perovskite Solar Cells," *Advanced Functional Materials,* vol. 28, no. 11, 2018.

[98] V. T. Tiong *et al.*, "Octadecylamine-Functionalized Single-Walled Carbon Nanotubes for Facilitating the Formation of a Monolithic Perovskite Layer and

Stable Solar Cells," *Advanced Functional Materials,* vol. 28, no. 10, p. 1705545, 2018/03/01 2018.

[99] H. Tao *et al.*, "Efficiency enhancement of perovskite solar cells by forming a tighter interface contact of C/$CH_3NH_3PbI_3$," *Journal of Physics and Chemistry of Solids,* vol. 123, pp. 25-31, 2018.

[100] Y. Wang, H. Zhao, Y. Mei, H. Liu, S. Wang, and X. Li, "A Carbon Nanotube Bridging Method for Hole Transport Layer-Free Paintable Carbon-Based Perovskite Solar Cells," *ACS Appl Mater Interfaces,* Dec 13 2018.

[101] L. Najafi *et al.*, "MoS_2 Quantum Dot/Graphene Hybrids for Advanced Interface Engineering of a $CH_3NH_3PbI_3$ Perovskite Solar Cell with an Efficiency of over 20," *ACS Nano,* vol. 12, no. 11, pp. 10736-10754, Nov 27 2018.

[102] Y. Busby *et al.*, "Aging effects in interface-engineered perovskite solar cells with 2D nanomaterials: A depth profile analysis," *Materials Today Energy,* vol. 9, pp. 1-10, 2018.

[103] Q. Q. Chu *et al.*, "Highly stable carbon-based perovskite solar cell with a record efficiency of over 18% via hole transport engineering," *Journal of Materials Science & Technology,* 2019.

[104] I. Hussain *et al.*, "Conductive glass free carbon nanotube micro yarn based perovskite solar cells," *Applied Surface Science,* vol. 478, pp. 327-333, 2019.

[105] R. Ishikawa, S. Watanabe, S. Yamazaki, T. Oya, and N. Tsuboi, "Perovskite/Graphene Solar Cells without a Hole-Transport Layer," *ACS Applied Energy Materials,* vol. 2, no. 1, pp. 171-175, 2019.

[106] Y. Guan *et al.*, "Fullerene derivative as an additive for highly efficient printable mesoscopic perovskite solar cells," *Organic Electronics,* vol. 62, pp. 653-659, 2018.

[107] H. Zou, D. Guo, B. He, J. Yu, and K. Fan, "Enhanced photocurrent density of HTM-free perovskite solar cells by carbon quantum dots," *Applied Surface Science,* vol. 430, pp. 625-631, 2018.

[108] Y. Hu *et al.*, "Improved Performance of Printable Perovskite Solar Cells with Bifunctional Conjugated Organic Molecule," *Adv Mater,* vol. 30, no. 11, Mar 2018.

[109] L. Wagner, S. Chacko, G. Mathiazhagan, S. Mastroianni, and A. Hinsch,

"High Photovoltage of 1 V on a Steady-State Certified Hole Transport Layer Free Perovskite Solar Cell by a Molten-Salt Approach," *ACS Energy Letters,* vol. 3, no. 5, pp. 1122-1127, 2018.

[110] Y. Zhang, J. Zhao, J. Zhang, X. Jiang, Z. Zhu, and Q. Liu, "Interface Engineering Based on Liquid Metal for Compact-Layer-free, Fully Printable Mesoscopic Perovskite Solar Cells," *ACS Appl Mater Interfaces,* vol. 10, no. 18, pp. 15616-15623, May 9 2018.

[111] X. Hou *et al.*, "High performance printable perovskite solar cells based on $Cs_{0.1}FA_{0.9}PbI_3$ in mesoporous scaffolds," *Journal of Power Sources,* vol. 415, pp. 105-111, 2019.

[112] J. Zhao *et al.*, "Band Alignment Strategy for Printable Triple Mesoscopic Perovskite Solar Cells with Enhanced Photovoltage," *ACS Applied Energy Materials,* 2019.

[113] B. Zong *et al.*, "Highly stable hole-conductor-free perovskite solar cells based upon ammonium chloride and a carbon electrode," *J Colloid Interface Sci,* vol. 540, pp. 315-321, Jan 12 2019.

[114] Y. Liang *et al.*, "Achieving High Open-Circuit Voltages up to 1.57 V in Hole Transport-Material-Free MAPbBr3 Solar Cells with Carbon Electrodes," *Advanced Energy Materials,* vol. 8, no. 4, p. 1701159, 2018/02/01 2018.

[115] B. Zong *et al.*, "Highly stable hole-conductor-free $CH_3NH_3Pb(I_{1-x}Br_x)_3$ perovskite solar cells with carbon counter electrode," *Journal of Alloys and Compounds,* vol. 748, pp. 1006-1012, 2018.

[116] B. Li *et al.*, "Constructing water-resistant $CH_3NH_3PbI_3$ perovskite films via coordination interaction," *Journal of Materials Chemistry A,* vol. 4, no. 43, pp. 17018-17024, 2016.

[117] S. Yu, Y. Yan, Y. Chen, P. Chábera, K. Zheng, and Z. Liang, "Enabling room temperature processed highly efficient and stable 2D Ruddlesden–Popper perovskite solar cells with eliminated hysteresis by synergistic exploitation of additives and solvents," *Journal of Materials Chemistry A,* vol. 7, no. 5, pp. 2015-2021, 2019.

[118] M. Yang *et al.*, "Perovskite ink with wide processing window for scalable high-efficiency solar cells," *Nature Energy,* vol. 2, no. 5, 2017.

[119] A. Mishra *et al.*, "Effect of annealing temperature on the performance of printable carbon electrodes for perovskite solar cells," *Organic Electronics*, vol. 65, pp. 375-380, 2019/02/01/ 2019.

[120] H. Kim *et al.*, "Effect of film thickness on the properties of indium tin oxide thin films," *Journal of Applied Physics*, vol. 88, no. 10, pp. 6021-6025, 2000.

[121] C. Zhang *et al.*, "Influence of different TiO2 blocking films on the photovoltaic performance of perovskite solar cells," *Applied Surface Science*, vol. 388, pp. 82-88, 2016.

[122] O. D. Renedo, M. A. Alonso-Lomillo, and M. J. Martinez, "Recent developments in the field of screen-printed electrodes and their related applications," (in eng), *Talanta*, vol. 73, no. 2, pp. 202-19, Sep 15 2007.

[123] Z. Congcong *et al.*, "Graphene oxide reduced and modified by environmentally friendly glycylglycine and its excellent catalytic performance," *Nanotechnology*, vol. 25, no. 13, p. 135707, 2014.

[124] L. Bokobza, J.-L. Bruneel, and M. Couzi, "Raman Spectra of Carbon-Based Materials (from Graphite to Carbon Black) and of Some Silicone Composites," *C*, vol. 1, no. 1, p. 77, 2015.

[125] R. A. DiLeo, B. J. Landi, and R. P. Raffaelle, "Purity assessment of multiwalled carbon nanotubes by Raman spectroscopy," *Journal of Applied Physics*, vol. 101, no. 6, p. 064307, 2007.

[126] C. Branca, F. Frusteri, V. Magazù, and A. Mangione, "Characterization of Carbon Nanotubes by TEM and Infrared Spectroscopy," *The Journal of Physical Chemistry B*, vol. 108, no. 11, pp. 3469-3473, 2004/03/01 2004.

[127] S. Lefrant, M. Baibarac, and I. Baltog, "Raman and FTIR spectroscopy as valuable tools for the characterization of polymer and carbon nanotube based composites," *Journal of Materials Chemistry*, 10.1039/B821136A vol. 19, no. 32, pp. 5690-5704, 2009.

[128] A. Misra, P. K. Tyagi, P. Rai, and D. S. Misra, "FTIR spectroscopy of multiwalled carbon nanotubes: a simple approach to study the nitrogen doping," (in eng), *J Nanosci Nanotechnol*, vol. 7, no. 6, pp. 1820-3, Jun 2007.

[129] G. Pavoski *et al.*, "Few layer reduced graphene oxide: evaluation of the best experimental conditions for easy production," *Materials Research*, vol. 20, no. 1, pp. 53-61, 2017.

[130] A. Dualeh *et al.*, "Impedance spectroscopic analysis of lead iodide perovskitesensitized solid-state solar cells," (in eng), *ACS Nano,* vol. 8, no. 1, pp. 36273, Jan 28 2014.

[131] Z. Meng, D. Guo, J. Yu, and K. Fan, "Investigation of Al 2 O 3 and ZrO 2 spacer layers for fully printable and hole-conductor-free mesoscopic perovskite solar cells," *Applied Surface Science,* vol. 430, pp. 632-638, 2018.

[132] K. S. Novoselov *et al.*, "Electric field effect in atomically thin carbon films," (in eng), *Science,* vol. 306, no. 5696, pp. 666-9, Oct 22 2004.

[133] S. Z. Butler *et al.*, "Progress, challenges, and opportunities in two-dimensional materials beyond graphene," (in eng), *ACS Nano,* vol. 7, no. 4, pp. 2898-926, Apr 23 2013.

[134] A. J. Mannix, B. Kiraly, M. C. Hersam, and N. P. Guisinger, "Synthesis and chemistry of elemental 2D materials," *Nature Reviews Chemistry,* Review Article vol. 1, p. 0014, 01/25/online 2017.

[135] S. Tongay, "Preface to a Special Topic: 2D Materials and Applications," *Applied Physics Reviews,* vol. 5, no. 1, p. 010401, 2018.

[136] G. R. Bhimanapati *et al.*, "Recent Advances in Two-Dimensional Materials beyond Graphene," (in eng), *ACS Nano,* vol. 9, no. 12, pp. 11509-39, Dec 22 2015.

[137] V. Kaushik, S. Wu, H. Jang, J. Kang, K. Kim, and J. W. Suk, "Scalable Exfoliation of Bulk MoS(2) to Single- and Few-Layers Using Toroidal Taylor Vortices," (in eng), *Nanomaterials (Basel),* vol. 8, no. 8, Aug 1 2018.

[138] L. Yang *et al.*, "Properties, Preparation and Applications of Low Dimensional Transition Metal Dichalcogenides," (in eng), *Nanomaterials (Basel),* vol. 8, no. 7, Jun 26 2018.

[139] S. I. Seok, M. Grätzel, and N.-G. Park, "Methodologies toward Highly Efficient Perovskite Solar Cells," *Small,* vol. 14, no. 20, p. 1704177, 2018.

[140] J.-P. Correa-Baena *et al.*, "The rapid evolution of highly efficient perovskite solar cells," *Energy & Environmental Science,* 10.1039/C6EE03397K vol. 10, no. 3, pp. 710-727, 2017.

[141] Y. Dang *et al.*, "Bulk crystal growth of hybrid perovskite material CH3NH3PbI3," *CrystEngComm,* 10.1039/C4CE02106A vol. 17, no. 3, pp. 665-670, 2015.

[142] L. K. Ono, N.-G. Park, K. Zhu, W. Huang, and Y. Qi, "Perovskite Solar Cells—Towards Commercialization," *ACS Energy Letters,* vol. 2, no. 8, pp. 1749-1751, 2017/08/11 2017.

[143] A. Rajagopal, K. Yao, and A. K.-Y. Jen, "Toward Perovskite Solar Cell Commercialization: A Perspective and Research Roadmap Based on Interfacial Engineering," *Advanced Materials,* vol. 30, no. 32, p. 1800455, 2018.

[144] Y. Liu *et al.*, "Two-Inch-Sized Perovskite $CH_3NH_3PbX_3$ (X = Cl, Br, I) Crystals: Growth and Characterization," (in eng), *Adv Mater,* vol. 27, no. 35, pp. 5176-83, Sep 16 2015.

[145] J.-H. Cha *et al.*, "Photoresponse of CsPbBr3 and Cs4PbBr6 Perovskite Single Crystals," *The Journal of Physical Chemistry Letters,* vol. 8, no. 3, pp. 565570, 2017/02/02 2017.

[146] C. Zhou *et al.*, "Low-Dimensional Organic Tin Bromide Perovskites and Their Photoinduced Structural Transformation," *Angewandte Chemie,* vol. 129, no. 31, pp. 9146-9150, 2017.

[147] D. Ma, Y. Fu, L. Dang, J. Zhai, I. A. Guzei, and S. Jin, "Single-crystal microplates of two-dimensional organic–inorganic lead halide layered perovskites for optoelectronics," *Nano Research,* journal article vol. 10, no. 6, pp. 2117-2129, June 01 2017.

[148] J. H. Im *et al.*, "Nanowire perovskite solar cell," (in eng), *Nano Lett,* vol. 15, no. 3, pp. 2120-6, Mar 11 2015.

[149] A. R. b. M. Yusoff and M. K. Nazeeruddin, "Low-Dimensional Perovskites: From Synthesis to Stability in Perovskite Solar Cells," *Advanced Energy Materials,* vol. 8, no. 26, p. 1702073, 2018.

[150] Y. Li, H. Huang, Y. Xiong, S. V. Kershaw, and A. L. Rogach, "Revealing the Formation Mechanism of CsPbBr3 Perovskite Nanocrystals Produced via a Slowed-Down Microwave- Assiste Synthesis," *Angewandte Chemie International Edition,* vol. 57, no. 20, pp. 5833-5837, 2018.

[151] H. Huang *et al.*, "Growth mechanism of strongly emitting CH3NH3PbBr3 perovskite nanocrystals with a tunable bandgap," *Nature Communications,* vol. 8, no. 1, p. 996, 2017/10/17 2017.

[152] V. Adinolfi, W. Peng, G. Walters, O. M. Bakr, and E. H. Sargent, "The Electrical and Optical Properties of Organometal Halide Perovskites Relevant to

Optoelectronic Performance," *Advanced Materials,* vol. 30, no. 1, p. 1700764, 2018.

[153] J. Huang, Y. Shao, and Q. Dong, "Organometal Trihalide Perovskite Single Crystals: A Next Wave of Materials for 25% Efficiency Photovoltaics and Applications Beyond?," *The Journal of Physical Chemistry Letters,* vol. 6, no. 16, pp. 3218-3227, 2015/08/20 2015.

[154] S. Jin, Y. Fu, and F. Meng, "Solution Growth Of Single-Crystal Perovskite Structures," 2017.

[155] H. Zhu *et al.*, "Lead halide perovskite nanowire lasers with low lasing thresholds and high quality factors," *Nat Mater,* vol. 14, no. 6, pp. 636-42, Jun 2015.

[156] J. Huang and Q. Dong, "Method for single crystal growth of photovoltaic perovskite material and devices," 2017.

[157] P.-A. Mante, C. C. Stoumpos, M. G. Kanatzidis, and A. Yartsev, "Electron–acoustic phonon coupling in single crystal CH3NH3PbI3 perovskites revealed by coherent acoustic phonons," *Nature Communications,* Article vol. 8, p. 14398, 02/08/online 2017.

[158] Y. Fu *et al.*, "Solution growth of single crystal methylammonium lead halide perovskite nanostructures for optoelectronic and photovoltaic applications," (in eng), *J Am Chem Soc,* vol. 137, no. 17, pp. 5810-8, May 6 2015.

[159] M. Xiao *et al.*, "A fast deposition-crystallization procedure for highly efficient lead iodide perovskite thin-film solar cells," (in eng), *Angew Chem Int Ed Engl,* vol. 53, no. 37, pp. 9898-903, Sep 8 2014.

[160] P. Beckmann, *ChemInform Abstract: A Review of Polytypism in Lead Iodide*. 2010, pp. 455-460.

[161] B. R. Vincent, K. N. Robertson, T. S. Cameron, and O. Knop, "Alkylammonium lead halides. Part 1. Isolated PbI64− ions in (CH3NH3)4PbI6•2H2O," *Canadian Journal of Chemistry,* vol. 65, no. 5, pp. 1042-1046, 1987/05/01 1987.

[162] Z. Zheng *et al.*, "In situ growth of epitaxial lead iodide films composed of hexagonal single crystals," *Journal of Materials Chemistry,* 10.1039/B510077A vol. 15, no. 42, pp. 4555-4559, 2005.

[163] M. Ledinský *et al.*, "Raman Spectroscopy of Organic–Inorganic Halide Perovskites," *The Journal of Physical Chemistry Letters*, vol. 6, no. 3, pp. 401406, 2015.

[164] R. G. Niemann *et al.*, "Halogen Effects on Ordering and Bonding of CH3NH3+ in CH3NH3PbX3 (X = Cl, Br, I) Hybrid Perovskites: A Vibrational Spectroscopic Study," *The Journal of Physical Chemistry C*, vol. 120, no. 5, pp. 2509-2519, 2016.

[165] C. Quarti *et al.*, "The Raman Spectrum of the CH3NH3PbI3 Hybrid Perovskite: Interplay of Theory and Experiment," *The Journal of Physical Chemistry Letters*, vol. 5, no. 2, pp. 279-284, 2014.

[166] J. Idígoras, A. Todinova, J. R. Sánchez-Valencia, A. Barranco, A. Borrás, and J. A. Anta, "The interaction between hybrid organic–inorganic halide perovskite and selective contacts in perovskite solar cells: an infrared spectroscopy study," *Physical Chemistry Chemical Physics*,10.1039/C6CP01265E vol. 18, no. 19, pp. 13583-13590, 2016.

[167] M. A. Pérez-Osorio *et al.*, "Vibrational Properties of the Organic–Inorganic Halide Perovskite $CH_3NH_3PbI_3$ from Theory and Experiment: Factor Group Analysis, First-Principles Calculations, and Low-Temperature Infrared Spectra," *The Journal of Physical Chemistry C*, vol. 119, no. 46, pp. 2570325718, 2015/11/19 2015.

[168] N. Ahn, D. Y. Son, I. H. Jang, S. M. Kang, M. Choi, and N. G. Park, "Highly Reproducible Perovskite Solar Cells with Average Efficiency of 18.3% and Best Efficiency of 19.7% Fabricated via Lewis Base Adduct of Lead(II) Iodide," (in eng), *J Am Chem Soc*, vol. 137, no. 27, pp. 8696-9, Jul 15 2015.

[169] E. Mosconi, C. Quarti, T. Ivanovska, G. Ruani, and F. De Angelis, "Structural and electronic properties of organo-halide lead perovskites: a combined IRspectroscopy and ab initio molecular dynamics investigation," (in eng), *Phys Chem Chem Phys*, vol. 16, no. 30, pp. 16137-44, Aug 14 2014.

[170] B. D. Fahlman and A. R. Barron, "Substituent effects on the volatility of metal β-diketonates," *Advanced Materials for Optics and Electronics*, vol. 10, no. 35, pp. 223-232, 2000.

[171] T. Baikie *et al.*, "Synthesis and crystal chemistry of the hybrid perovskite (CH3NH3)PbI3 for solid-state sensitised solar cell applications," *Journal of*

Materials Chemistry A, 10.1039/C3TA10518K vol. 1, no. 18, pp. 5628-5641, 2013.

[172] T. Supasai, N. Rujisamphan, K. Ullrich, A. Chemseddine, and T. Dittrich, "Formation of a passivating CH3NH3PbI3/PbI2 interface during moderate heating of CH3NH3PbI3 layers," *Applied Physics Letters,* vol. 103, no. 18, p. 183906, 2013/10/28 2013.

[173] J. Cao *et al.*, "Porous PbI_2 films for the fabrication of efficient, stable perovskite solar cells via sequential deposition," *Journal of Materials Chemistry A,* 10.1039/C6TA03121H vol. 4, no. 26, pp. 10223-10230, 2016.

[174] A. Mishra, Z. Ahmad, F. Touati, R. A. Shakoor, and M. K. Nazeeruddin, "One-dimensional Facile Growth of $MAPbI_3$ Perovskite Micro-rods," *RSC Advances,* 2019.